MULTIPHASE MODELS OF SLAG LAYER BUILT-UP IN SOLID FUEL GASIFICATION AND COMBUSTION

by

Sze Zheng Yong

Dipl.(FH), Automotive Engineering – Mechatronics
Esslingen University of Applied Sciences, 2008

Submitted to the Department of Mechanical Engineering in Partial Fulfillment of the Requirements for the Degree of

Master of Science in Mechanical Engineering
at the
MASSACHUSETTS INSTITUTE OF TECHNOLOGY

JUNE 2010

Signature of Author .....
Department of Mechanical Engineering
May 19, 2010

Certified by .....
Ahmed F. Ghoniem
Ronald C. Crane Professor of Mechanical Engineering
Thesis Supervisor

Accepted by .....
David E. Hardt
Chairman, Department Committee on Graduate Students

Page left intentionally blank

MULTIPHASE MODELS OF SLAG LAYER BUILT-UP IN SOLID FUEL GASIFICATION AND COMBUSTION

by

Sze Zheng Yong

Submitted to the Department of Mechanical Engineering
on May 19, 2010 in partial fulfillment of the
requirements for the degree of Master of Science in
Mechanical Engineering

Abstract

A steady-state model has been developed to describe the flow and heat transfer characteristics of slag. The model incorporates two submodels for particle capture and wall burning; takes into consideration the temperature and composition dependent properties of slag, the contribution of momentum of captured particles and the possibility of slag resolidification. The model predicts the local thickness of molten and solid slag layers as well as the average slag velocity. Moreover, it is capable of predicting heat losses and the inner as well as outer wall temperatures, taking into account the influence of molten and resolidified slag layers coating the combustor or reactor wall.

An equally important issue is the interaction of the particles colliding with the slag layer. High inertia particles tend to rebound whereas slower particles are trapped in the slag layer. Since only trapped particles are relevant to the slag layer built-up, a particle capture criterion for colliding particles is introduced. Particles with combustibles may be captured by the slag layer while they continue to burn at a different rate. To take this into account, a wall burning submodel is proposed to predict a correction factor for both solid and porous char combustion models.

Thesis Supervisor: Ahmed F. Ghoniem
Title: Ronald C. Crane Professor of Mechanical Engineering

Page left intentionally blank

Acknowledgements

First of all, I would like to thank my advisor, Professor Ahmed Ghoniem, for giving me the opportunity to do research for the past two years. Without his invaluable guidance and consistent support throughout my Master's program, I would not have found this interesting research problem and this thesis would not have been possible. Furthermore, he has always pointed me in the right direction, ensuring that my work has sufficient depth and applicability.

I am also grateful to my colleagues in the ENEL oxy-coal combustion project team, Lei Chen, Chukwunwike Iloeje and James Hong, for providing essential information and support whenever I needed inputs from others. I would also like to thank Anup Shirgaonkar for his kind advice and support, especially with the DNS simulations to help validate my wall burning submodel. Many thanks to Mayank Kumar, Simcha Singer and Rory Monaghan too for their support and inputs on modeling the gasifier and writing UDFs, and to all my lab-mates in the Reacting Gas Dynamics group. It has indeed been a pleasure and a privilege to work with Professor Ghoniem, Lorraine Rabb and the rest of the RGD group.

The sponsors of this work, ENEL, have also been a tremendous help for providing useful feedback and essential information for the building of the slag model. This work has especially benefitted hugely from the contributions of Marco Gazzino.

This work would also not have been possible without my family's continual encouragement, love and support. They had to put up with my problems and also my failure to keep my promise to call, but are still there for me whenever I need someone to talk to.

I am also tremendously grateful to my God and savior Jesus Christ who have given me this great opportunity, and the grace and guidance throughout these two years of ups and downs in my studies and research. I am also thankful for the friends that I have met here at MIT who have encouraged me and prayed for me, especially my roommates in 10B Tang and my small group members at Tang.

Thank you, all!

Contents

Abstract 3

Acknowledgements 5

Contents 6

List of Figures 9

List of Tables 12

Nomenclature 13

Capital Letters 13

Lowercase Letters 13

Greek Letters 14

Chapter 1 Introduction 17

1.1. Thesis 17

1.2. Motivation 18

1.3. Slagging Reactor 21

1.4. Thesis Outline 22

Chapter 2 Background and Current State 24

2.1. Overview 24

2.2. Previous Slag Models 24

2.2.1. Slag Flow Model 25

2.2.2. Particle Capture Submodel 26

2.2.3. Wall Burning Submodel 27

2.3. Moving Forward 28

2.3.1. Contributions 28

2.3.2. Conclusions 29

Chapter 3 Modeling Slagging Behavior 30
3.1. Overview 30
3.2. Slag Model in a Computational Fluid Dynamics (CFD) Framework 31
3.3. Present Slag Model 32
3.3.1. Slag Flow Model 34
3.3.1.1. Mass Conservation 36
3.3.1.2. Momentum Conservation 37
3.3.1.3. Energy Conservation 40
3.3.2. Particle Capture Submodel 44
3.3.3. Wall Burning Submodel 46
3.4. Slag Properties 52
3.4.1. Properties Relevant to Slag Flow 53
3.4.1.1. Density 53
3.4.1.2. Surface Tension 54
3.4.1.3. Temperature of Critical Viscosity 55
3.4.1.4. Viscosity 56
3.4.1.5. Specific Heat Capacity 58
3.4.1.6. Thermal Conductivity 59
3.5. Conclusions 60
Chapter 4 Model Application to Coal Combustor and Gasifier 61
4.1. Overview 61
4.2. Pressurized Oxy-Coal Combustor 62
4.2.1. Computational Fluid Dynamics Framework 64
4.2.2. Simulation Results 65
4.2.2.1. Model Inputs 65
4.2.2.2. Model Outputs 68
4.3. MHI Entrained Flow Coal Gasifier 72
4.3.1. Computational Fluid Dynamics Framework 74
4.3.2. Simulation Results 75

4.3.2.1. Model Inputs 75
4.3.2.2. Model Outputs 80
4.4. Sensitivity Analysis 85
4.4.1. Particle Momentum vs. Gravity 85
4.4.2. Critical Weber Number 88
4.4.3. Temperature of Critical Viscosity 90
4.5. Validation of Wall Burning Submodel 92
4.5.1. Particle Sink Position 93
4.5.2. Wall Burning of Porous Char 94
4.6. Implementation in FLUENT 96
4.6.1. Particle Capture Submodel and Data Acquisition UDF 97
4.6.2. Slag Flow Model and Thermal Boundary Condition UDF 98
4.6.3. Discrete Phase Boundary Condition UDF 99
4.7. Conclusions 100
Chapter 5 Conclusions 102
5.1. Summary 102
5.2. Future Work and Challenges 103
5.2.1. Particle Capture Submodel 104
5.2.2. Slag Properties 105
5.2.3. Implementation in FLUENT 105
Appendix A Derivation of Constriction Correction Factor 107
Appendix B Current Code for Coupling with CFD 112
References 124

List of Figures

Figure 1-1 Ash removal in pulverized entrained-flow coal reactor with electrostatic precipitator. 18
Figure 1-2 Coal combustion product (CCP) application utilization breakout (2008) [5]. ... 20
Figure 2-1 Retarded reaction rates of trapped particle [17] 27
Figure 3-1 Slag model in CFD framework. 31
Figure 3-2 Interaction of slag flow model with particle capture and wall burning submodels. 33
Figure 3-3 Mass and heat transfer to reactor wall of slagging reactor. 34
Figure 3-4 Mass conservation with particle deposition and consumption/devolatilization. 36
Figure 3-5 Momentum conservation with momentum transfer from depositing particles... 39
Figure 3-6 Energy conservation with enthalpy and heat of fusion of depositing particles. . 40
Figure 3-7 Shrinking core reaction model. 46
Figure 3-8 Illustration of sink position, covered angle and contact radius 47
Figure 3-9 Porous char reaction model 48
Figure 3-10 Visualization of tortuosity. 49
Figure 3-11 Visualization of constriction factor. 49
Figure 3-12 Model of pore with periodic pore constrictions ; b is the focal point of the hyperbola, η_0 the axis intercept and z_0 the half length of the hyperbola 52
Figure 4-1 Geometry of the pressurized oxy-coal combustor. 62
Figure 4-2 Particle tracks colored by the residence times in second. 66
Figure 4-3 Temperature contour in K and streamlines of the fluid flow. 66
Figure 4-4 Pressurized Oxy-Combustor – CFD simulation outputs/ model inputs: (a) Heat flux to slag surface and heat loss to coolant; (b) Mass feed rate per unit area, mass deposition rate per unit area and particle volumetric consumption rate $\cdot \Delta x$; (c) Average particle temperature and gas temperature near the wall; (d) Average particle velocity in the direction of

and normal to the slag flow; (e) Average particle diameter along the wall; (f) Average particle density along the wall. 67
Figure 4-5 Temperature profiles and heat fluxes to and from the wall and slag layer. 68
Figure 4-6 Pressurized Oxy-Combustor – Model outputs; (a) Total slag thickness and solid slag thickness; (b) Slag surface, inner and outer wall temperatures and temperature at the critical viscosity; (c) Slag velocity; (d) Slag mass flow rate; (e) Slag viscosity (ordinate in logarithmic scale); (f) Heat flux to slag surface and heat loss to coolant. 70
Figure 4-7 Gasifier geometry with swirl injector configurations: (1), (2) and (3) indicate the locations of the coal injectors 72
Figure 4-8 Two-stage Air Blown Gasifier – CFD simulation outputs/ model inputs: (a) Heat flux to slag surface and heat loss to coolant; (b) Mass feed rate per unit area, mass deposition rate per unit area and particle volumetric consumption rate (cyan: mass deposition that forms molten slag); (c) Particle temperature and gas temperature near the wall; (d) Particle velocity in the direction of and normal to the slag flow; (e) Particle diameter; (f) Particle density. 77
Figure 4-9 Particle burnout contour in kg/s. 78
Figure 4-10 Particle tracks colored by the residence times in second. 78
Figure 4-11 Temperature contour in K. 79
Figure 4-12 Streamlines of the fluid flow colored by the fluid velocity in m/s. 79
Figure 4-13 Two-stage Air Blown Gasifier –Model outputs; (a) Total slag thickness and solid slag thickness; (b) Slag surface, inner and outer wall temperatures and temperature at the critical viscosity; (c) Slag velocity; (d) Slag mass flow rate; (e) Slag viscosity (ordinate in logarithmic scale); (f) Heat flux to slag surface and heat loss to coolant. 83
Figure 4-14 Influence of particle momentum transfer for different combustor inclinations; (a) $\alpha = 1.5°$ with momentum transfer;(b) $\alpha = 45°$ with momentum transfer; (c) $\alpha = 90°$ with momentum transfer;(d) $\alpha = 1.5°$ without momentum transfer. 87

Figure 4-15 Influence of critical Weber number; (a) We_{cr} = 0.1; (b) We_{cr} = 1; (c) We_{cr} = 5; (d) All particles are assumed to be trapped..... 89
Figure 4-16 Influence of temperature of critical viscosity; (a) T_{cv} = 1580 K; (b) T_{cv} = 1680 K; (c) T_{cv} = 1780 K..... 91
Figure 4-17 Sink positions for various reactor inclinations in the pressurized oxy-combustion case. 93
Figure 4-18 DNS simulation concentration profiles..... 94
Figure 4-19 Comparison with DNS simulation. 96
Figure A-1 A pore hyperbola in oblate spheroidal coordinates. 107
Figure A-2 Illustration of uncovered surface area of the particle spherical cap. 110

List of Tables

Table 3-1 Recommended values for partial molar volumes of slag constituents at 1773 K. 54
Table 3-2 Recommended values of partial molar surface tension of slag constituents at 1733 K. 55
Table 3-3 Recommended values for partial molar specific heat of slags constituents. 59
Table 4-1 Operating conditions of the burner and atomizer. 62
Table 4-2 Properties of raw coal and ash. 63
Table 4-3 Operating conditions of the gasifier burners [41] 73
Table 4-4 Properties of raw coal and ash [41,42]. 73
Table 4-5 Sensitivity analysis parameters 85
Table 4-6 Description of UDMs for model inputs. 97
Table 4-7 Description of UDMs for model outputs. 98

Nomenclature

Capital Letters

A_{eff}	Effective surface area [m^2]
D	Combustor diameter [m]
D_{bulk}	Reactant diffusion coefficient [m^2/s]
D_{eff}	Effective diffusivity of porous particles [m^2/s]
F_b	Particle buoyancy force [N]
F_w	Particle weight [N]
F_σ,	Particle capillary force [N]
G_s	Gravity contribution to slag flow [kg/m^4s]
M_p	Momentum contribution to slag flow [kg/m^4s]
$\dot{Q}'_{ex,j}$	Cell heat transfer rate/unit length [W/m]
R_p	Particle radius [m]
T_c	Coolant temperature [K]
T_{cv}	Temperature at critical viscosity [K]
T_{int}	Interface temperature [K]
T_{gas}	Bulk gas temperature [K]
T_p	Particle temperature [K]
T_s	Slag surface temperature [K]
T_{slag}	Slag mean temperature [K]
T_{wi}	Internal wall temperature [K]
T_{wo}	Outer wall temperature [K]

Lowercase Letters

a	Particle contact radius [m]
b	Tunability factor [-]
c_p	Slag specific heat [J/kg K]
$c_{p,p}$	Particle specific heat [J/kg K]
d_p	Particle diameter [m]
g	Gravitational constant [m/s^2]
h_{melt}	Particle heat of fusion [J/kg]

h_o	Convective heat transfer coefficient to coolant [W/m^{2}K]
j	Current computational cell index [-]
k	Slag thermal conductivity [W/m K]
k_{wall}	Wall thermal conductivity [W/m K]
k_{sld}	Solid slag thermal conductivity [W/m K]
$\dot{m}''_d$	Local particle deposition flux [kg/m^{2}s]
$\dot{m}'_{ex}$	Cell mass flow rate/unit length [kg/ms]
$\dot{m}''_f$	Local particle feeding flux [kg/m^{2}s]
$\dot{m}''_{melt}$	Particle phase change flux [kg/m^{2}s]
$\dot{m}''_{rb}$	Local particle rebound flux [kg/m^{2}s]
$\dot{m}'''_{vc}$	Particle volumetric consumption/devolatilization rate [kg/m^{3}s]
q_{in}	Heat flux to the slag surface [W/m^2]
q_{loss}	Heat loss to coolant [W/m^2]
s	Particle sink position [m]
u_{avg}	Local average slag velocity [m/s]
u_p	Particle velocity in the direction of slag flow [m/s]
v_p	Particle velocity in the direction normal to slag flow [m/s]
z	Distance from the slag surface [m]
z_0	Half-length of the particle constriction hyperbola [-]

Greek Letters

α	Reactor inclination from the horizontal [°]
α_{eff}	Slag thermal diffusivity [m^{2}s^{-1}]
χ_{corr}	Particle effective diffusivity correction factor [-]
η_0	Particle constriction hyperbola axis intercept [-]
δ	Total slag thickness [m]
δ_l	Molten slag thickness [m]
δ_{sld}	Slag thickness [m]
δ_{wall}	Wall thickness [m]
Δx	Cell slag surface length [m]
μ_p	Particle viscosity [Pa s]
μ_s	Slag viscosity [Pa s]
φ	Particle porosity [-]
ρ_p	Particle density [kg/m^3]
ρ_s	Slag density [kg/m^3]
σ_c	Particle constriction factor [-]

σ_{corr} Particle constriction correction factor [-]
σ_{sp} Slag-particle surface tension [N m]
σ_p Particle-air surface tension [N m]
σ_s Slag-particle surface tension [N m]
ψ Particle covered angle [°]
τ Particle tortuosity [-]
τ_{corr} Particle tortuosity correction factor [-]
τ_p Average shear stress on slag surface [Pa]
θ Contact angle [°]

Page left intentionally blank

Chapter 1 Introduction

1.1. Thesis

This thesis seeks to develop a steady-state slag flow model to describe the flow and heat transfer characteristics of slag (molten ash) in a slagging reactor.

Improvements are sought to take into consideration the temperature and composition dependent properties of slag, the contribution of momentum of captured particles and the possibility of slag resolidification. Additionally, most work on particle deposition is dedicated to a dry reactor wall. On the other hand, the mechanism of particle deposition onto a "wet" reactor wall covered with molten slag is less studied and needs more attention. Furthermore, particles that are captured by the slag layer may still contain combustibles and a prediction of their altered burning rate is necessary.

Finally, the coupling of the model with a computational fluid dynamics (CFD) framework is essential. This is because the presence of a slag layer changes the wall boundary condition of the CFD computations and this in turn has an impact on the gasification or combustion phenomena in the slagging reactor. This coupling has the potential of shedding light on many of the difficulties in reactor design and operation that have been faced thus far.

1.2. Motivation

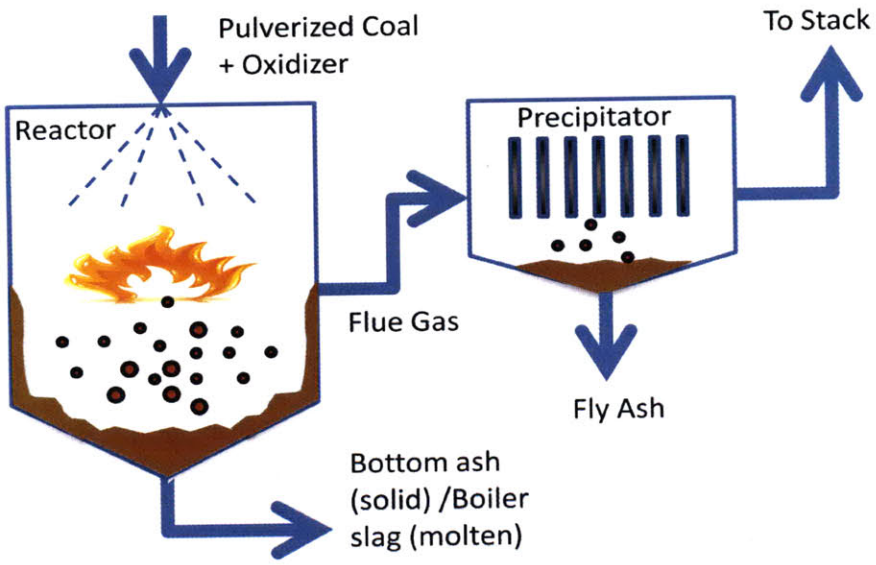

Figure 1-1 Ash removal in pulverized entrained-flow coal reactor with electrostatic precipitator.

Solid fuels such as wood, charcoal, peat, coal, grains etc. have long been used by humans to make fire. In fact, coal and wood has enabled the industrial revolution, from firing furnaces to running steam engines. Presently, coal and peat are used in electricity generation and they account for 26.5% of the world energy demand, second only to petroleum oil (34%) [1]. And coal is the most abundant fossil fuel produced in the United States and 49.8% of the electricity generated in the US is from it [2]. Researchers and policy makers have agreed that it will remain a major source of world energy in the near future for two reasons: the low cost and the wide distribution around the world [3].

Coal contains inorganic mineral matter. When burned, the inorganic compounds turn into an incombustible ash residue. In most coal boilers and reactors, coal ash is

normally captured from the flue gas (fly ash) or removed from the reactor bottom (bottom ash). When operating the reactor above the ash fusion temperature, coal ash particles become molten. This molten slag (boiler slag) is collected from a molten ash port located at the downstream end of the reactor. A general flow of fly ash and bottom ash or boiler slag production is presented in Figure 1-1.

Carbon combustion products (CCP) – fly ash, bottom ash and boiler slag – are useful in numerous applications, especially in construction, mining and agriculture. In 2008, 41.60% of fly ash, 43.82% of bottom ash and 83.31% of boiler slag produced are utilized in various applications. Fly ash combines with calcium hydroxide to form strong, durable and corrosion resistant cementitious compounds, which is widely used as cement replacement in concrete and building applications. Bottom ash is coarse and porous, making it less durable but light and it is mainly used in transportation applications such as structural fill, road base material, and as snow and ice control products. On the other hand, boiler slag particles are hard and durable with a resistance to surface wear, and are mainly used in surface coatings of asphalt in road paving and roofing shingles. A detailed breakout of the 2008 CCP application utilization is given in Figure 1-2 [4,5].

Moreover, the utility of coal ash has many environmental benefits, including reduced land disposal, reduced greenhouse gases and reduced utilization of virgin resources. For each ton of coal ash that is recycled, we save space equivalent to 455 days worth of solid waste in a landfill and energy equivalent to 24 days electricity consumption of an average home. Since coal ash has similar properties to virgin resources such as sand and fine aggregates, the natural materials can be saved for other uses [6].

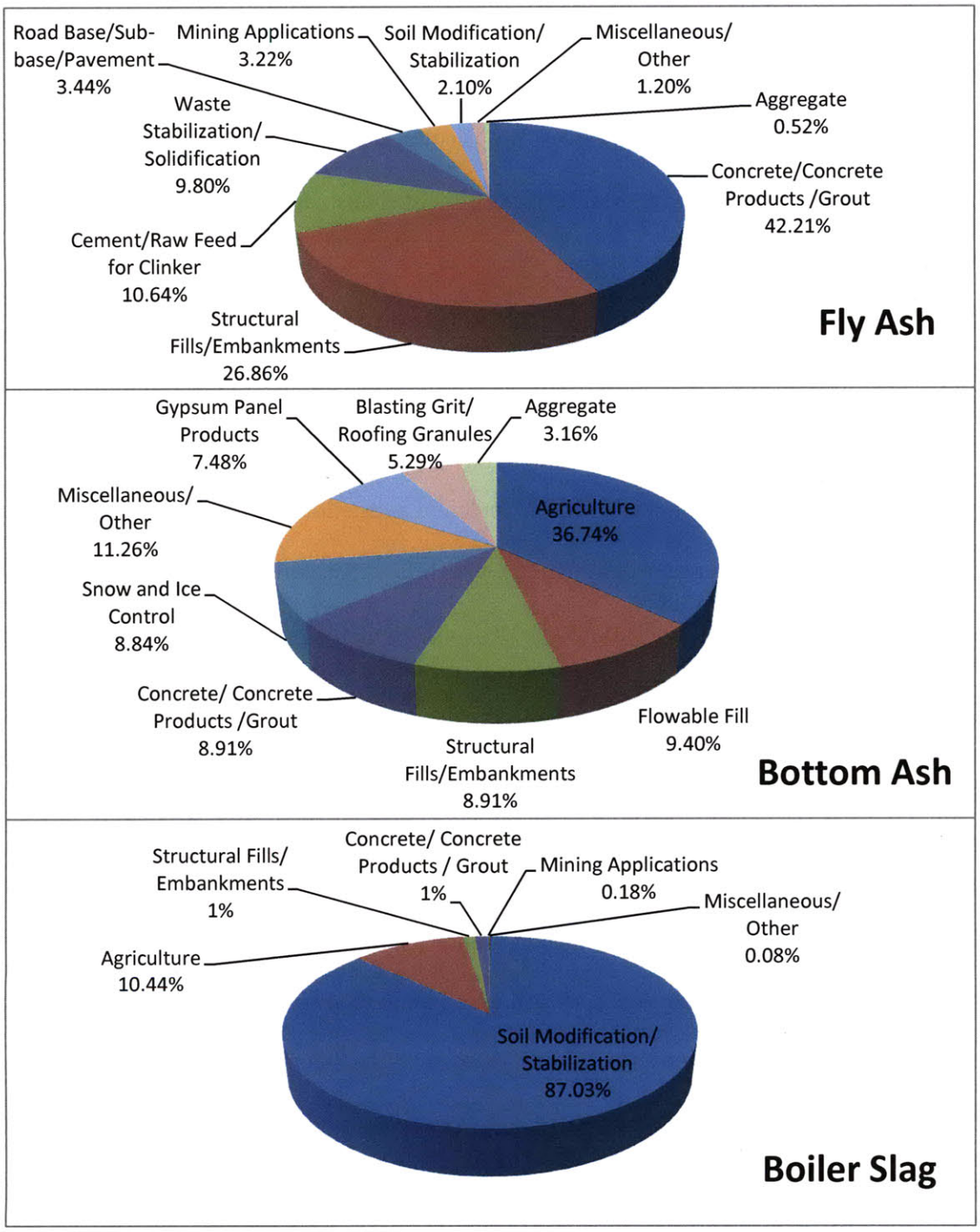

Figure 1-2 Coal combustion product (CCP) application utilization breakout (2008) [5].

1.3. Slagging Reactor

Slagging reactors, also known as wet-bottom boilers, operate at temperatures higher than the ash fusion temperature. As a result, the ash particles become molten and some of these molten particles are deposited along the wall, forming a slag layer that flows along the internal walls of the reactor chamber. The resulting boiler slag is tapped off as a liquid into a water-filled ash hopper, fracturing it instantly upon contact and crystallizing to form pellets. There are two types of slagging reactors: the slag-tap boiler, that burns crushed coal, and the cyclone boiler, that burns pulverized coal.

An advantage of a slagging reactor as opposed to a non-slagging combustor is the fact that boiler slag has in general a higher value when compared to bottom ash because of its higher durability and resistance to surface wear. Moreover, the layer of molten slag can protect the walls from corrosion and can also act as a thermal barrier. Slagging reactors are much more compact and can burn a wide range of fuels and generate a higher proportion of bottom ash than fly ash. The yield ratio of boiler ash to fly ash is 50 percent in a slag-tap boiler and 70 to 85 percent in a cyclone boiler. This ratio is higher when compared to the yield ratio of bottom ash to fly ash in a non-slagging boiler, which is about 10 to 20 percent [7,8].

However, slagging combustors have higher investment costs and higher maintenance costs. Because of wall cooling, a portion of the molten slag that flows along the internal walls of the reactor chamber may resolidify, clogging the molten ash port. Difficulties in slag discharge have been found especially in the slag tap design and when coals with high ash fusion temperature are used.

There are two methods of the handling of this problem, both of which unnecessarily reduce the system efficiency. First, a methane burner can be used to increase the temperature near the slag tap area. Alternatively, a small fraction of the combustion gas is bypassed through the slag tap instead of using a methane burner [9]. Active control solutions have also proven to be difficult due to the high temperatures within a solid fuel reactor. Measurements of slag thickness and flow within the various regions of slagging reactors are difficult during operation. At best, they can be estimated using thermocouple measurements at various locations in the refractory walls, assisted by the knowledge of the total slag flow from the slag tap, slag composition at the slag tap and heat transfer to the wall [9].

Therefore, to maintain a free passage at the molten ash port without this additional complexity, a mathematical model that predicts the slag flow and heat characteristics within a slagging reactor is necessary. A model for this purpose is developed in this thesis and the model is to be coupled with CFD computations and used as an integral part of reactor design process to avoid clogging.

1.4. Thesis Outline

Outline of the thesis is presented:

Chapter 1 gives an overview of the work presented, including the motivations and the introduction of slagging reactors for which the model is developed.

Chapter 2 provides a literature review of existing knowledge and models that have been developed for coal gasification and combustion in slagging reactors, their deficiencies and the contributions of this work to address that.

Chapter 3 describes the development of the slag model, which includes a slag flow model, a particle capture submodel and a wall burning submodel.

Chapter 4 presents the slag model application to a pilot-scale pressurized oxy-fuel combustor and a pilot scale two-stage air blown gasifier. The model inputs from CFD, the model parameters and the model outputs are presented and explained, followed by some sensitivity analyses. DNS simulations is used to validate the wall burning submodel, while the slag flow model and the particle capture submodel is implemented in a CFD framework using User Defined Functions (UDFs).

Chapter 5 summarizes the content of this thesis and provides direction for future work.

Chapter 2 Background and Current State

2.1. Overview

This chapter presents a literature review of the slag models and their submodels that are relevant to this research and proposes suggestions to bridge the gaps in those models. It will first address the models that have been developed for solid fuel gasification and combustion in slagging reactors in Section 2.2. The models that have been developed is divided into the slag flow model, that will be discussed in Section 2.2.1 and two submodels: particle capture and wall burning, that will be described in Sections 2.2.2 and 2.2.3 respectively.

Next, Section 2.3 discusses ways to improve on the current models that were presented to make the slag model more accurate and appropriate to be implemented within a CFD framework, and enumerates the proposed contribution of this work.

2.2. Previous Slag Models

Various slag models have been proposed to predict the phenomenon of slag formation in slagging coal reactors. Most of the time, the term slag model simply refers to the model of the flow and energy characteristics of slag as they form and flow down the reactor walls. At other times, the slag model is used as a general term to mean the

composition of the flow and energy characteristics model and two submodels: particle capture or particle deposition, and wall burning. In this work, the second definition is used and the model for the flow and energy characteristics is referred to as the slag flow model.

Most notable slag models in the literature include Seggiani [10] and Bockelie et al. [11] for entrained-flow coal gasifiers and Wang et al. [12] for entrained-flow coal combustors. However, only the latter integrated the slag model with particle capture and wall burning submodels. The former two publications assumed that all ash particles are trapped and that the particles that are captured by the wall no longer contain combustibles, i.e. pure ash.

In the next sections, we will explore the various slag flow models, as well as different submodels that have been introduced in the literature.

2.2.1. Slag Flow Model

Several models have been proposed to predict slag formation and its flow and energy characteristics in entrained-flow reactors. Seggiani [10] has proposed an analytical time-varying slag accumulation and flow model to predict both the solid and molten slag layer thicknesses for the gasifier of the IGCC plant in Puertollano, Spain. As an extension to that, Bockelie et al. [11] introduced a numerical scheme for predicting the molten layer thickness. Similarities in both models include the assumption of negligible shear stress at the slag surface and a linear temperature profiles across both the solid and molten slag layers. Benyon [9] used a simplified version of Seggiani's model, citing instability of the

model as a problem, and justified the simplification with an assumption that the sensible heat of the slag flow is minor in comparison to the heat flux to the slag layer. Wang et al. [12] also adopted a similar approach to Seggiani [10] but included an important feature, that is, the influence of particle deposition on the slag flow momentum. However, Wang et al.'s work stopped short of applying energy conservation to predict the slag temperature, and hence could not predict resolidification.

2.2.2. Particle Capture Submodel

There are suggestions in the literature that particles are more readily captured by a reactor wall that is covered by molten slag layer. A model that is able to predict the probability of capture but does not differentiate between particles of different sizes and velocities was given in Shimizu and Tominaga [13]. Benyon [9] has earlier asserted that a crude check of the capture criterion be made based on the angle and velocity of particle impact. Alternatively, Tominaga et al. [14] suggested that the criterion be based on the viscosities of the slag and the incoming particles at the time of collision. Montagnaro and Salatino [15] has confirmed using order of magnitude estimates that particle plunging and overlaying are not likely to occur but did not provide a conclusive capture criterion. In contrast, Emory and Berg [16] brought up the role of a vapor film between the particle and slag layer which introduced another layer of complication. A simple but more encompassing capture criterion is necessary.

2.2.3. Wall Burning Submodel

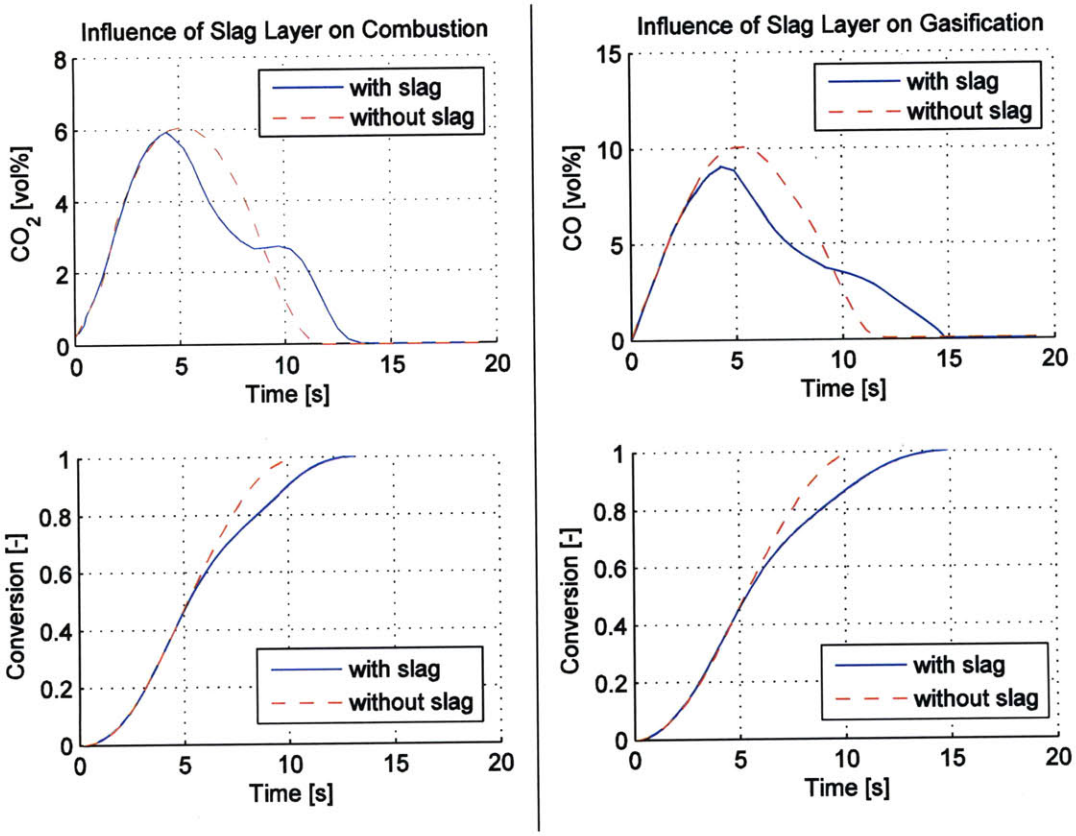

Figure 2-1 Retarded reaction rates of trapped particle [17].

Besides ash particles, particles with combustibles may be captured by the slag layer and experiments have shown that these particles continue to burn albeit at a slower rate in both gasification and combustion environments. Figure 2-1 shows experimental results obtained by Noda et al. [17] that substantiate this notion of retarded particle reaction rates – the recorded time histories of CO_2 concentration in an oxidizing environment and of CO

concentration in an reducing environment and their corresponding conversion curves. During the first 5 seconds, the conversion rates do not differ between the free and the trapped particles. The authors suggest that this is because of the simultaneous volatile matter and fixed carbon consumption. However, when trapped, the fixed carbon combustion rate is delayed as evidenced by the slope of that is less steep when compared to that of the free particle.

To take into consideration these retarded reaction rates, Wang et al. [12] have proposed the concept of an effective outer reaction surface when particles are trapped, but recommended that the wall burning mechanism be studied more thoroughly after stating the deficiencies of their model. The proposed model assumes a solid char particle where the reaction only takes place on the outer surface of the particles. A reaction model with this assumption is known as a shrinking core model. However, coal particles are known to be very porous. Therefore, other reaction models that consider the reactions on the internal surface areas are often used and a wall burning model needs to be developed to reflect these considerations in those reaction models.

2.3. Moving Forward

2.3.1. Contributions

In this work, we combine the slag model described in Seggiani [10] with the momentum transfer of captured particles introduced in Wang et al.[12]. Moreover, an

energy balance is derived for the steady-state case, and a cubic temperature profile across the molten slag layer is used to replace the linear temperature profile assumed in Seggiani [10] to obtain an analytical steady-state model that can be integrated into a CFD framework.

A deterministic slag capture criterion is proposed in Section 3.3.2. The criterion involves distinguishing between different phases of the slag layer and the impacting particles, as well as the velocities and trajectories of the impacting particles. This submodel also deterministically predicts the particles that are captured, as opposed to the probabilistic submodel used in Wang et al. [12] which was based on Shimizu and Tominaga [13].

Section 3.3.3 introduces a wall burning submodel for porous char particles using the concept of an equivalent particle with a modified effective diffusivity. This modified diffusivity value is used to consider the effect of the access loss of reactants to the inner surfaces of the porous particles and the resulting increased reactant travel distances.

2.3.2. Conclusions

This chapter gave some background knowledge and the current state in the area of modeling the slagging phenomenon. The chapter also points out the limitations of the different models in the literature and listed measures that are suggested in this work to address these deficiencies. With a common knowledge established, the reader can better understand the basis on which this work is built, as well as the motivations and the assumptions in this work.

Chapter 3 Modeling Slagging Behavior

3.1. Overview

This chapter seeks to describe the behavior of slag (molten ash) in a wet bottom reactor. This model is based on previous slag models in the literature that each have their limitations as described in Chapter 2, and expanded to include essential additions and modifications to increase the fidelity of the slag models and submodels.

First, the inputs of the slag model as well as the outputs of the slag model are described in the context of a Computational Fluid Dynamics (CFD) framework, in which the slag model is used to predict the wall boundary conditions of the CFD computation. Section 3.2 also briefly explains the methodology used in incorporating this slag model in CFD.

Next, Section 3.3 presents the development of the slag model and its submodels. The assumptions that are made and the model derivation is described in detail. Section 3.3.1 focuses on the slag flow model and includes the application of mass, momentum and energy conservation while Section 3.3.2 and Section 3.3.3 introduce the particle capture and wall burning submodels respectively.

Slag properties are also found to vary with temperature and with its ash composition. Therefore, Section 3.4 presents some correlations and models found in the literature for the prediction of slag properties.

3.2. Slag Model in a Computational Fluid Dynamics (CFD) Framework

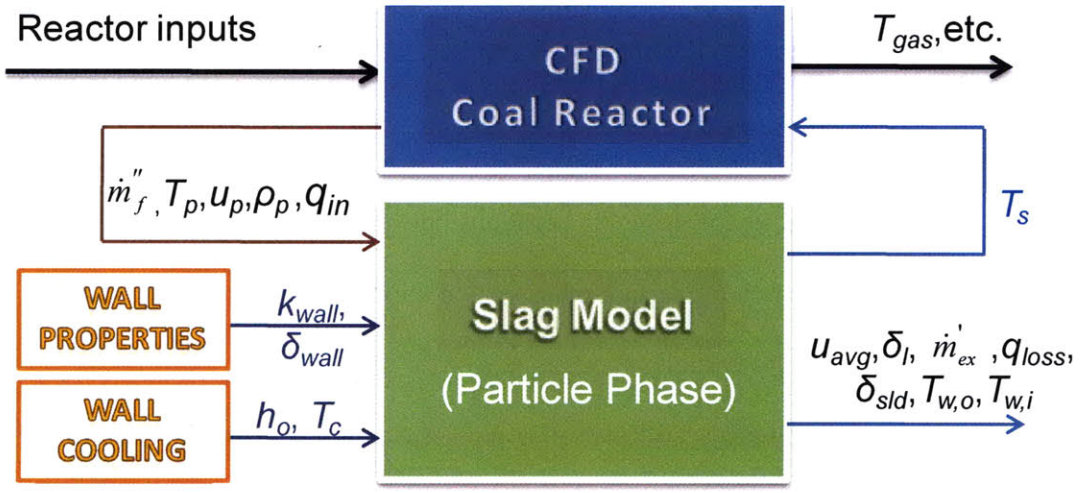

Figure 3-1 Slag model in CFD framework.

The slag model is developed to better predict the wall boundary conditions of a CFD framework for modeling coal combustion or gasification. These include the computed wall temperature that is used as the thermal boundary condition of the reactor walls (see Figure 3-1) and the particle capture/reflect boundary condition at the wall in the discrete phase (not depicted in the figure).

For the thermal boundary condition, the combustor or gasifier simulation supplies the slag model inputs: the local per unit area particle feeding rate $\dot{m}''_f$, the particle temperature T_p, the particle velocity in the direction of slag flow u_p, the slag density ρ_p and the per unit area heat flux to the slag surface q_{in}. The slag model computes the slag surface

temperature, T_s, that is fed back as the wall boundary condition for the next CFD iteration, as well as the average slag velocity, u_{avg}, the molten and solid slag thickness, δ_l and δ_{sld}, the inner and the outer wall temperatures, T_{wi} and T_{wo}, the mass flow rate per unit length, $\dot{m}'_{ex}$, and the per unit area heat flux to the coolant, q_{loss}. For this slag model simulation, the wall properties and the wall cooling conditions have to be supplied and these inputs include the wall thermal conductivity k_{wall}, the wall thickness δ_{wall}, the heat transfer coefficient to the coolant h_o and the coolant temperature T_c. Iterations between the CFD solution and the slag model are performed with every particle phase calculation of the reactor until steady-state is achieved in both fluid and particle phases.

The slag model employs an Eulerian approach which uses the readily defined CFD mesh cells. For each control volume or cell, computations are performed using an analytical model to reduce computational time. Therefore, the accuracy of this model is dependent on the CFD mesh resolution along the reactor walls.

Conversely, the particle phase boundary condition is determined by the particle capture submodel that is described in Section 3.3.2. This boundary condition is deterministic on a particle-to-particle basis and not restricted to the CFD mesh resolution as the thermal boundary condition.

3.3. Present Slag Model

The present slag model consists of the slag flow model and two submodels: particle capture and wall burning (see Figure 3-2). Besides the inputs from the CFD, these

submodels supply the necessary inputs for the slag flow model. The particle capture submodel predicts the particle deposition rate $\dot{m}_d''$, from the particle feeding rate $\dot{m}_f''$ by subtracting the particle rebound rate $\dot{m}_{rb}''$:

$$\dot{m}_d'' = \dot{m}_f'' - \dot{m}_{rb}'' \tag{3-1}$$

A detailed description of the particle capture criterion is given is Section 3.3.2.

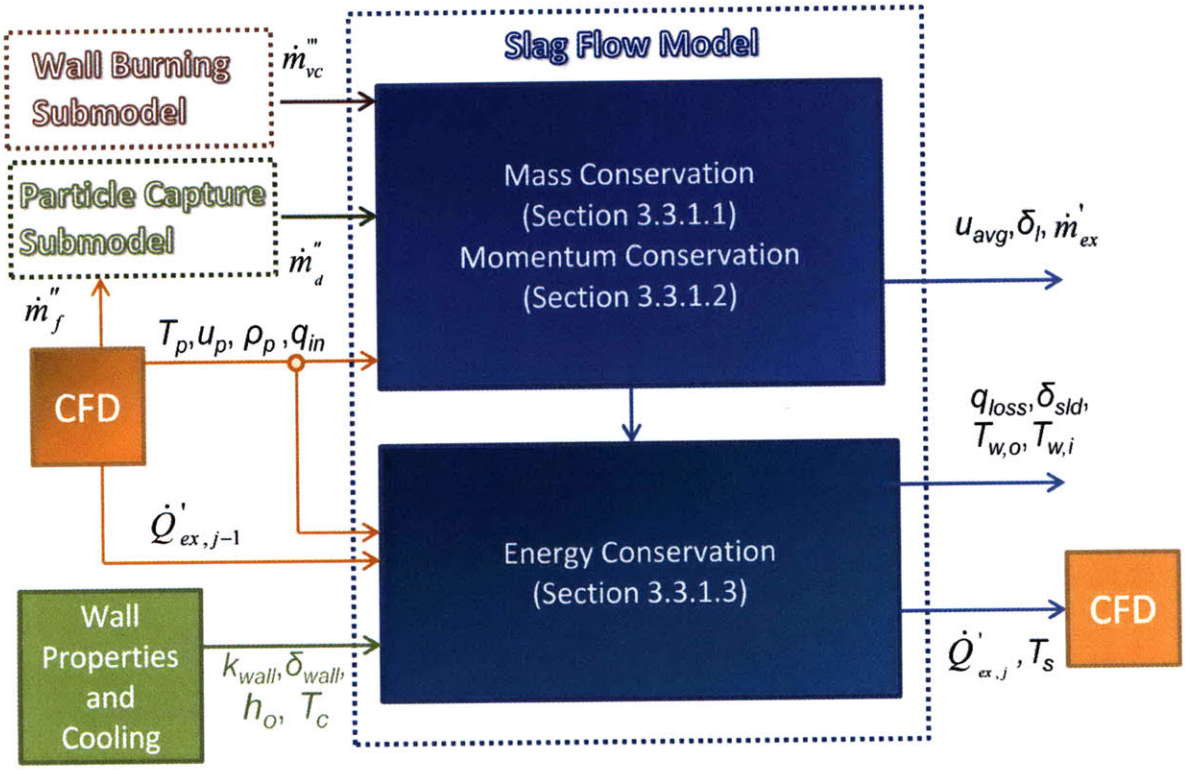

Figure 3-2 Interaction of slag flow model with particle capture and wall burning submodels.

On the other hand, the wall burning submodel proposes a correction factor for predicting particle devolatilization and consumption rate when trapped in a slag layer. This correction factor, which is presented in Section 3.3.3, is supplied to the CFD and the computation is carried out by the particle devolatilization and consumption models that are chosen by the user.

3.3.1. Slag Flow Model

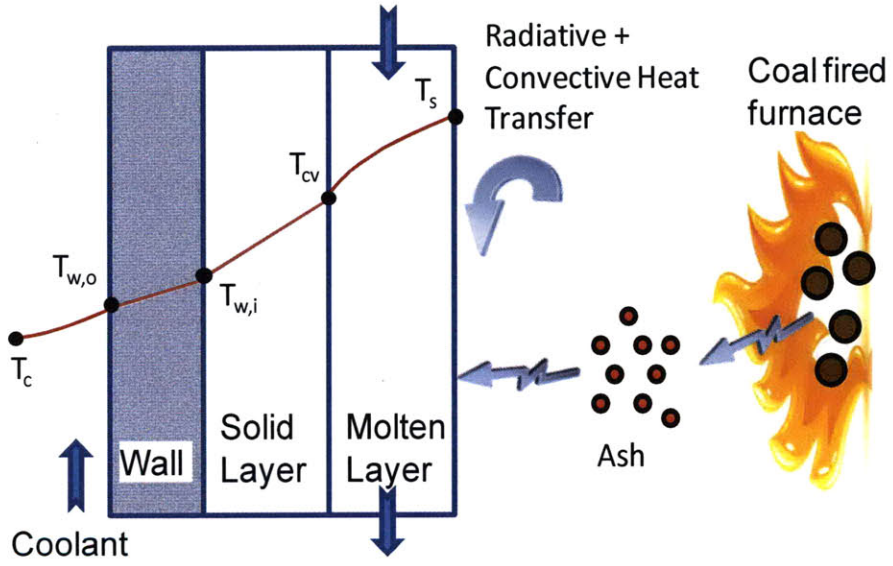

Figure 3-3 Mass and heat transfer to reactor wall of slagging reactor.

Figure 3-3 shows the mass and heat transfer processes that are involved in a slagging reactor that are considered in the development of the slag flow model. A fraction of the ash particles from the furnace that impacts the reactor wall is captured by the slag

layer, increasing the slag thickness and the total momentum and energy of the slag layer through momentum and enthalpy transfer. Heat is also transferred to the slag layer via radiative and convective modes.

Ultimately, the slag flow model can be broken down into mass, momentum and energy conservation, as shown in Figure 3-2. The conservation equations are derived under the following assumptions:

1. The slag thickness is very small compared to the reactor diameter ($\delta_l + \delta_{sld} << D$).
2. The slag flow is unidirectional, i.e. no reverse flow or flow inhibition is allowed. If necessary, flow in the azimuthal direction of the reactor can be considered using an averaging method.
3. The shear stress on slag surface, τ_p, is dominated by the depositing particles.
4. The transition temperature between the resolidified and molten slag layers is the slag temperature at the critical viscosity, T_{cv}, which is dependent on the type of coal used as a feedstock (see Section 3.4).
5. The temperature profile across the slag layer is cubic with the following boundary conditions:

$$z = 0; \quad T = T_s; \quad \frac{\partial T}{\partial z} = -\frac{q_{in}}{k}$$

$$z = \delta_l; \quad T = T_{cv}; \quad \frac{\partial^2 T}{\partial z^2} = 0$$

where k is the slag thermal conductivity and z the distance from slag surface.

The temperature profile across the slag layer is thus given by:

$$T = T_{cv} + \left(1.5(T_s - T_{cv}) - \frac{q_{in}\delta_l}{2k}\right)\left(1 - \frac{z}{\delta_l}\right) - \left(0.5(T_s - T_{cv}) - \frac{q_{in}\delta_l}{2k}\right)\left(1 - \frac{z}{\delta_l}\right)^3 \quad (3\text{-}2)$$

6. Slag properties are evaluated at the slag mean temperature based on correlations in Section 3.4.

3.3.1.1. Mass Conservation

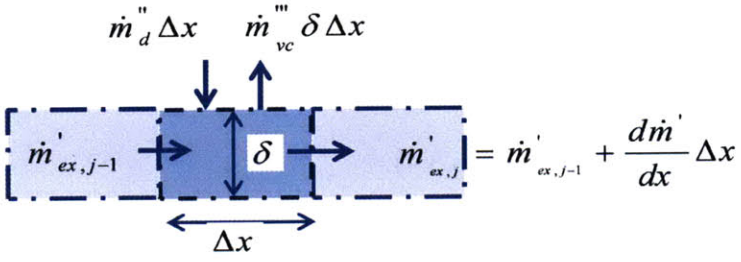

Figure 3-4 Mass conservation with particle deposition and consumption/devolatilization.

Figure 3-4 illustrates the mass balance for a computational cell j within the slag layer. We assume steady-state in which the mass accumulation rate is zero. Hence, particle deposition rate per unit area $\dot{m}''_d$, particle consumption and devolatilization rate per unit volume $\dot{m}'''_{vc}$ and exit mass flow rate per unit length $\dot{m}'_{ex}$ are related as follows:

$$\begin{aligned} \dot{m}'_{ex,j} &= \Delta\dot{m}' + \dot{m}'_{ex,j-1} = \dot{m}''_{d}\,\Delta x - \dot{m}'''_{vc}\,\delta\,\Delta x + \dot{m}'_{ex,j-1} \\ &= \sum_{i=0}^{j} (\dot{m}''_{d,i}\,\Delta x - \dot{m}'''_{vc,i}\,\delta_i\,\Delta x) \end{aligned} \tag{3-3}$$

where j is the current computational cell index and Δx is the slag surface length. The particle deposition rate $\dot{m}''_d$ is computed using Equation (3-1) and the particle consumption and devolatilization rate can be computed with the help of the correction factor that is introduced in Section 3.3.3.

The exit mass flow rate per unit length for each cell, $\dot{m}'_{ex,j}$, is given by the average slag velocity u_{avg} and molten slag thickness δ_l:

$$\dot{m}'_{ex,j} = \frac{\dot{m}_{ex,j}}{\pi D} = \rho_{s,j} \int_0^{\delta_{l,j}} u_j(z)\, dz = \rho_{s,j}\, \delta_{l,j}\, u_{avg,j} \tag{3-4}$$

where D is the combustor diameter and ρ_s the slag density.

3.3.1.2. Momentum Conservation

Given assumption 1 in Section 3.3.1, the momentum equation can be expressed in linear coordinates. Furthermore, in the thin layer inertia free limit, the momentum balance equation can be written as:

$$\frac{d}{dz}\left(\mu_s \frac{du}{dz}\right) = -\rho_s g \sin\alpha \tag{3-5}$$

with
$$z = 0; \quad \mu_s \frac{\partial u}{\partial z} = -\tau_p$$

$$z = \delta_l; \quad u = 0$$

where τ_p is the average shear stress on the slag surface. This shear stress is assumed to be dominated by the depositing particles (Assumption 3). The derivation of the shear stress on the slag surface is based on the conversion of the kinetic energy of trapped particle to the impelling work of deposition, assuming that no energy is loss in this conversion process:

$$\tau_p \pi D \Delta x \Delta x = \frac{1}{2} u_p^2 \dot{m}_d'' \pi D \Delta x \Delta t \tag{3-6}$$

where
$$\frac{\Delta x}{\Delta t} = u_{avg} \tag{3-7}$$

Using Equations (3-3), (3-4), (3-6) and (3-7), this average shear stress can be computed as:

$$\tau_p = \frac{u_p^2 \dot{m}_d''}{2 u_{avg}} = \frac{u_p^2 \dot{m}_d'' \rho_s \delta_l}{2 \sum_{i=0}^{j} (\dot{m}_{d,i}'' \Delta x - \dot{m}_{vc,i}''' \delta_i \Delta x)} \tag{3-8}$$

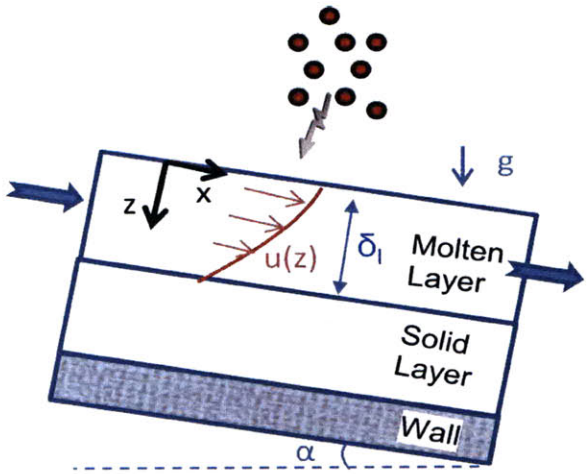

Figure 3-5 Momentum conservation with momentum transfer from depositing particles.

Applying assumption 6 and Equation (3-8), the solution of Equation (3-5) gives:

$$u(z) = -\frac{\rho_s g \delta_l^2 \sin\alpha}{2\mu_s}\left(1-\frac{z}{\delta_l}\right)^2 + \left(\tau_p \delta_l + \frac{\rho_s g \delta_l \cos\beta}{2\mu_s}\right)\left(1-\frac{z}{\delta_l}\right) \tag{3-9}$$

Combining Equations (3-3) through (3-9), the molten slag thickness δ_l and the average slag velocity u_{avg} can be expressed as follows:

$$\delta_l = \left(\frac{\dot{m}'_{ex,j}}{M_p + G_s}\right)^{\frac{1}{3}} = \left(\frac{\sum_{i=0}^{j}(\dot{m}''_{d,i}\Delta x - \dot{m}'''_{vc,i}\delta_i \Delta x)}{M_p + G_s}\right)^{\frac{1}{3}} \tag{3-10}$$

$$u_{avg} = \frac{\left(\sum_{i=0}^{j}(\dot{m}''_{d,i}\Delta x - \dot{m}'''_{vc,i}\delta_i \Delta x)\right)^{\frac{2}{3}}\left(M_p + G_s\right)^{\frac{1}{3}}}{\rho_s} \tag{3-11}$$

where M_p and G_s are driving forces for the slag flow and are defined as:

$$M_p = \frac{\rho_s^2 u_p^2 \dot{m}_d^{''}}{4\mu_s \sum_{i=0}^{j} (\dot{m}_{d,i}^{''} \Delta x - \dot{m}_{vc,i}^{'''} \delta_i \Delta x)} \tag{3-12}$$

$$G_s = \frac{\rho_s^2 g \sin\alpha}{3\mu_s} \tag{3-13}$$

3.3.1.3. Energy Conservation

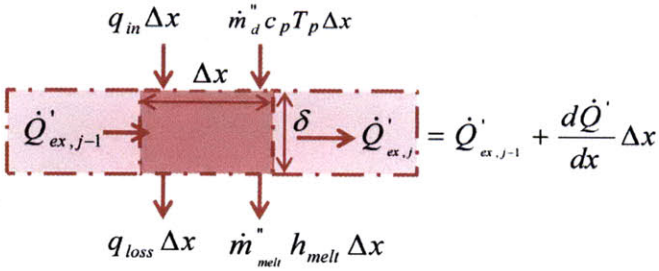

Figure 3-6 Energy conservation with enthalpy and heat of fusion of depositing particles.

Similar to mass conservation, energy conservation for the molten slag layer for a particular computational cell *j* at steady-state (see Figure 3-6) is:

$$\begin{aligned} \dot{Q}'_{ex,j} &= \Delta\dot{Q}' + \dot{Q}_{ex,j-1} \\ &= q_{in}\Delta x - q_{loss}\Delta x - \dot{m}_{melt}^{''} h_{melt}\Delta x + \dot{m}_d^{''} c_{p,p} T_p \Delta x + \dot{Q}_{ex,j-1} \end{aligned} \tag{3-14}$$

where $\dot{Q}'_{ex}$ is the exit heat transfer rate, $\dot{m}'_{melt}$ the melting mass rate per unit area, h_{melt} the

heat of fusion, $c_{p,p}$ the slag specific heat and T_p the depositing particle temperature.

Employing the proposed cubic temperature profile across the molten slag layer, the exit heat transfer rate for each cell, $\dot{Q}_{ex}^{'}$, can also be obtained by the following integration:

$$\begin{aligned}\dot{Q}_{ex,j}^{'} &= \rho_{s,j}\, c_{p,j} \int_0^{\delta_{l,j}} u_j(z)\, T(z)\, dz \\ &= \frac{\rho_{s,j}\, c_{p,j}\, \delta_{l,j}^3}{\mu_{s,j}} \left[\frac{q_{in}\delta_{l,j}}{2k_j}\left(\frac{11\rho_{s,j} g \sin\alpha}{120} + \frac{4\mu_{s,j} M_{p,j}}{15\rho_{s,j}} \right) \right. \\ &\quad \left. + T_{s,j}\left(\frac{61\rho_{s,j} g \sin\alpha}{240} + \frac{4\mu_{s,j} M_{p,j}}{5\rho_{s,j}} \right) + T_{\text{int}}\left(\frac{19\rho_{s,j} g \sin\alpha}{240} + \frac{\mu_{s,j} M_{p,j}}{5\rho_{s,j}} \right) \right]\end{aligned} \tag{3-15}$$

where M_p is given by Equation (3-12) and T_{int} is the interface temperature which varies depending on the existence of a solid slag layer. The interface temperature is defined as:

$$T_{\text{int},j} = \begin{cases} T_{wi.j}; & \textit{for} \quad T_{wi.j} \geq T_{cv} \quad \& \quad \delta_{sld} = 0 \\ T_{cv}; & \textit{for} \quad T_{wi,j} < T_{cv} \quad \& \quad \delta_{sld} \neq 0 \end{cases} \tag{3-16}$$

where T_{cv} is the temperature at the critical viscosity as defined in assumption 4 and T_{wi} is the internal wall temperature. In this derivation, axial conduction has been neglected. This assumption is warranted upon inspection of the Péclet number which is found to be in the order of 1000.

Axial heat conduction is also neglected along the solid slag layer and reactor wall. Thus, the heat flux to the coolant is the heat loss from the molten slag layer q_{loss}, yielding the following equations:

$$q_{loss} = \frac{k_{sld}}{\delta_{sld}}(T_{cv} - T_{wi}) \tag{3-17}$$

$$q_{loss} = \frac{k_{wall}}{\delta_{wall}}(T_{wi} - T_{wo}) \tag{3-18}$$

$$q_{loss} = h_o(T_{wo} - T_c) \tag{3-19}$$

where k_{sld} is the solid slag thermal conductivity.

Solving Equations (3-14) through (3-19) simultaneously and setting the value of $\dot{Q}'_{ex,0}$ to zero, the unknowns $\dot{Q}'_{ex,j}$ (Equation (3-15)), q_{loss}, T_s, T_{wi}, T_{wo} and δ_{sld} can be computed for each computational cell:

$$q_{loss,j} = \begin{cases} \dfrac{\left(\begin{array}{l} q_{in}(\pi D\Delta x - C_1(C_2 + C_3\dfrac{\delta_l}{3k})) - C_1(C_3 + C_4)T_c \\ -\dot{m}''_{melt}h_{melt}\Delta x\pi D + \dot{m}''_d c_{p,p}T_p\Delta x\pi D \end{array}\right)_j + \dot{Q}'_{ex,j-1}\pi D}{\left(\pi D\Delta x + C_1C_3\dfrac{\delta_l}{1.5k} + C_1(C_3 + C_4)\left(\dfrac{\delta_{wall}}{k_{wall}} + \dfrac{1}{h_o}\right)\right)_j}; \\ \qquad for\ T_{wi.j} \geq T_{cv} \\ \dfrac{\left(\begin{array}{l} q_{in}(\pi D\Delta x - C_1(C_2 + C_3\dfrac{\delta_l}{3k})) - C_1(C_3 + C_4)T_{cv} \\ -\dot{m}''_{melt}h_{melt}\Delta x\pi D + \dot{m}''_d c_{p,p}T_p\Delta x\pi D \end{array}\right)_j + \dot{Q}'_{ex,j-1}\pi D}{\left(\pi D\Delta x + C_1C_3\dfrac{\delta_l}{1.5k}\right)_j}; \\ \qquad for\ T_{wi,j} < T_{cv} \end{cases} \tag{3-20}$$

where

$$C_1 = \frac{\rho_{s,j}\,\pi\, D c_{p,j} \delta_{l,j}^3}{\mu_{s,j}}$$

$$C_2 = \frac{\delta_{l,j}}{2k_j}\left(\frac{11\rho_{s,j} g \sin\alpha}{120} + \frac{4\mu_{s,j} M_{p,j}}{15\rho_{s,j}}\right)$$

$$C_3 = \frac{61\rho_{s,j} g \sin\alpha}{240} + \frac{4\mu_{s,j} M_{p,j}}{5\rho_{s,j}}$$

$$C_4 = \frac{19\rho_{s,j} g \sin\alpha}{240} + \frac{\mu_{s,j} M_{p,j}}{5\rho_{s,j}}$$

$$T_s = \begin{cases} q_{loss}\left(\dfrac{\delta_{wall}}{k_{wall}} + \dfrac{1}{h_o} + \dfrac{\delta_l}{1.5k}\right) + q_{in}\dfrac{\delta_l}{3k} + T_c; & for\ T_{wi.j} \geq T_{cv} \\ \left(q_{loss} + \dfrac{q_{in}}{2}\right)\dfrac{\delta_l}{1.5k} + T_{cv}; & for\ T_{wi,j} < T_{cv} \end{cases} \quad (3\text{-}21)$$

$$T_{wi} = q_{loss}\left(\frac{\delta_{wall}}{k_{wall}} + \frac{1}{h_o}\right) + T_c \quad (3\text{-}22)$$

$$T_{wo} = \frac{q_{loss}}{h_o} + T_c \quad (3\text{-}23)$$

$$\delta_{sld} = \begin{cases} 0; & for\ T_{wi.j} \geq T_{cv} \\ k_{sld}\left(\dfrac{T_{cv} - T_c}{q_{loss}} - \dfrac{\delta_{wall}}{k_{wall}} - \dfrac{1}{h_o}\right); & for\ T_{wi,j} < T_{cv} \end{cases} \quad (3\text{-}24)$$

3.3.2. Particle Capture Submodel

The objective of this submodel is to derive a deterministic capture criterion to predict which particle is captured and which is rebounded. Using this criterion, the particle deposition rate that is needed in Section 3.3.1 can be determined by using Equation (3-1). Capture is defined to include both particles trapped on the surface as well as within the slag layer. Order of magnitude estimates by Montagnaro and Salatino [15] have shown that particles do not penetrate the slag surface unless:

$$d_p v_p > 36\frac{\mu_p}{\rho_p} \tag{3-25}$$

where ρ_p is the particle density, v_p the normal component of particle velocity, d_p the particle diameter and μ_p the particle viscosity. Since under typical operation conditions, the Equation (3-25) is not fulfilled, a criterion for particle capture on the slag surface is sufficient.

The particle phase and the slag phase contribute to whether a particle is captured. Experiments have shown that when both are in the liquid phase, the liquid particle is always captured [18]. This is analogous to the approach used by Richards [19] to determine capture by comparing particle viscosity to the critical viscosity (melting viscosity). On the other hand, when dealing with solid-solid interaction, it is assumed that all particles are rebounded.

For the case in which the particle is in the liquid phase and the slag is in the solid state, or when the slag is in the solid phase and the particle in the molten state, the sticking tendency depends on surface "stickiness" which is dependent on the surface tension, the normal velocity and the diameter. The impacted surface also contributes to the determining factors of capture. Therefore, a simplified argument for capture vs. no capture is based on the competition between the kinetic energy of the particles and the interfacial surface tension energy between the particles and the slag surface. A dimensionless number that compares these two quantities is the Weber number, given by:

$$We \equiv \frac{Particle\ Kinetic\ Energy}{Surface\ Tension\ Energy} = \frac{\rho_p v_p^2 d_p}{\sigma_{sp}} \tag{3-26}$$

where σ_{sp} is the slag-particle surface tension that is determined using the Young's equation:

$$\sigma_{sp} = \sigma_p - \sigma_s \cos\theta \tag{3-27}$$

where the contact angle θ is experimentally determined by Shannon et al. [20] to be 120°.

A particle is rebounded when its Weber number exceeds a critical value. This critical value has been set to 1. It is also noted that the range of Weber number of interest excludes the possibility of wall jetting that is described in Senda et al. [21].

3.3.3. Wall Burning Submodel

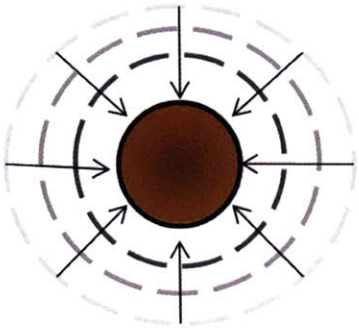

Figure 3-7 Shrinking core reaction model.

Given the observations that particles with combustibles burn at a slower rate when trapped in a slag layer [17], it is necessary to model their wall burning characteristics. Noda et al. [17] have attributed this retarded reaction rates to the loss of surface area. Wang et al. [12] has adopted this concept by introducing an effective surface area A_{eff} for a solid sphere which would be suitable when using the shrinking core combustion/gasification model, in which reactions are assumed to take place on the outer particle surfaces only (see Figure 3-7):

$$A_{eff} = 2\pi R_P (R_P + \sqrt{R_P^2 - a^2}) \tag{3-28}$$

where R_p is the particle radius and a the contact radius (see Figure 3-8).

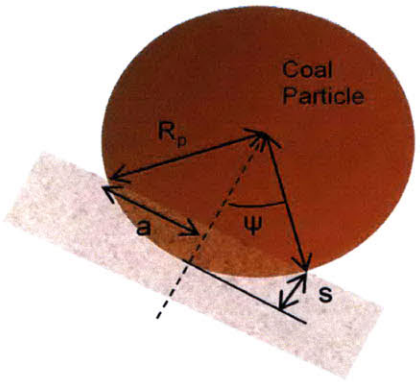

Figure 3-8 Illustration of sink position, covered angle and contact radius.

The contact radius, a, can be determined by considering the balance of forces that are acting on the coal particle. According to simulations done by Shannon [20], for particles of sizes up to 100μm, the particle's settling time is less than 5μs, which is negligible when compared to the time needed to travel from one computational cell to the next. This justifies the assumption of quasi-steadiness and as a result, the added-mass force and drag force will have no effect on the sink position of the particles. The three forces that act on the particle are the capillary force F_σ, weight F_w and buoyancy force F_b:

$$F_\sigma = 2\pi R_P\left(\frac{s}{R_P} - 1 - \cos\theta\right) \tag{3-29}$$

$$F_w = \rho_P g \cos\alpha \frac{4}{3}\pi R_P^3 \tag{3-30}$$

$$F_b = -\rho_P g \cos\alpha\, \pi s\left(R_P s - \frac{s^3}{3}\right) \tag{3-31}$$

where s is the sink position as shown in Figure 3-8. At equilibrium, the sum of the three forces is zero and herewith the sink position can be determined and consequently, the contact radius a and covered angle ψ (Figure 3-8) through geometry.

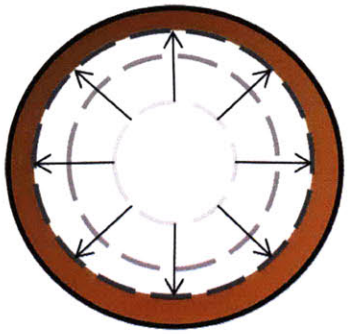

Figure 3-9 Porous char reaction model.

However, coal particles are known to be very porous. This means that the reaction surface area within the particle is larger when compared to the external surface area. Therefore, it is common to consider the reactions as primarily occurring on the internal surfaces of the solid [22,23] (see Figure 3-9).

To take this fact in consideration, instead of employing an effective surface area as described above, a modified effective diffusivity is used to reflect the increased diffusion resistance and distance. The modified diffusivity D_{mod} is based on the definition of effective diffusivity D_{eff} as defined in [24]:

$$D_{\text{mod}} = D_{eff}\left(\frac{\sigma_{Corr}}{\tau_{Corr}}\right) = \left(\frac{D_{bulk}\varphi\sigma_C}{\tau}\right)\left(\frac{\sigma_{Corr}}{\tau_{Corr}}\right) = \left(\frac{D_{bulk}\varphi\sigma_C}{\tau}\right)\chi_{corr} \tag{3-32}$$

$$\chi_{corr} = \frac{\sigma_{Corr}}{\tau_{Corr}} \tag{3-33}$$

where D_{bulk} is the reactant diffusion coefficient, φ the particle porosity , σ_c the constriction factor, τ the tortuosity and χ_{corr} the effective diffusivity correction factor. Tortuosity τ is the ratio of actual distance a molecule travels between two points to the shortest distance between them while the constriction factor σ_c accounts for the variation in cross-sectional area that is normal to diffusion (see Figure 3-10 and Figure 3-11).

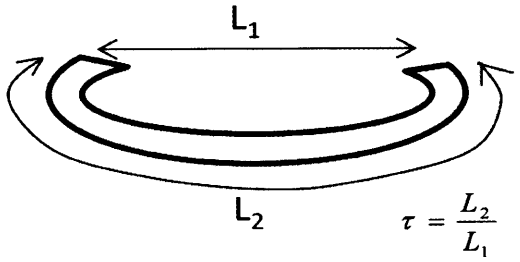

Figure 3-10 Visualization of tortuosity.

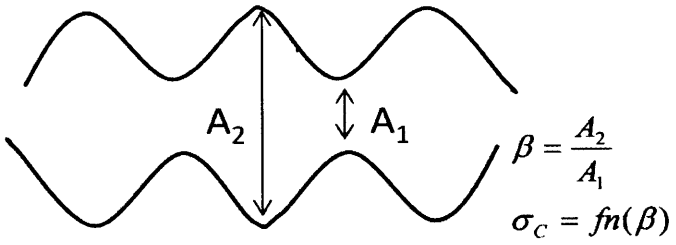

Figure 3-11 Visualization of constriction factor.

The modified effective diffusivity has thus two correction factors – tortuosity correction factor τ_{corr} and constriction correction factor σ_{corr}. The former accounts for the increased average distance that reactants have to travel through the labyrinth within a porous char due to loss of access resulting from being covered by slag. The tortuosity correction factor τ_{corr} is defined as the ratio of average distances to every point within the free particle to a trapped particle:

$$\tau_{corr} = \frac{\bar{l}_{trapped}}{\bar{l}_{free}} \tag{3-34}$$

The average distances within a free particle and a trapped particle are derived using spherical coordinates:

$$\bar{l}_{trapped} = \frac{R_P}{4} \tag{3-35}$$

$$\bar{l}_{free} = \frac{R_P}{8}(1+\cos\psi) + \frac{R_P B}{80} \tag{3-36}$$

where ψ is the covered angle (see Figure 3-8) and B is defined as follows:

$$B = -10 + 32m - 23m\cos^2\psi + 5m\cos^3\psi + 15\cos^4\psi - 30\ln 2\cos^3\psi + 15\ln 2\cos^5\psi - 29m\cos\psi + 15\ln 2\cos\psi + 25\cos^2\psi - 15\cos^4\psi + 15\cos\psi(\cos^2\psi - 1)^2 \ln[m^{-1}(1-\cos\psi + m)] \quad (3\text{-}37)$$

where $m = \sqrt{2-2\cos\psi}$

Hence, the tortuosity correction factor is obtained by the following:

$$\tau_{corr} = \frac{\bar{l}_{trapped}}{\bar{l}_{free}} = \frac{1+\cos\psi}{2} + \frac{B}{20} \quad (3\text{-}38)$$

On the other hand, the constriction correction factor considers the increased constriction of reactant path due to reduced entrance area. The derivation of this correction factor is based on the definition of constriction factor by Petersen [25] and the details of the derivation are given in Appendix A. However, it is notable that a variable focal point of the constriction hyperbolas in Figure 3-12 is introduced as a fitting parameter called tunability factor b. The resulting constriction correction factor σ_{corr} can be expressed by:

$$\sigma_{corr} = \frac{6(1-\eta_0)z_0}{\eta_0^2\left(z_0 + \frac{z_0^3}{3(b^2-\eta_0^2)}\right)\tan^{-1}\left(\frac{2z_0}{1+\eta_0}\right)} \quad (3\text{-}39)$$

where η_0 is the axis intercept that is fixed at 0.7071, and z_0 the half-length of the hyperbola (see Figure 3-12). They are related to the covered angle ψ by:

$$z_0 = \sqrt{(b^2 - \eta_0^2)\left(\frac{2}{1+\cos\psi} - 1\right)} \tag{3-40}$$

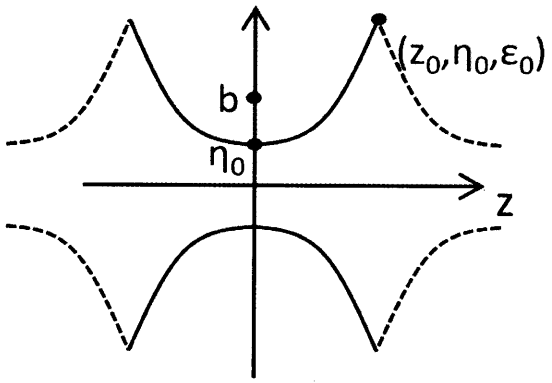

Figure 3-12 Model of pore with periodic pore constrictions ; b is the focal point of the hyperbola, η_0 the axis intercept and z_0 the half length of the hyperbola.

3.4. Slag Properties

Chemical compositions of coal slags vary significantly between mining regions and consequently, the properties of the slags also vary appreciably. A common measurement method of the slag composition is the use of X-ray fluorescence (XRF) to determine the mineral oxides that are present in the slag. These oxides are sometimes categorized into basic and acidic components and the acid to base ratio is used in the development of mathematical models.

Besides, slag properties also vary considerably with temperature. Therefore, mathematical models for slag properties are usually developed on the basis of these

independent variables: temperature and chemical composition. The following sections present selected properties that are used in the slag model that are relevant to the fluid flow and the heat transfer. The mathematical correlations described are developed using data of coal slags and appropriate metallurgical slags and magmas due to the dearth of physical property data of coal slags. This has the advantage that the models are applicable to a wide range of compositions.

Slag properties in this work are evaluated at the slag mean temperature (Assumption 6 in Section 3.3.1). Given the assumption of a cubic temperature profile across the slag layer (Assumption 5), the mean slag temperature is given as:

$$T_{slag} = \frac{5T_s}{8} + \frac{3T_{cv}}{8} - \frac{q_{in}\,\delta_l}{8k} \tag{3-41}$$

where δ_l is the molten slag thickness, T_s the slag surface temperature, T_{cv} the temperature at critical viscosity, q_{in} the heat flux to the slag surface and k the slag thermal conductivity.

3.4.1. Properties Relevant to Slag Flow

3.4.1.1. Density

Mills and Rhine [26] review several slag density prediction models and propose the use of a mathematical model in terms of the constituent mole fraction x_i, the constituent molecular weight M_i and the partial molar volume $\bar{V}_i$ with recommended values given in Table 3-1 to take slag structure into account:

$$\rho_s = \frac{\sum M_i x_i}{(1+0.0001\ (T_{slag}-1773))\sum \bar{V}_i x_i} \tag{3-42}$$

Table 3-1 Recommended values for partial molar volumes of slag constituents at 1773 K.

Constituents	$\bar{V}$ [10^{-6} m^3mol^{-1}]
CaO	20.7
MgO	16.1
Na2O	33.0
FeO	15.8
Fe_2O_3	38.4
MnO	15.6
TiO_2	24.0
P_2O_5	65.7
CaF_2	31.3
SiO_2	$19.55+7.966*x_{SiO_2}$
Al_2O_3	$28.31+32*x_{Al_2O_3}-31.45*x^2_{Al_2O_3}$

3.4.1.2. Surface Tension

All surface tension prediction models use the principle of additivity of the partial molar surface tension of the various slag constituents. Mills and Rhine [26] propose the use of the recommended values of partial molar surface tension, $\bar{\sigma}_i$, given in Table 3-2 for the prediction of slag surface tension according to the following equation:

$$\sigma_s=(\sum \bar{\sigma}_i x_i - 0.15\ (T_{slag}-1733))\ 10^{-3} \tag{3-43}$$

Table 3-2 Recommended values of partial molar surface tension of slag constituents at 1733 K.

Constituents	$\bar{\sigma}$ {m Nm^{-1}]
CaO	625.0
MgO	635.0
FeO	645.0
MnO	645.0
TiO_2	350.0
SiO_2	260.0
Al_2O_3	655.0
P_2O_5	$-5.2\ x_{Fe_2O_3}^{-1} - 3454 + 22178\ x_{Fe_2O_3}$
Fe_2O_3	$-3.7\ x_{Fe_2O_3}^{-1} - 2972 + 14312\ x_{Fe_2O_3}$
Na_2O	$0.8\ x_{Na_2O_3}^{-1} - 1388 - 6723\ x_{Na_2O_3}$
K_2O	$0.8\ x_{K_2O}^{-1} - 1388 - 6723\ x_{K_2O}$

3.4.1.3. Temperature of Critical Viscosity

The temperature of critical viscosity, T_{cv}, is defined as the temperature at which there is an abrupt transition between liquid and plastic flow, which is evidenced by a sudden change in viscosity for a small change in temperature or where the internal yield stress is first lost or developed in the slag [27]. The temperature of critical viscosity is dependent on the slag composition. The following are selected models of predicting this temperature (slag components are expressed in weight components):

Watt-Fereday (1963) [28]

$$T_{cv} = 3263 - 1470A + 360A^2 - 14.7B + 0.15B^2 \qquad (3\text{-}44)$$

Nowok et al. (1993) [29]

$$T_{cv} = 1473.15 - 230\ln\left(\frac{FeO + CaO + MgO + Na_2O + K_2O}{SiO_2 + Al_2O_3 + TiO_2 + Fe_2O_3}\right) \quad (3\text{-}45)$$

Patterson et al. (2001) [30]

$$T_{cv} = 3452 - 519.5A + 74.5A^2 - 67.8B + 0.86B^2 \quad (3\text{-}46)$$

Seggiani (1998) [10]

$$T_{cv} = 1385.44 + 74.1\left(\frac{Fe_2O_3 + CaO + MgO + Na_2O + K_2O}{SiO_2 + Al_2O_3 + TiO_2}\right) \quad (3\text{-}47)$$

where

$$A = \frac{SiO_2}{Al_2O_3}$$

$$B = Fe_2O_3 + CaO + MgO$$

3.4.1.4. Viscosity

Many models have been developed to predict the slag viscosity in the literature. These models all attempts to relate viscosity to temperature and the slag composition. Existing models are the result of an empirical fitting of data, and they only apply to Newtonian liquids, i.e. completely molten systems. They can be categorized as follows:

- Nomograms, charts and look-up tables
- Fitted equations that
    - relate viscosity to temperature (Arrhenius, Weymann, Vogel-Fulcher-Tammann equations)
    - relate viscosity to composition

No model outperforms all other models for all slag compositions considered in the study of Vargas et al. [31]. However, the Urbain (1981) and Kalmanovitch-Frank (1988) models are best suited for the prediction of the viscosity of coal slags [31]. Both models are given in the same Weymann form (slag components are expressed as mole fractions):

$$\mu_s = aT_{slag} \exp\left(\frac{1000b}{T_{slag}}\right) \tag{3-48}$$

with

$$x_m = FeO + CaO + MgO + Na_2O + K_2O + MnO + NiO + 2(TiO_2 + ZrO_2) + 3CaF_2;$$

$$x_a = Al_2O_3 + Fe_2O_3 + B_2O_3;$$

$$\omega = \frac{x_m}{x_m + x_a}$$

$$b_0 = 13.8 + 39.9355\omega - 44.049\omega^2;$$

$$b_1 = 30.481 - 117.1505\omega + 129.9978\omega^2;$$

$$b_2 = -40.9429 + 234.0486\omega - 300.04\omega^2;$$

$$b_3 = 60.7619 - 153.9276\omega + 211.1616\omega^2;$$

$$b = b_0 + b_1 SiO_2 + b_2 SiO_2^2 + b_3 SiO_2^3$$

Urbain (1981)

$$a = \exp(-0.2693b - 13.9751)$$

Kalmanovitch-Frank (1988)

$$a = \exp(-0.2812b - 14.1305)$$

where x_m and x_a are the sum of mole fractions of glass modifiers and amphoterics (grouped according to the oxygen content [31]).

3.4.1.5. Specific Heat Capacity

Mills and Rhine [32] proposed that the specific heat capacity of slag has a different characteristic in the glassy and the liquid phases. In the liquid phase, the specific heat capacity is independent of temperature and is determined with the principle of additivity of the partial molar specific heats of the various slag constituents:

$$c_p = (x_1 \bar{c}_{p_1} + x_2 \bar{c}_{p_2} + x_3 \bar{c}_{p_3} + ...) 10^3 \tag{3-49}$$

The recommended values of partial molar specific heat capacities for the liquid state are given in the final column of Table 3-3. On the other hand, the partial molar specific heats in the glassy state are dependent on the temperature and are given as:

$$\bar{c}_p = a + b\, T_{slag} - c\, T_{slag}^{-1} \tag{3-50}$$

where the parameters a, b, c are dependent on the slag constituents and are given in the center column of Table 3-3.

The transition from the glassy to the liquid state takes place at a temperature of approximately 800-1000 K and the apparent enthalpy of fusion is found to be approximately 230 J/g.

Table 3-3 Recommended values for partial molar specific heat of slags constituents.

Constituents	$\overline{c_p}$ (glass) [$JK^{-1}mol^{-1}$] $= a + b\,T_{slag} - c\,T_{slag}^{-1}$			$\overline{c_p}$ (liq) [$JK^{-1}mol^{-1}$]
	a	b	c	
SiO_2	55.98	15.40	14.48	87.0
CaO	48.82	4.52	6.52	80.8
Al_2O_3	115.00	11.80	35.15	146.4
MgO	42.60	7.45	6.19	90.4
K_2O	65.70	22.60	0.00	74.0
Na_2O	65.70	22.60	0.00	92.0
TiO_2	75.19	1.17	18.20	111.7
MnO	46.48	8.12	3.68	79.9
FeO	48.78	8.36	2.80	76.6
Fe_2O_3	98.28	77.80	14.85	191.2
Fe	12.72	31.71	-2.51	43.9
P_2O_5	182.50	46.40	45.44	242.7
CaF_2	59.83	30.45	-1.96	96.2
SO_3	70.20	97.74	0.00	175.7

3.4.1.6. Thermal Conductivity

There are two methods of predicting the thermal conductivity of coal slag [32]. The first involves separating the contributions of thermal ('phonon') conductivity, the radiation conductivity and the electronic conductivity. However, it is frequently more convenient in experimental measurements to determine the thermal diffusivity, α_{eff} , than the thermal conductivity, k. Thus, the second method of predicting the thermal conductivity is through the relation:

$$k = \alpha_{eff} C_p \rho_s \tag{3-51}$$

The value of α_{eff} is found to not vary appreciably with temperature and composition. A value of 4.5 x 10^{-7} m^2s^{-1} is adopted in Seggiani [10] and this value is used for all the computations in this thesis.

3.5. Conclusions

This chapter started off by introducing the inputs and outputs of the slag model and the role of the slag model in relation to a CFD framework. Then, the development of the slag model is described. The slag model includes a slag flow model that considers the heat and flow characteristics of the slag along the reactor wall and two submodels – particle capture and wall burning – that predicts the rate of depositing particles based on the slag and particle phases and Weber numbers, and the effective diffusivity of a particle trapped in a slag layer, respectively. Finally, the chapter describes some mathematical models used to predict the slag properties pertaining to slag flow such as the density, the surface tension, the viscosity and the temperature at critical viscosity, and thermal properties of the slag such as specific heat and thermal diffusivity.

Chapter 4 Model Application to Coal Combustor and Gasifier

4.1. Overview

This chapter puts the slag model that is described in Chapter 3 to the test. Initially, the reactor systems, to which the slag model is applied, are described. Section 4.2 is dedicated to the description and discussion of the model application to a pressurized oxy-coal combustor and Section 4.3 applies the slag model to a two-stage air blown entrained flow coal gasifier.

The description includes the type of coal that is used and the operating conditions of the system. The CFD framework as well as the submodels that have been used to simulate the reacting processes in the reactors is also explained in Section 4.2.1 and Section 4.3.1 for the combustion and gasification cases respectively. Next, the model inputs from the CFD used in the slag model are presented, followed by the results of the slag model computation in Section 4.2.2 and Section 4.3.2.

Section 4.4 discusses the sensitivity analyses of several important parameters. First, the results of varying the reactor inclination to discover the importance of particle momentum transfer to slag flow when compared to slag gravity is discussed, followed by the variation of the critical Weber number and a comparison with the case where all particles are trapped. The analysis of temperature of critical viscosity variations is also carried out.

Finally, Section 4.6 describes the implementation of the slag model in the CFD framework as User Defined Functions (UDFs). Concluding remarks complete the chapter in Section 4.7.

4.2. Pressurized Oxy-Coal Combustor

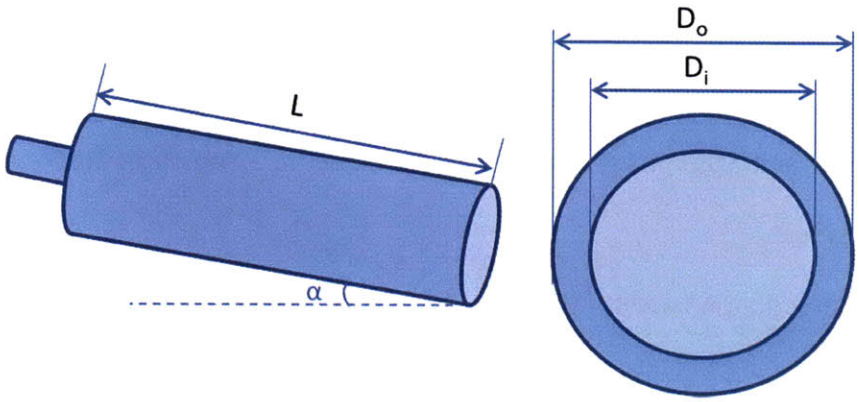

Figure 4-1 Geometry of the pressurized oxy-coal combustor.

Table 4-1 Operating conditions of the burner and atomizer.

	Component	Mass flow rate [kg/s]	Mole fraction
Burner stream (280°C, 4 bar)	O_2	0.26	0.222
	N_2	0.038	0.037
	CO_2	0.58	0.361
	H_2O	0.25	0.38
CWS (37°C, 15 bar)	coal	0.1	N/A
	water	0.054	
Atomization gas (265°C, 18 bar)	H_2O	0.01	1

Table 4-2 Properties of raw coal and ash.

Coal Proximate Analysis	
Moisture (%)	6.4
Ash (%)	7
Volatile matter (%)	33.1
Fixed carbon (%)	53.5

Coal Ultimate Analysis	
Carbon (%)	71.1
Hydrogen (%)	4.7
Moisture (%)	6.4
Ash (%)	7
Sulphur (%)	0.5
Nitrogen (%)	1.2
Oxygen (%)	9.086
Chlorine (%)	0.014
Fluorine (ppm)	34.6

Oxide wt% of ash	
SiO_2	44.35
TiO_2	1.56
Al_2O_3	30.88
CaO	3.82
MgO	3.14
Na_2O	0.76
K_2O	0.67
P_2O_5	1.027
Mn_3O_4	0.1
SO_3	0.85
Fe_2O_3	4.51

Properties	Range
T_{cv} (K)	1680
Viscosity (Pa s)	6.21 - 334.47
Density (kg/m^3)	2779.9 - 2887.9
Specific heat (kJ/kg K)	1.3825
Thermal conductivity (W/m K)	1.7294 - 1.7966

The slag model is tested under oxy-combustion conditions with inputs from a CFD simulation of an inclined pilot-scale slagging combustor operating at 4 bar. The ISOTHERM combustor, developed by ITEA S.P.A. and ENEL, consists of a partial swirl burner and a coal water slurry (CWS) atomizer. The combustor wall is made of refractory material and the external wall surface is cooled by water at a temperature of 343 K with an

assumed heat transfer coefficient of 9 W/m^2K. A thermal conductivity of 28.88891 W/m K is adopted for the refractory wall. The combustor geometry is given in Figure 4-1 and more details on the ISOTHERM pressurized oxy-coal combustion system can be found in Hong et al. [33]. The description of the combustion system is reported in [34,35] and the combustion system is patented by Itea [36-39].

The combustor is fed with three streams of oxidizers and reactants: the burner stream, the coal water slurry (CWS) and the atomization gas. The mass flow rates and their components are shown in Table 4-1. The coal water slurry is sprayed into the combustor with a Sauter mean diameter of 200 μm. The properties of the coal used in the combustor are given in Table 4-2.

4.2.1. Computational Fluid Dynamics Framework

FLUENT 12.0.16 was used in the CFD framework and the modeling uses a gas-discrete phase coupling: an Eulerian approach for the gas phase and a Lagrangian approach for the discrete phase. The Reynolds Average Navier Stokes (RANS) equations are used to model the flow field, the SIMPLE algorithm for pressure-velocity coupling and the k-ε model for the gaseous turbulent flow. For gaseous combustion reactions, the finite rate/eddy dissipation model was adopted, while for the discrete phase, the char devolatilization is calculated using the Chemical Percolation Devolatilization (CPD) Model and the char combustion with the fixed core/multiple surface reactions model. Radiation heat transfer is simulated by using the Discrete Ordinates (DO) radiation model where the

local absorption coefficient was calculated with the help of the Weighted Sum of Gray Gases (WSGG) model. More details on the CFD framework can be found in Chen and Ghoniem [40].

4.2.2. Simulation Results

4.2.2.1. Model Inputs

Figure 4-4 shows the CFD simulation outputs which are used as inputs to the slag model, with the exceptions of q_{loss} and $\dot{m}_d''$, which are model outputs [40]. The heat flux per unit area to the slag layer, q_{in}, which is a function of slag temperature, reactor temperature and flow characteristics within the combustor, is obtained from the CFD simulations as the sum of convective and radiation heat fluxes. The particle spray angle adopted in CFD simulations leads to the highest particle feed rate at about 0.5 L. The average particle temperature at that location is also lowest as shown in the Figure 4-4(c). The particles that collide with this portion of the wall come directly from the atomizer and their residence times are relatively small as shown by the particle tracks in Figure 4-2. While water has been completely evaporated, the particles are still devolatilizing resulting in the low particle temperatures and correspondingly, the largest particle diameter and density due to particle swelling (particle swell ratio is fixed at 1.4) as shown in Figure 4-4(c),(e) and (f). This is confirmed by the particle devolatilization and consumption rates in Figure 4-4(b) which are only present in the vicinity of the above mentioned region. The particles at the two extremes of the combustor wall are fully converted and this can be seen

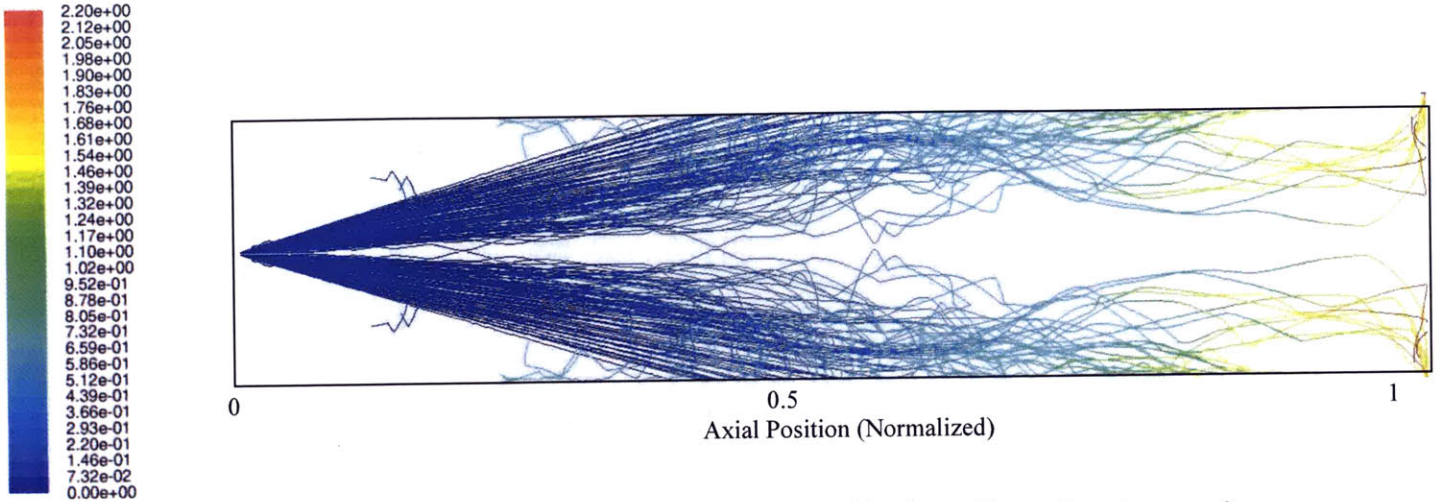

Figure 4-2 Particle tracks colored by the residence times in second.

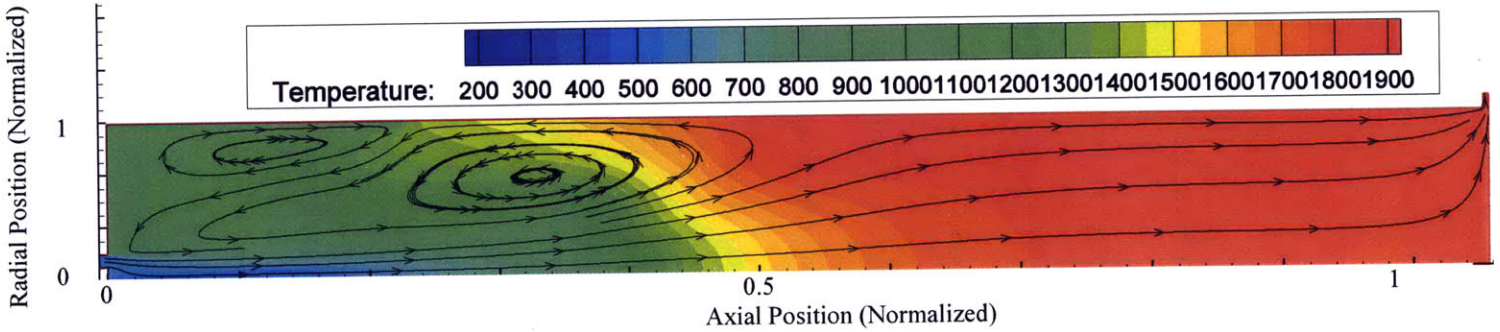

Figure 4-3 Temperature contour in K and streamlines of the fluid flow.

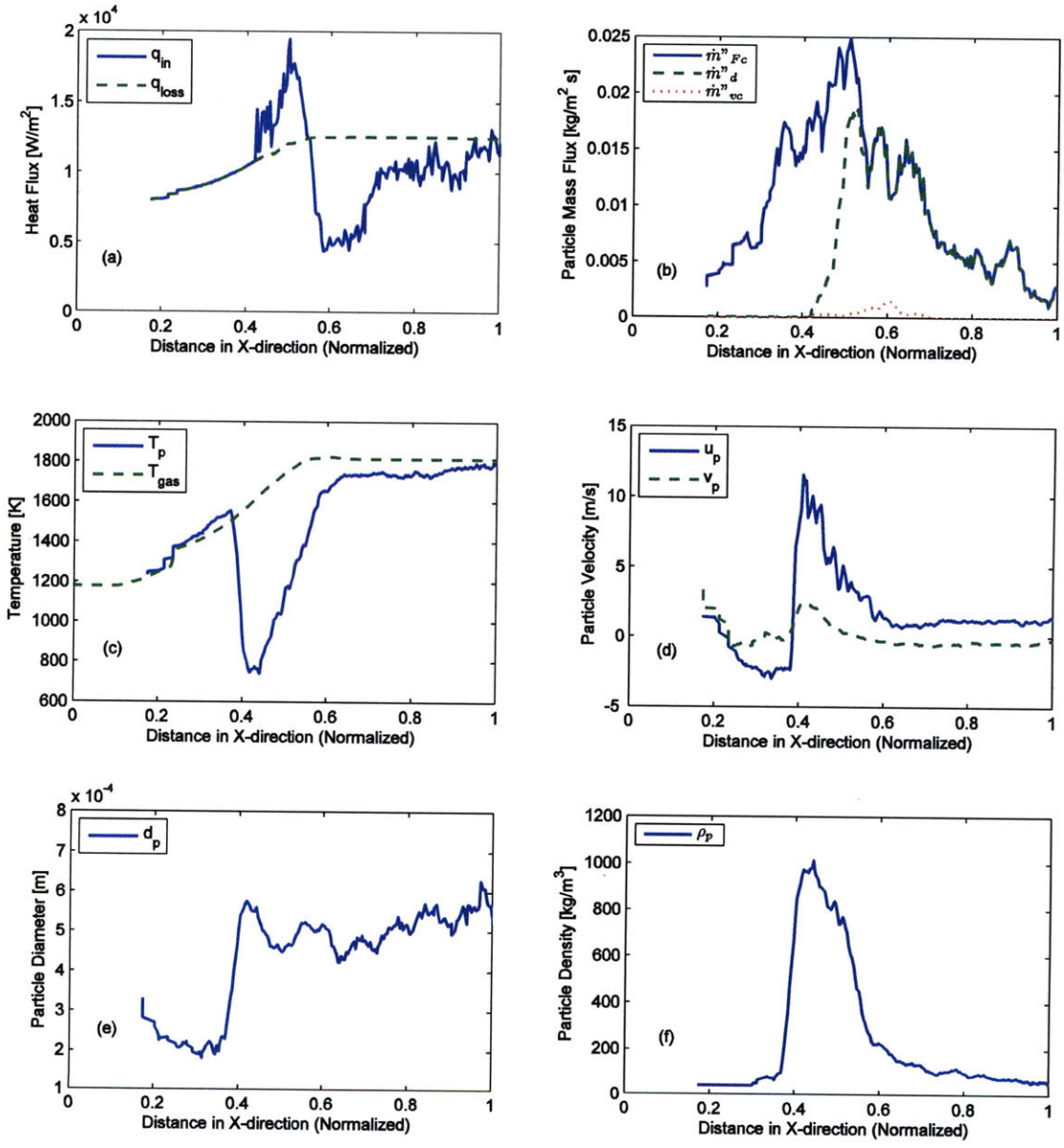

Figure 4-4 Pressurized Oxy-Combustor – CFD simulation outputs/ model inputs: (a) Heat flux to slag surface and heat loss to coolant; (b) Mass feed rate per unit area, mass deposition rate per unit area and particle volumetric consumption rate $\cdot \Delta x$; (c) Average particle temperature and gas temperature near the wall; (d) Average particle velocity in the direction of and normal to the slag flow; (e) Average particle diameter along the wall; (f) Average particle density along the wall.

both in the particle devolatilization and consumption rate plot (Figure 4-4(b)) and the plot of particle densities (Figure 4-4(f)) because ash particles are less dense compared to coal particles.

The velocity profiles (Figure 4-4(d)) depend on the flow configuration in the combustor as shown in Figure 4-3 and reverse flow is observed in the region between 0.2 L and 0.4 L from the combustor inlet. The recirculating flow also carries smaller particles with lower inertia to the top of the combustor resulting in smaller average particle diameters at close to the combustor inlet. The gas temperature near the wall, T_{gas}, is lower at the location because of mixing with fresh oxygen and flue gases while the half of the combustor that is closer to the combustor outlet is hotter due to combustion reactions.

4.2.2.2. Model Outputs

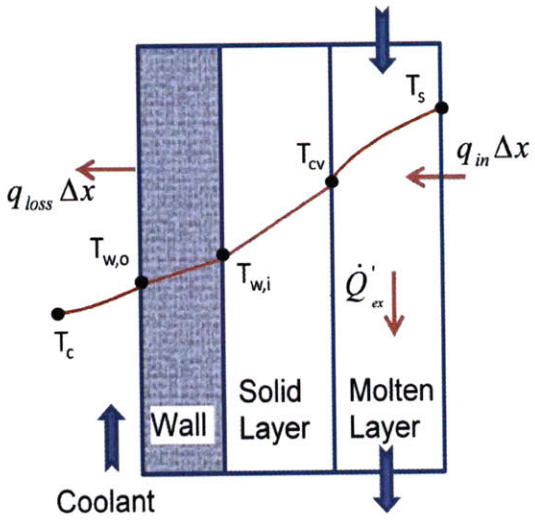

Figure 4-5 Temperature profiles and heat fluxes to and from the wall and slag layer.

The simulation results of the slag model presented in this section are based on steady-state outputs from the CFD. A two-way coupling with the CFD is not expected to drastically alter the trends observed here. Note that the heat of fusion in Equation (3-12) is neglected in this simulation due to the relatively small contribution when compared to the enthalpy of the trapped particles.

Flow and heat transfer characteristics of the slag layers are discussed in detail in this section. Slag mass flow rate and velocity apply only to the molten slag layer whereas the slag viscosity is evaluated at the mean temperature of the molten slag layer if it exists. Otherwise, it is evaluated at the surface temperature. Surface temperature T_s, outer and inner wall temperatures T_{wo} and T_{wi} refer to temperatures as depicted in Figure 4-5. Likewise, heat loss and heat in correspond to q_{loss} and q_{in}, as shown in the same figure.

Figure 4-6(a) shows no slag layer built-up up to approximately 0.4 L from the combustor top. This is because of the low temperatures of the walls near the combustor top as can be seen in the Figure 4-6(b). In general, the slag surface temperature profile follows closely the trend of the gas temperatures near the wall as shown in Figure 4-4(c). The inner and outer wall temperatures are correspondingly lower than the slag surface temperature profile because of the finite conductivity through the slag layer and the combustor wall.

No solid slag layer (see Figure 4-6(a)) is built-up on the combustor wall because of the high temperatures that is common of oxy-combustion environments. The inner wall temperature T_{wi} never dips below the temperature of the critical viscosity T_{cv} resulting in no solid slag layer. This is consistent with the definition of solid and molten transition of coal slag at this temperature.

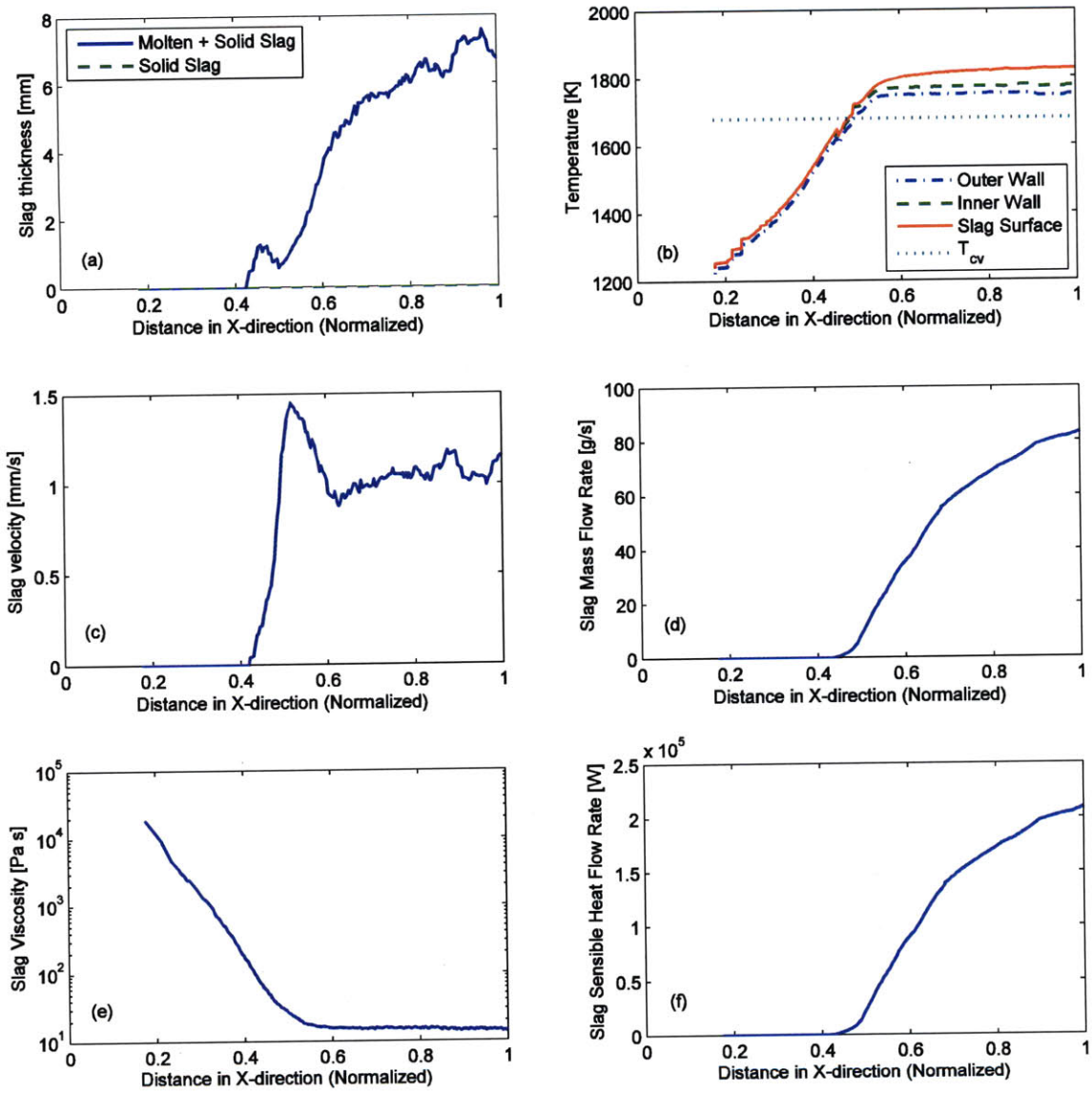

Figure 4-6 Pressurized Oxy-Combustor – Model outputs; (a) Total slag thickness and solid slag thickness; (b) Slag surface, inner and outer wall temperatures and temperature at the critical viscosity; (c) Slag velocity; (d) Slag mass flow rate; (e) Slag viscosity (ordinate in logarithmic scale); (f) Heat flux to slag surface and heat loss to coolant.

The slag mass flow rate observed in Figure 4-6(d) increases steadily down the combustor wall as more and more particles are captured (see $\dot{m}_d''$ in Figure 4-4(b)). On the other hand, the slag velocity increases with increasing particle momentum transfer (see Figure 4-6(c)). The peak in the velocity curve is because of the high momentum of the particles that are captured at that location. The momentum of captured particles is dependent on the velocity of those particles in the direction of slag flow, u_p, and Figure 4-4(d) shows a peak in u_p at that location, which once again explains the slag velocity peak. This also accounts for the slight dip in molten slag thickness in Figure 4-6(a) approximately 0.5 L down the reactor.

The heat loss q_{loss} profile (Figure 4-6(f)) is similar to that of the outer wall temperature T_{wo} (Figure 4-6(b)). Since these variables can be measured externally, they are good candidates for the overall model validation. Similarly, the slag mass flow rate and the slag viscosity at the molten ash port can be used for model verification.

These results have been found to be similar to that of Wang et al. for a pilot-scale slagging combustor. Although the slag capture submodel used is probabilistic in nature, the results agree that slag only begins to build up a little distance from the combustor inlet. In both cases, there is no solid slag layer built. A velocity peak and a slight dip in the molten slag thickness have also been observed. However, the model in this work is capable of also predicting temperature profiles and heat fluxes to the coolant, besides providing a deterministic criterion for the discrete phase in CFD simulations.

4.3. MHI Entrained Flow Coal Gasifier

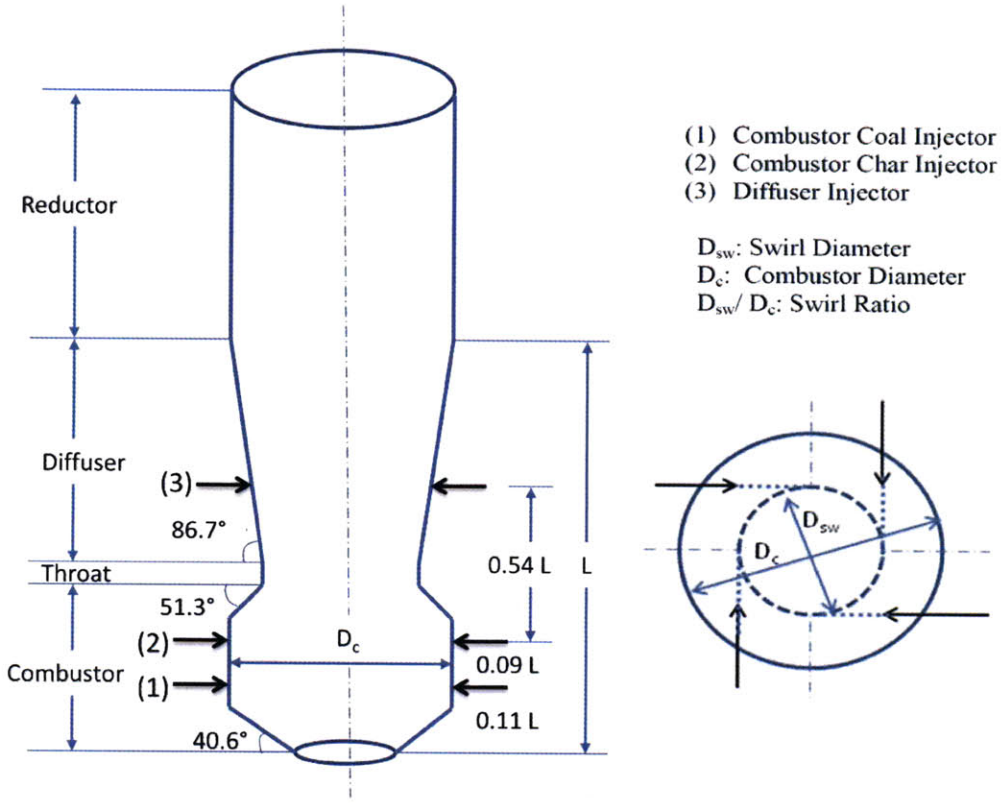

Figure 4-7 Gasifier geometry with swirl injector configurations: (1), (2) and (3) indicate the locations of the coal injectors.

The slag model is also tested under gasification conditions with inputs from a CFD simulation of a 200 td^{-1} pilot-scale slagging gasifier operating at 2.7 MPa. The geometry of the Mitsubishi Heavy Industries (MHI) gasifier is given in Figure 4-7. The MHI gasifier is an up-flow, dry-fed, air-blown, radially / tangentially-fired, two-stage gasifier. The first stage is fed with coal, recycled char and air (Burners 1 and 2), while the second stage is fed with coal and air (Burner 3). The mass flow rates of the individual burners are shown in

Table 4-3 Operating conditions of the gasifier burners [41].

	Burner	Mass flow rate [kg/s]
Particle loading (300 K)	(1)	0.472
	(2)	1.112
	(3)	1.832
Gas flow rate (Air at 450 K)	(1)	4.708
	(2)	4.708
	(3)	1.832

Table 4-4 Properties of raw coal and ash [41,42].

Coal Proximate Analysis	
Moisture (%)	5.3
Ash (%)	12.1
Volatile matter (%)	46.7
Fixed carbon (%)	35.8

Coal Ultimate Analysis	
Carbon (%)	77.6
Hydrogen (%)	6.5
Nitrogen (%)	1.13
Oxygen (%)	13.9
Sulphur (%)	0.22

Oxide wt% of ash	
SiO_2	46.58
TiO_2	2.02
Al_2O_3	24.91
CaO	9.91
MgO	0.89
Na_2O	0.89
K_2O	1.05
Fe_2O_3	6.58

Properties	Range
T_{cv} (K)	1540
Viscosity (Pa s)	16.09 - 7.92 x 10^5
Density (kg/m^3)	2809.7 - 3017.4
Specific heat (kJ/kg K)	1.3825
Thermal conductivity (W/m K)	1.748 - 1.877

Table 4-3 and the properties of the coal used in the gasifier are given in Table 4-4. The reductor wall is made of refractory material with a thermal conductivity of 28.9 W/m K and the external wall surface is cooled by water at a temperature of 343 K with an assumed heat transfer coefficient of 9 W/m^2K. More details on the MHI gasification system can be found in Kumar et al. [41].

The objective of this section is to examine the performance of the slag model under gasification conditions. For that reason, the discussion below only focuses on the diffuser and combustor sections of the gasifier (Figure 4-7). The reductor section is not considered because of the low temperatures in this section that inhibits the slagging phenomenon. In the simulations that will be described in Section 4.3.2, the diffuser section also turns out to be the most interesting section because of the occurrence of an important phenomenon called fouling that typically do not affect combustors and hence, was not discussed in the previous sections.

4.3.1. Computational Fluid Dynamics Framework

The CFD framework is similar to the oxy-combustion case. FLUENT is also used and the same models have been employed for modeling the flow field, the pressure-velocity coupling, gaseous combustion reactions, the char devolatilization and the radiation heat transfer. The only difference in the choice of models in the k-ω model for the gaseous turbulent flow, that is more suitable for the strongly swirling flows in the gasifier. More details on the CFD framework can be found in Kumar et al. [41].

4.3.2. Simulation Results

4.3.2.1. Model Inputs

The simulation results shown in this section are plotted as a function of distance in the direction of flow of coal/char particles and reactants (normalized by the total length of diffuser, throat and combustor). Hence, it is in the opposite direction to the slag flow. The vertical magenta lines refer to the location at which there is a change of gasifier inclination as shown in Figure 4-7. The section until the third vertical line is the combustor section, followed by a small throat section and the final section is the diffuser region. For the upper combustor section (between vertical lines 2 and 3), it is assumed that the dripping of the molten slag is prevented by the swirling gases.

The CFD simulation outputs shown in Figure 4-8 are used as inputs to the slag model [41]. q_{loss} and $\dot{m}''_d$, which are model outputs, are also depicted in Figure 4-8(a) and Figure 4-8(b) for the sake of comparison and will be explained in detail in the next section. The heat flux per unit area to the slag layer, q_{in}, which is obtained from the CFD as the sum of convective and radiation heat fluxes is observed to be high and fluctuating in the combustor, the throat and the lower part of the diffuser and decreases to a rather uniform profile from about 0.5 L onwards. This is a result of the combustion reactions at those locations that decrease in intensity after a distance of 0.5 L, as seen in Figure 4-9.

The particle feed rate $\dot{m}''_f$ in Figure 4-8(b) appear to fluctuate with an apparent periodicity. This is possibly because of the spiraling of the particle path lines as shown in Figure 4-10 that result from the injector configuration (Figure 4-7). Figure 4-9 also shows

that there are almost no combustion or gasification processes near the gasifier wall which is consistent with the particle volumetric consumption rate $\dot{m}'''_{vc}$ shown in Figure 4-8(b).

Figure 4-8(c) shows little variability in the temperature of particles that impact the gasifier wall. They remain at the high temperature attained during the combustion process in the combustor and stay fairly close to the gas temperature near the wall (c.f. Figure 4-11). The dip in the gas temperature in the combustor section is a consequence of air introduction by burner 1 and 2 whereas the dip at approximately 0.75 L corresponds to the location where air is introduced by burner (3).

Overall, the particles have a fairly uniform axial velocity at the lower diffuser section as observed in Figure 4-8(d) and some recirculation can be seen in the combustor which is a consequence of its geometry. However, the radial velocity profile has a drop at about 0.75 L. This can be explained with the location of the drop coinciding with the location of the injectors in the diffuser (Burner (3) in Figure 4-7). The radial introduction of air reduces the radial velocity of the particles as they pass through that region.

Figure 4-8(e) and Figure 4-8(f) show the diameter and the density of the particles that reach the gasifier wall respectively. In the combustor, the particles that impact the wall are completely converted because of the oxidizing environment which results in the low particle densities (pure ash density). On the other hand, only small particles are recirculated back to the bottom of the gasifier (< 0.05 L), but the particles that impact the wall between 0.05 L and 0.2 L are observed to be slightly larger than those between 0.2 L and 0.3 L. This difference is a result of the injection of coal, which swells during devolatilization, at approximately 0.1 L and the injection of char, which no longer swells, at 0.2 L.

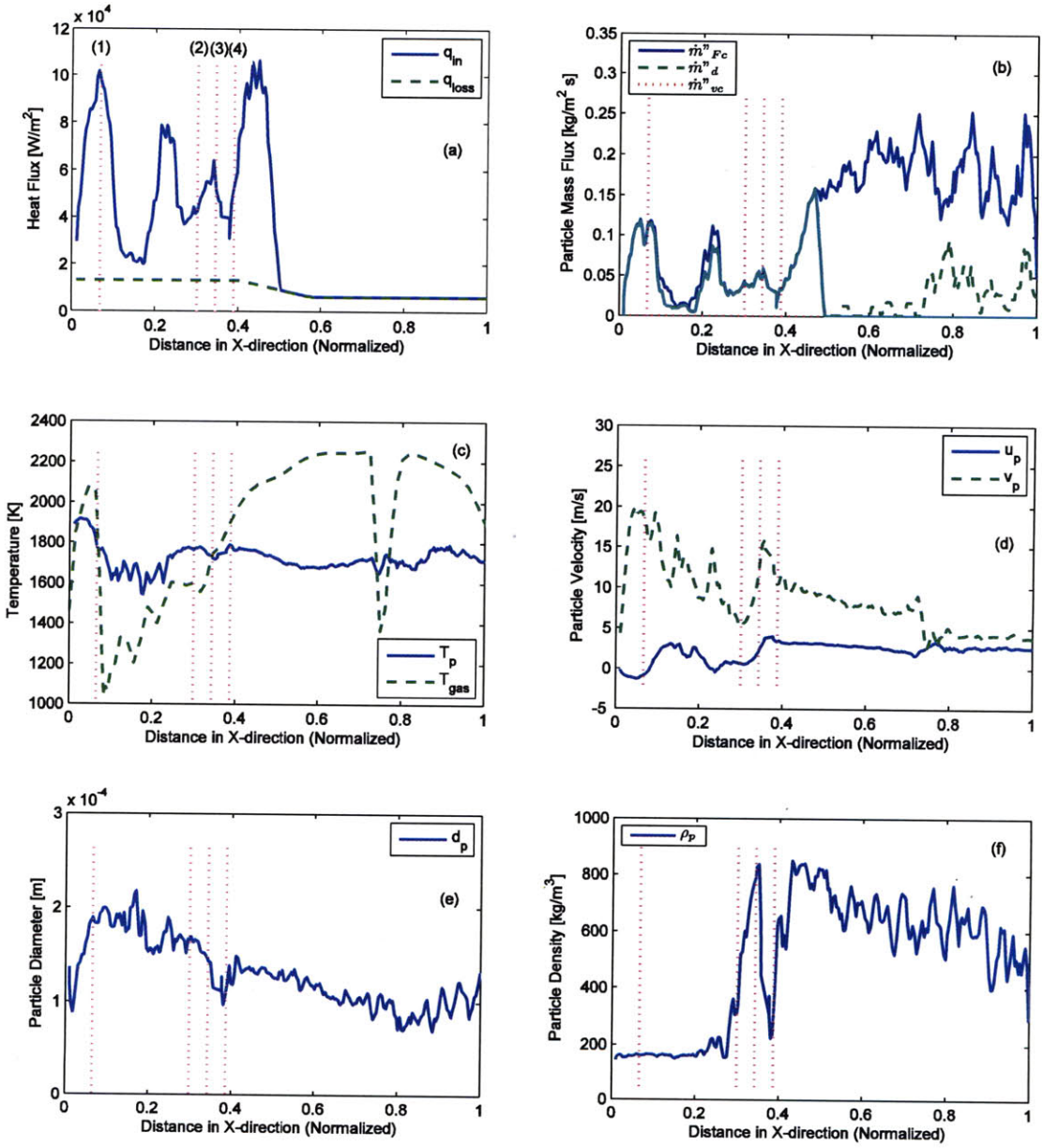

Figure 4-8 Two-stage Air Blown Gasifier – CFD simulation outputs/ model inputs: (a) Heat flux to slag surface and heat loss to coolant; (b) Mass feed rate per unit area, mass deposition rate per unit area and particle volumetric consumption rate (cyan: mass deposition that forms molten slag); (c) Particle temperature and gas temperature near the wall; (d) Particle velocity in the direction of and normal to the slag flow; (e) Particle diameter; (f) Particle density.

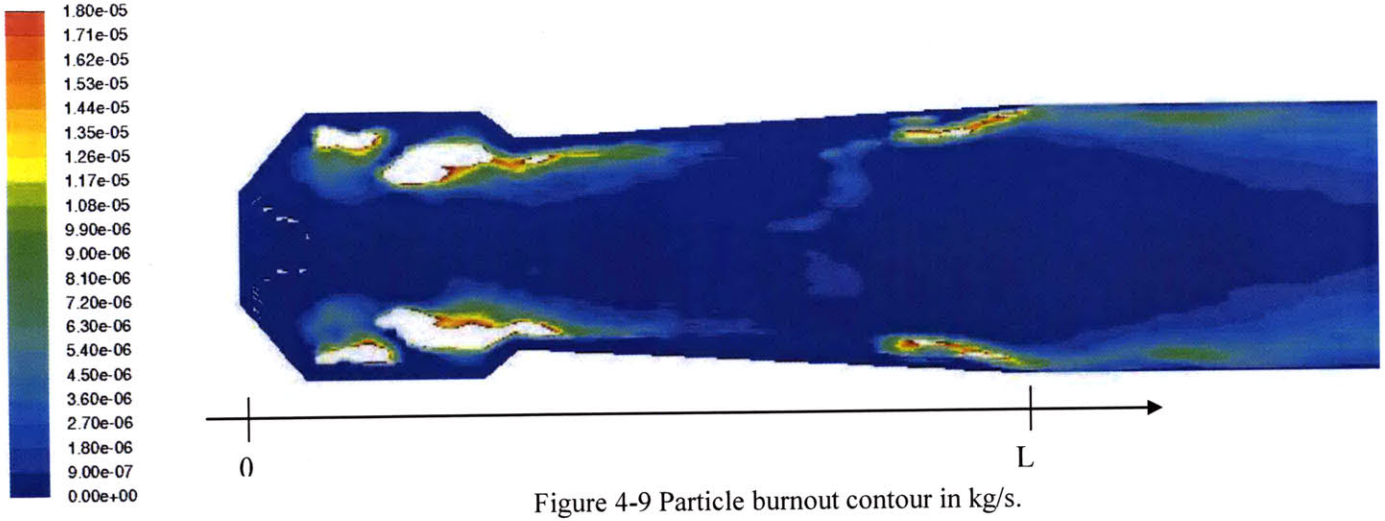

Figure 4-9 Particle burnout contour in kg/s.

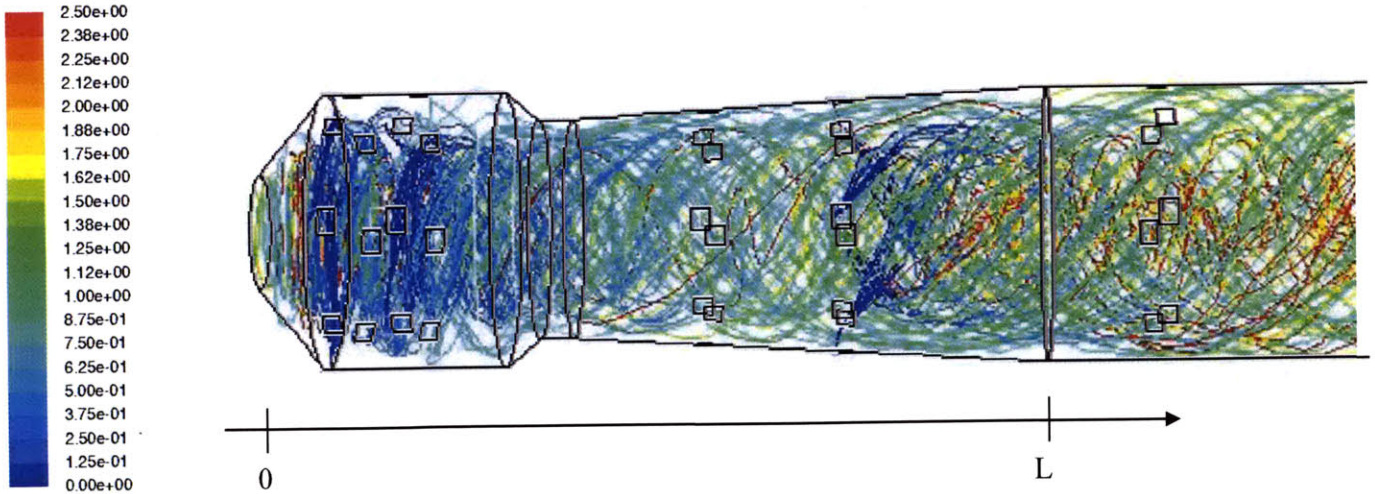

Figure 4-10 Particle tracks colored by the residence times in second.

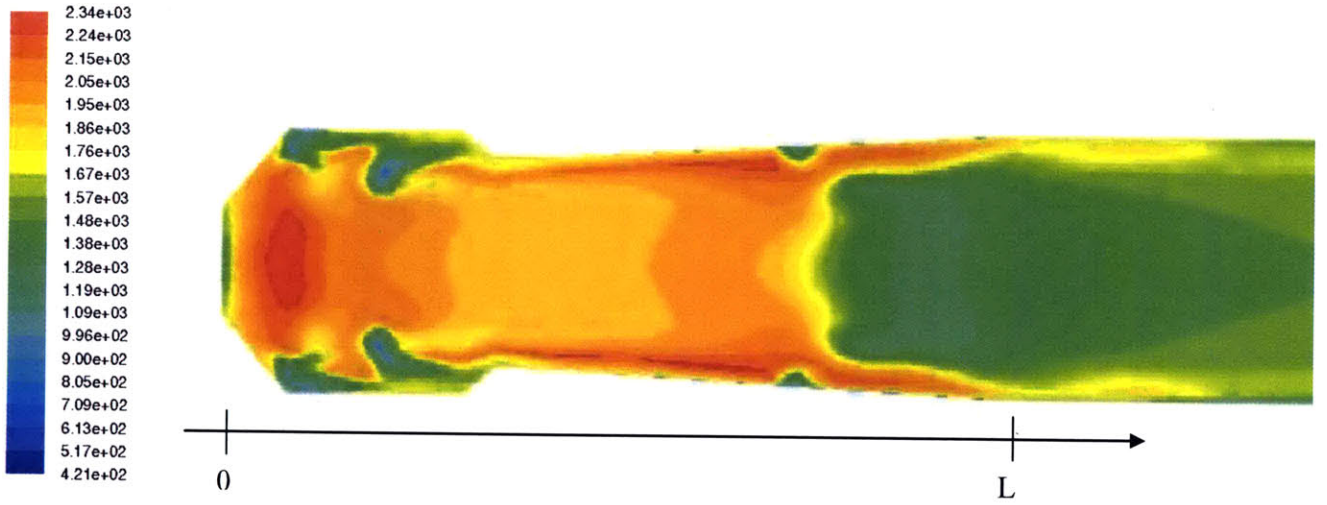

Figure 4-11 Temperature contour in K.

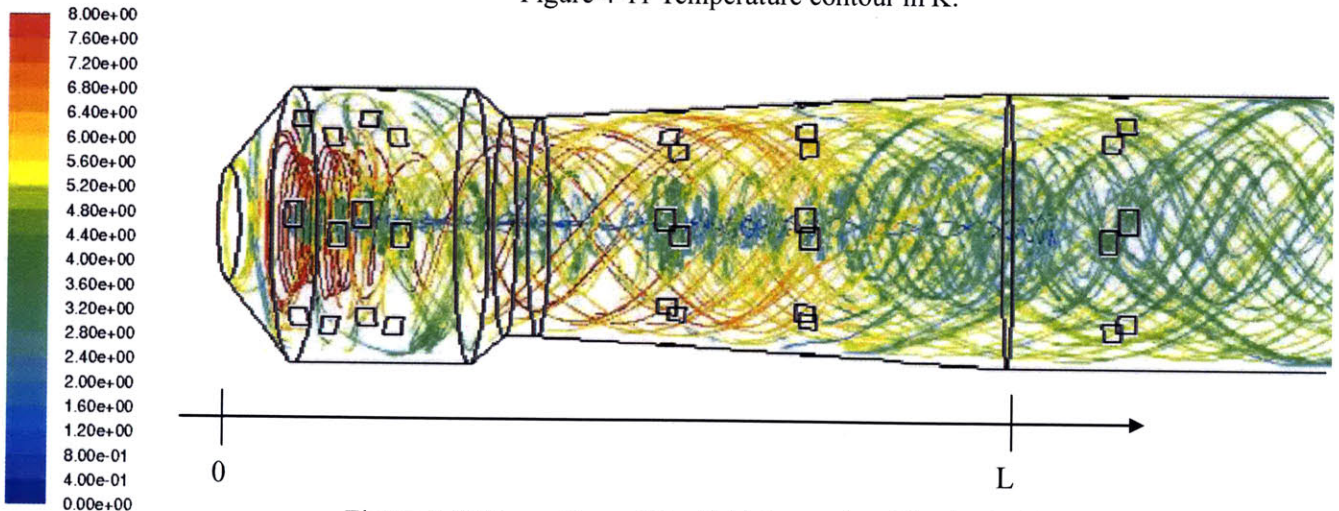

Figure 4-12 Streamlines of the fluid flow colored by the fluid velocity in m/s.

In general, there is a spread of particle diameters that are injected and a range of particle densities due to their different conversion extents. However, a trend of decreasing particle diameter and decreasing particle density with increasing distance is observed in the diffuser section. In other words, as particles flow from the gasifier bottom towards the top, smaller and lighter particles are more likely to reach the gasifier wall than bigger and denser ones. The reason for this is closely related to the Stokes number of particles which is proportional to the particle density and the square of the particle diameter [43]. As the swirl intensity of the gases in the gasifier decreases as they move up the gasifier (see Figure 4-12), particles with larger Stokes number are less likely to reach the gasifier wall, that is particles that are larger and denser impact the wall at a lower probability than smaller and lighter ones as seen in the figures.

4.3.2.2. Model Outputs

The model outputs described in this section – surface temperature T_s, outer and inner wall temperatures T_{wo} and T_{wi}, heat loss q_{loss} and heat flux to slag surface q_{in} – are as defined in Figure 4-5. As in the combustion case, the simulation results of the slag model presented in this section are based on steady-state outputs from the CFD without two-way coupling. They are shown in Figure 4-13 for only the diffuser, the throat and the combustor sections. Note that the slag flows in the opposite direction to fluid flow. Therefore, the slag flow in the direction of decreasing distance (towards the left in figures). Once again, the vertical magenta lines corresponds to the locations of gasifier inclination change as shown

in Figure 4-7. The section within the first three vertical lines is the combustor and the following two sections are the throat and the diffuser.

No slag is formed up until a distance of 0.5 L because of the low assumed wall temperature. This seems to contradict the mass deposition rate per unit area that is shown in Figure 4-8(b) because particles are deposited at distances that are larger than 0.5 L. These particles are trapped because they fall into the category of solid wall and liquid particle with Weber numbers that are lesser than the critical Weber number. However, due to the low wall temperature, these trapped particles cannot flow on the wall to form a molten slag layer. This phenomenon is known among reactor experts as fouling, which is the accumulation of solid particles on the gasifier wall that generally degrades the heat transfer characteristics of a gasifier. This occurrence is more common in gasifiers than in combustors. Thus, it was not observed in the combustion case in Section 4.2.2.2.

Only the cyan segment of the mass deposition rate line forms the molten slag shown from 0.5 L onwards in Figure 4-13(a). The condition used in this simulation to distinguish between molten slag and fouling particle is the proximity to a body of molten slag that is capable of flowing along the gasifier wall. This is reasonable given that the slag flow velocity is typically low and unless these liquid particles are within "flowing distance" to a wall region with temperature that is higher than the temperature of critical viscosity (which corresponds to a slag viscosity of less than approximately 1000 Pa s in Figure 4-13(e)), they will resolidify because of wall cooling.

Figure 4-13(a) also shows no solid slag layer built-up. This is expected given the monotonic increase in slag surface temperature (see Figure 4-13(b)). Solid layer typically

exist when the slag surface temperature is reasonably uniform or slightly decreasing, and is barely above the temperature of critical viscosity of the ash. In those cases, because of the finite thermal conductivity of the molten slag layer, the inner wall temperature will be below the temperature of critical viscosity which enables resolidification.

Unlike the combustion case, there is no particular region of the gasifier wall in the diffuser section that has a higher concentration of high kinetic energy particles as evidenced by the rather uniform radial velocities of the impacting particles (see Figure 4-8(d)). Therefore, Figure 4-13(c) show an almost monotonically increasing the slag velocity in the diffuser, with a slight decrease at the combustor end because of a slight decrease in particle deposition. In the combustor and throat sections, there are variations in the slag velocity and the molten slag thickness because of the varying gasifier wall inclination and the varying velocities of the trapped particles. On average, the slag velocity is higher and correspondingly, the molten slag layer is thinner in the sections where the wall is vertical (between vertical lines 1 and 2; and 3 and 4).

On the other hand, the monotonic increase in the slag mass flow rate in Figure 4-13(d) is a consequence of the accumulation of trapped particles since trapped particles are assumed to be either incorporated in the slag layer or floating on the slag surface without the possibility of being re-entrained by the fluid flow. The locations of the mass deposition rate peaks in Figure 4-8(b) correspond to the steeper increases of mass flow rate in Figure 4-13(d).

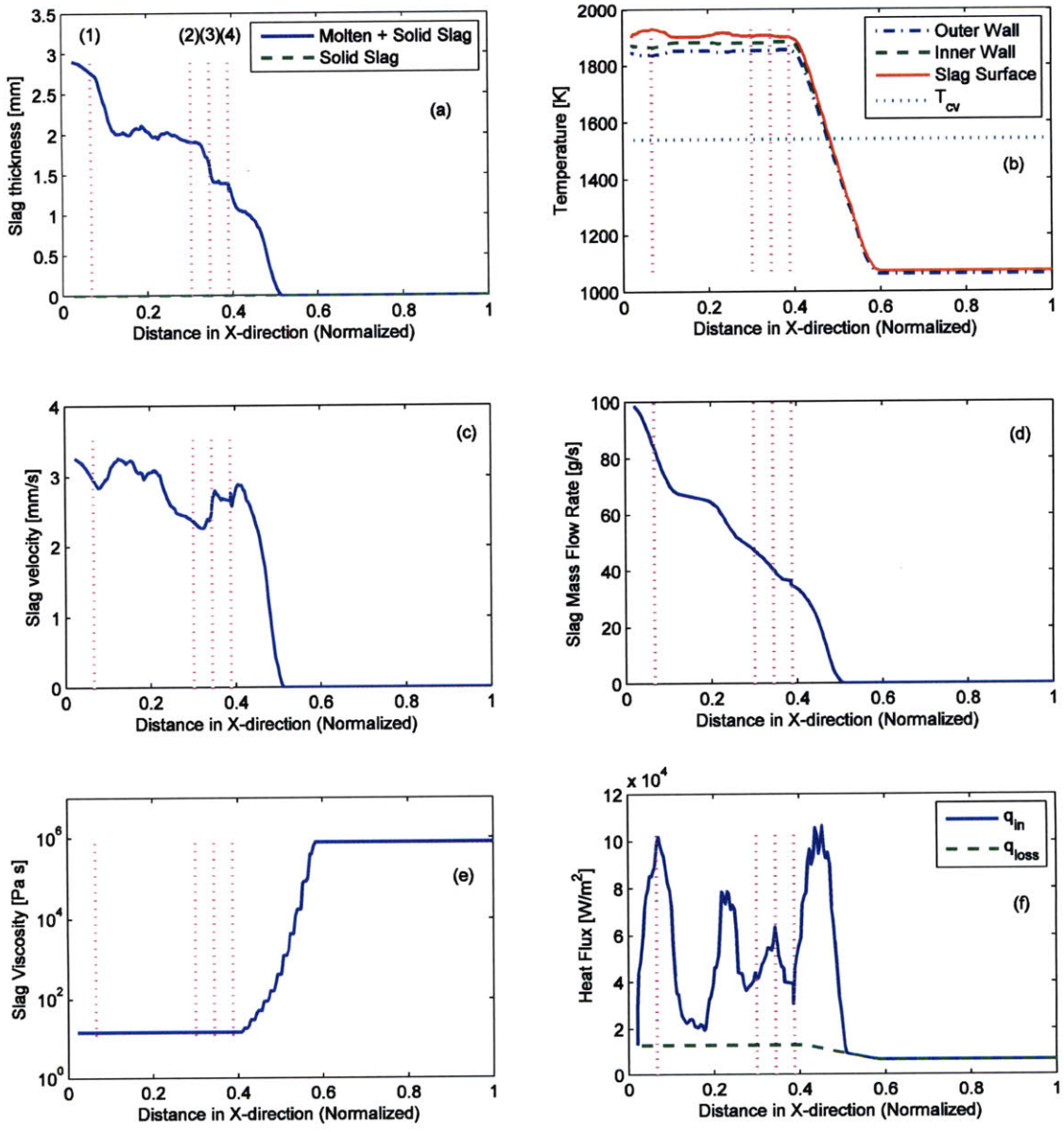

Figure 4-13 Two-stage Air Blown Gasifier − Model outputs; (a) Total slag thickness and solid slag thickness; (b) Slag surface, inner and outer wall temperatures and temperature at the critical viscosity; (c) Slag velocity; (d) Slag mass flow rate; (e) Slag viscosity (ordinate in logarithmic scale); (f) Heat flux to slag surface and heat loss to coolant.

The heat loss q_{loss} profile shown in Figure 4-13(f) corresponds to the trend of the outer wall temperature T_{wo} (Figure 4-13(b)) as in the combustion case. Similarly, these variables as well as the slag mass flow rate and the slag viscosity at the molten ash port are suitable for the overall model validation because of their accessibility from outside the gasifier.

These results are understandably different when compared to the results presented in Bockelie et. al [44] that compare the slag models developed by Benyon [9], Bockelie et. al [11] and Seggiani [10] when applied to a single stage gasifier. The temperatures in the single stage gasifier are always above the temperature of critical viscosity and remain rather uniform along the gasifier wall which favors the formation of a solid slag layer as discussed in Section 4.3.2.2. Benyon [9] has also applied his model to a two-stage gasifier. Similar to the slag model in this thesis, only the gasifier section near the combustor section has slagging characteristic. However, a direct comparison for these two slag model results is not possible because Benyon [9] has only presented his results for a small segment of the combustor section of the gasifier. From the small segment that has been shown, it can be inferred that only a solid slag layer exists at certain wall locations even though their wall temperatures are not below the temperature of critical viscosity. This is presumably a consequence of not having a particle capture submodel and assuming that all impacting particles are trapped. In conclusion, a particle capture submodel is an integral part of a slag model and deserves more attention.

4.4. Sensitivity Analysis

Preliminary study of the slag model suggests that the following parameters need more attention. Table 4-5 shows the variables with which we conduct sensitivity analyses. By varying the combustor inclination, we are able to investigate the importance of particle momentum transfer to the building up and flow of the slag layer. On the other hand, the study of the influence of the critical Weber number shows the importance of the choice of a particle capture model while the study of the temperature of critical viscosity demonstrated the importance of the slag properties prediction and the effect of changing the feedstock. This sensitivity study is performed using the pressurized oxy-coal combustion case.

Table 4-5 Sensitivity analysis parameters

Variables	Min.	Max.
Combustor inclination	1.5°	90°
Critical Weber number	0.1	5
Temperature of critical viscosity	1580 K	1785 K

4.4.1. Particle Momentum vs. Gravity

To study the importance of particle momentum contributions to the slag flow, simulations with various combustor inclinations were performed and the results are presented in Figure 4-14 where the relative contribution of particle momentum and gravity to slag flow is shown. Figure 4-14(a(i)) through (c(i)) show the comparison of forces that

drives the slag flow. The definition of these driving forces is given in Section 3.3.1.2. The momentum contribution, M_p and the gravitational contribution, G_s are given Equation (3-12) and Equation (3-13) respectively. Note that the results shown in the figures are normalized by the maximum value of the slag momentum contribution, M_p. A peak in particle momentum contribution is observed at approximately 0.4 L down the combustor wall, consistent with the high velocity of the particles that hit that portion of the combustor wall, as shown in Figure 4-4(d).

Figure 4-14(a(ii)) through (c(ii)) show the contribution of particle momentum to slag thicknesses. Particle momentum contribution is important for all combustor inclinations. Nonetheless, the gravity contribution is not negligible as Figure 4-14(a(iii)) through (c(iii)) show an increase in the slag velocity with increasing combustor inclination which accounts for the decreasing molten slag thickness. The temperature profiles in Figure 4-14(a(iv)) through (c(iv)) show similar trends. However, the temperature drop across the slag layer increases with increasing slag thickness because of the finite thermal conductivity of the slag. It is also notable that no solid slag layer is observed in these cases because of the high temperatures in the combustor.

Figure 4-14(d(i)) through (d(iv)) show the case without particle momentum transfer for a combustor inclination of 1.5°. Because of the lower average slag velocity along the combustor wall, the total slag thickness is thicker and consequently, the temperature difference between the slag surface and the inner wall is larger. Similar to the cases with momentum transfer, no solid slag layer is observed as shown in Figure 4-14(d(iv)).

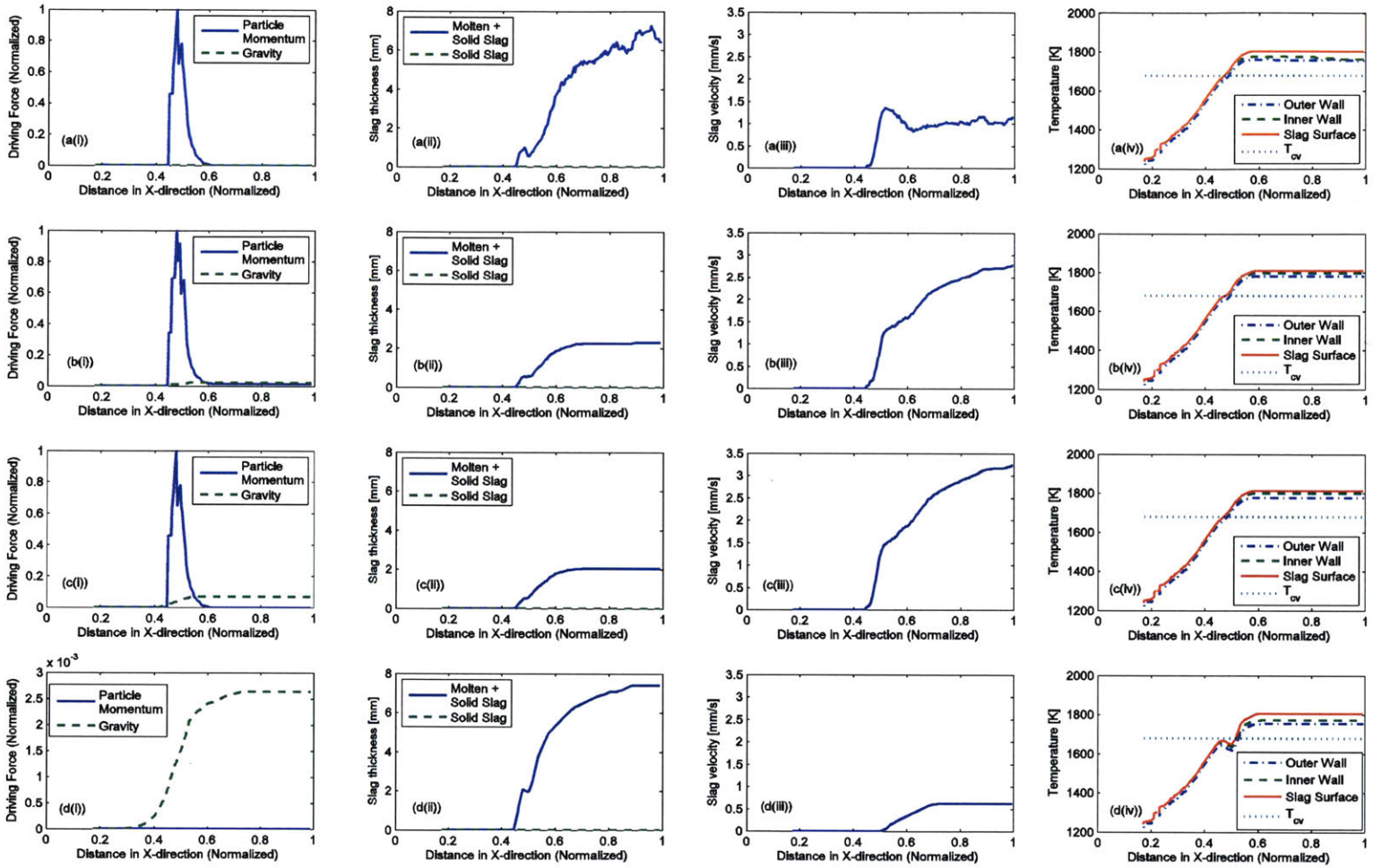

Figure 4-14 Influence of particle momentum transfer for different combustor inclinations; (a) $\alpha = 1.5°$ with momentum transfer; (b) $\alpha = 45°$ with momentum transfer; (c) $\alpha = 90°$ with momentum transfer; (d) $\alpha = 1.5°$ without momentum transfer.

4.4.2. Critical Weber Number

We next study the influence of the critical Weber number We_{cr} on the slag model. Figure 4-15(a(i)) through (c(i)) show the change in mass deposition rate per unit area $\dot{m}_d''$ for three different critical Weber numbers: 0.1, 1 and 5. The simulation demonstrates an increase in mass deposition with increasing critical Weber number. A larger We_{cr} denotes a higher tendency for capture. The figures illustrate that no particles are captured in the top portion of the combustor (up to approximately 0.45 L).

When more particles are deposited, it should follow that the slag layer is thicker. However, the particle momentum transfer also plays a role in increasing the slag velocity (Figure 4-15(a(iii)) through (c(iii)). As a result, the difference in molten slag layer thickness (Figure 4-15(a(ii)) through (c(ii))) is observed to be only approximately 0.3 mm, with the exception of the vicinity of 0.5 L. Here, the molten slag layer can differ up to 1.2 mm. On the other hand, the temperature profiles for the slag surface, the inner and the outer walls show a difference of up to approximately 20 K (Figure 4-15(a(iv)) through (c(iv))). This shows the importance of the critical Weber number. The difference in the slag surface temperature results in a different thermal boundary condition of the combustor wall and this, in turn, influences the CFD computations.

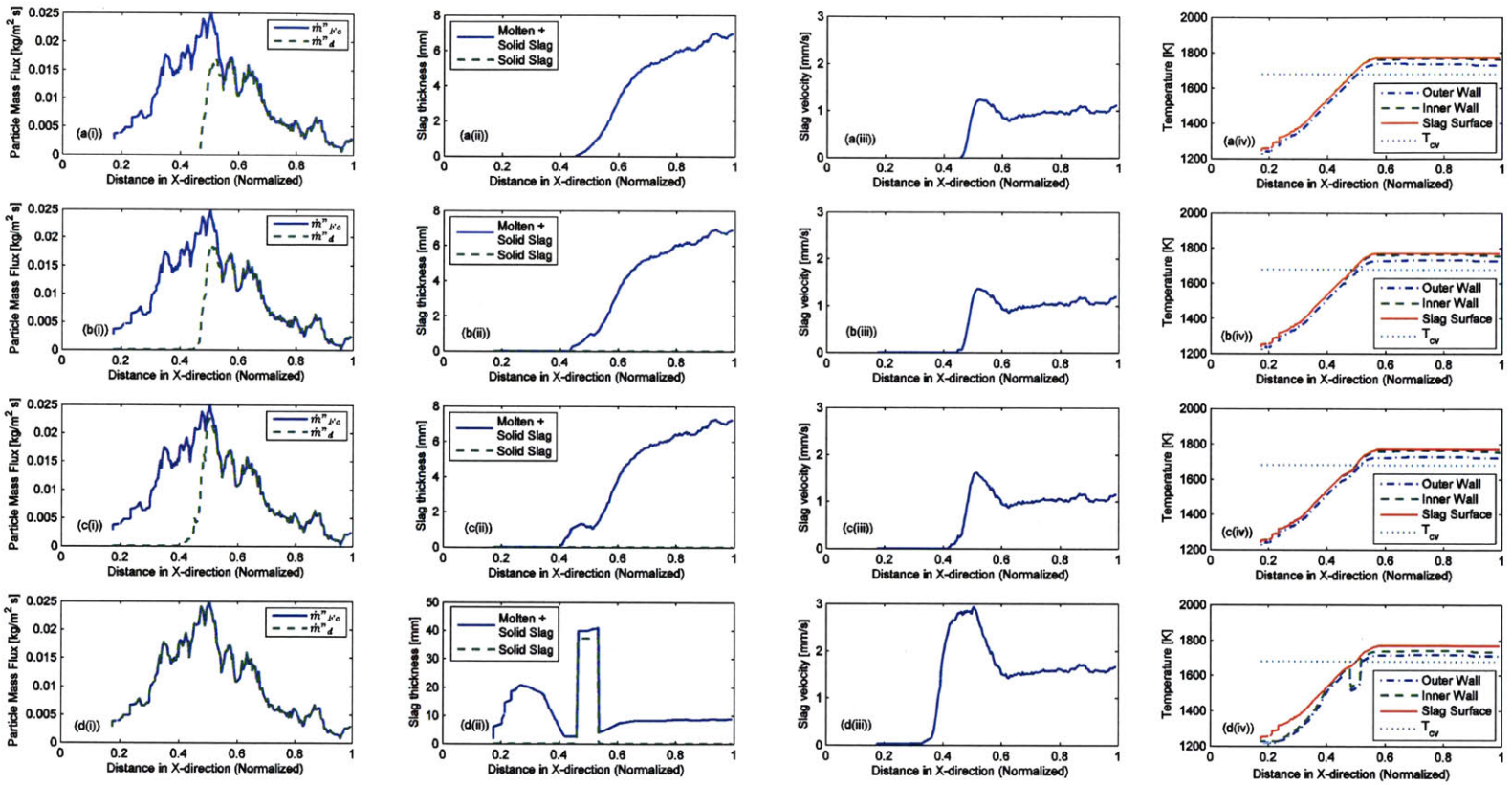

Figure 4-15 Influence of critical Weber number; (a) We_{cr} = 0.1; (b) We_{cr} = 1; (c) We_{cr} = 5; (d) All particles are assumed to be trapped.

Figure 4-15(d(i)) through (d(iv)) show the slag thicknesses, the average slag velocity and the temperature profiles along the combustor walls when all impacting particles are assumed to be captured. As expected, the slag layers are thicker, the average slag velocity is higher because of the increased particle momentum transfer and as a result, the inner and outer wall temperatures are lower on average than the cases with a particle capture submodel. In conclusion, a particle capture submodel is absolutely necessary, and the choice of a submodel and the critical Weber number is equally important, as it plays a big role in the results.

4.4.3. Temperature of Critical Viscosity

In this section, the influence of the temperature of critical viscosity, T_{cv}, on the slag model is presented. The change in mass deposition rate per unit area $\dot{m}_d''$ for three temperatures of critical viscosity: 1580 K, 1680 K and 1785 K can be seen in Figure 4-16(a(i)) through (c(i)). It can be observed that the mass deposition rate decreases with increasing temperature of critical viscosity. Although the slag surface is molten, as a result of the higher temperature of critical viscosity, more of the impacting particles are in the solid state and they also have a lower level of kinetic energy (see Figure 4-4(c) and (d)). Therefore, fewer particles are captured.

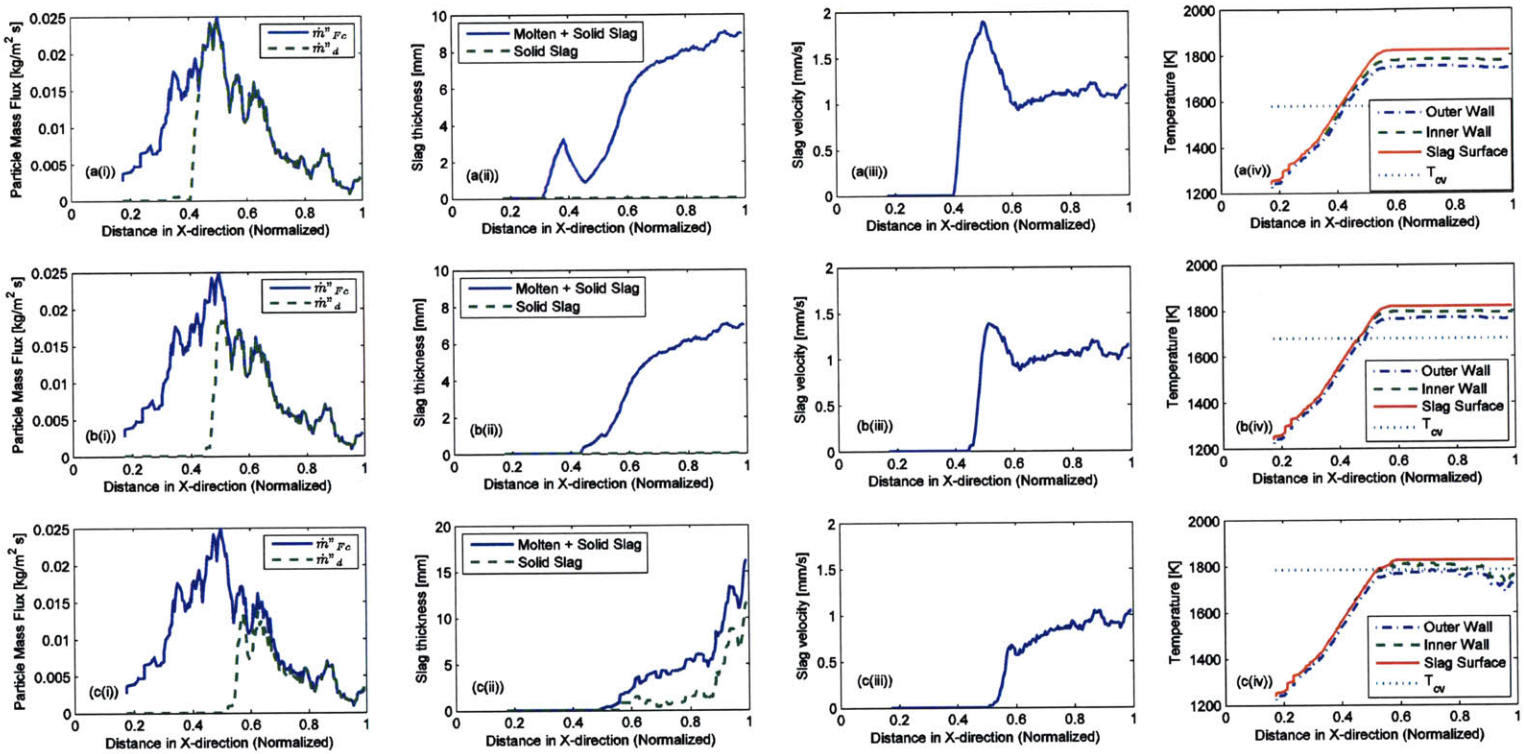

Figure 4-16 Influence of temperature of critical viscosity; (a) T_{cv} = 1580 K; (b) T_{cv} = 1680 K; (c) T_{cv} = 1785 K.

Since less particles are deposited, the slag layer is thinner (Figure 4-16(a(ii)) through (c(ii))). At the same time, lesser particle momentum is transferred to the slag layer resulting in a lower average slag viscosity transfer (Figure 4-15(a(iii)) through (c(iii))).

There also exists a layer of solid slag in the case where the temperatures of critical viscosity is 1785 K (Figure 4-16(c(ii))) because the inner wall temperature T_{wi} is lower than the temperature of critical viscosity T_{cv} (Figure 4-16 (c(iv))) which leads to the slag resolidification. Therefore, the task of maintaining the slag layer in the molten state is not an easy one given the variability of the temperature of critical viscosity, which is dependent on the coal type that is used.

4.5. Validation of Wall Burning Submodel

Since a fixed core model is currently used in the CFD as mentioned in Section 4.2.1, the wall burning submodel for porous char particles that is described in Section 3.3.3 is tested in this section by comparing it with results from Direct Numerical Simulation (DNS) [45]. The two important aspects of this submodel are presented in the next sections. First, the influence of combustor inclination on the particle sink positions along the reactor wall is shown and followed by the validation of the modified effective diffusivity of the wall burning sub-model for porous char with DNS simulations.

4.5.1. Particle Sink Position

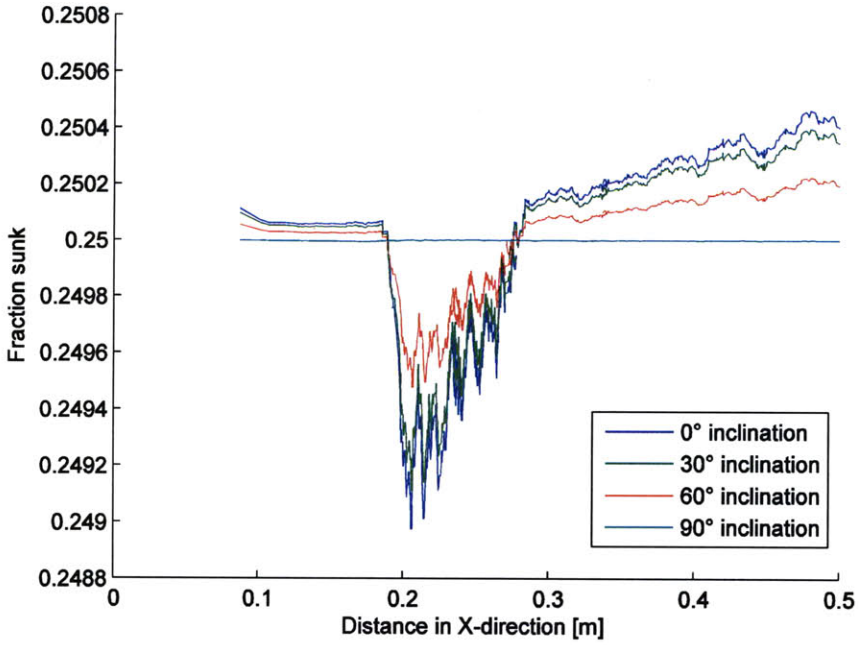

Figure 4-17 Sink positions for various reactor inclinations in the pressurized oxy-combustion case.

Particle sink position is dependent on the reactor inclination. Buoyancy force and weight, for instance, will not have an effect on a vertical reactor. Figure 4-17 shows the different sink positions of char particles along the walls at different reactor inclinations for the pressurized oxy-coal combustion case. The sink positions are given as a fraction of the vertical distance that a particle is sunk in the slag layer:

$$f = \frac{2s}{R_p} \tag{4-1}$$

where s is the sink position as shown in Figure 3-8 and R_p the particle radius.

It can be observed from Figure 4-17 that the particle weight and buoyancy force do not contribute much to the change in particle sink position. Approximately one quarter of a trapped particle is embedded within the slag layer, exposing the other three quarters to the oxidation environment within reactor. This is also true for the two-stage air blown gasification case.

4.5.2. Wall Burning of Porous Char

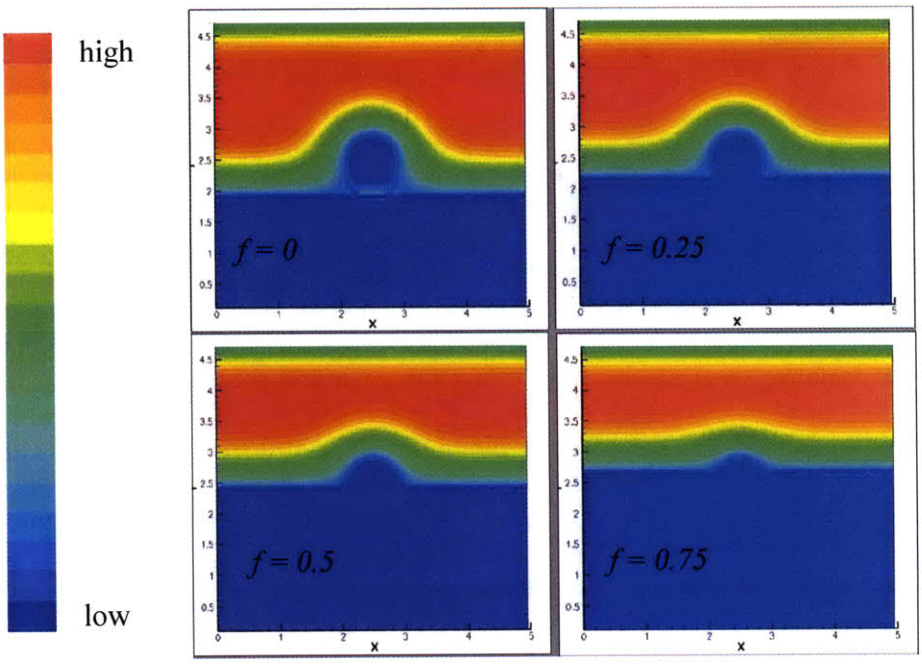

Figure 4-18 DNS simulation concentration profiles.

To test the validity of the proposed effective diffusivity for porous chars, simulations with Direct Numerical Simulation (DNS) were used [45]. In these simulations, the diffusivity coefficient within the particle is set to approximately 5% of the diffusivity coefficient of the environment. As time elapses, the species from the environment diffuses into the particle due to the species concentration gradient. The time histories of the total species concentration within the particle for different sink positions are recorded.

First, the species concentration within an isolated particle at different times is simulated. Then, as the particle is gradually sunk into a slag layer with an infinite diffusive resistance, the time history of the species concentration is recorded. Figure 4-18 shows the species concentration profiles for four different sink positions, f: 0, 0.25, 0.5 and 0.75. Note that the $f = 0$ case is to be differentiated from the isolated case because of the low species concentration in the vicinity of the particle lower region as depicted in Figure 4-18. The effective diffusivity correction factor, χ_{corr}, can then be derived by computing the ratio of species concentration in the sunken particles to the concentration of the isolated particle at after sufficient time has elapsed.

Figure 4-19 shows the comparison of the effective diffusivity correction factor, χ_{corr} , computed using DNS simulation (purple markers) and from Equation (3-1) from Section 3.3.3 (all lines). The different lines in the figure represent the varying of the foci of the constriction hyperbolas, b, described in Section 3.3.3. This parameter b can be used for fine-tuning the diffusivity correction factor for better accuracy. Overall, the figure shows a good agreement between the proposed wall burning submodel and the DNS simulations for all sunken fractions of the trapped particle.

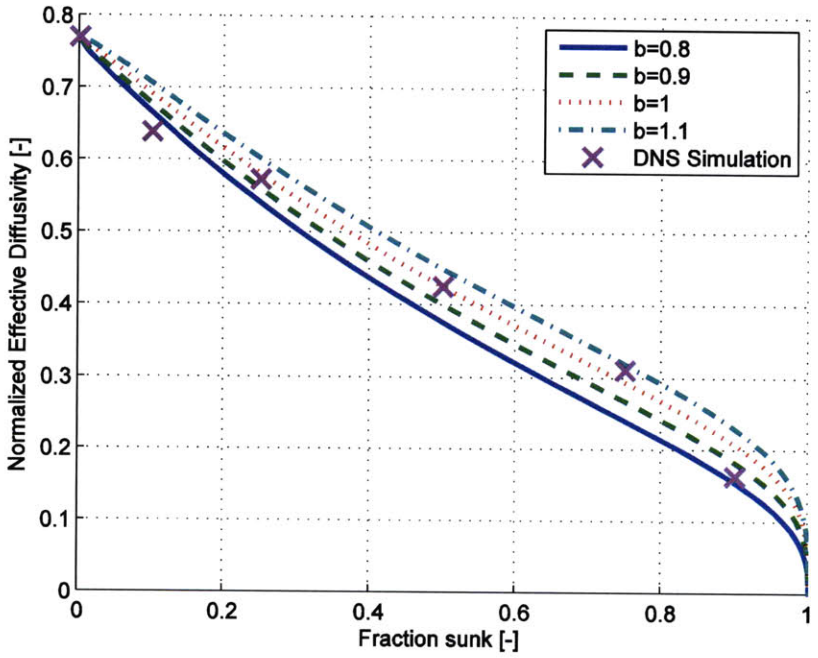

Figure 4-19 Comparison with DNS simulation.

4.6. Implementation in FLUENT

The slag model has been implemented in FLUENT® as User Defined Functions (UDFs) and the code is given in Appendix B. The code can be divided into three main sections: (i) the slag flow model and the thermal boundary condition, (ii) the particle capture submodel and data acquisition, and (iii) the discrete phase boundary condition. There are conveniently separated into different functions in the C code as described in the next sections.

It is noteworthy that the slag model is very sensitive to the initial inputs to the slag model. Therefore, it is important to ensure the convergence of the gaseous flow, combustion and radiation before the slag model is implemented as suggested by Benyon [9]. Benyon has further suggested the estimation for the initial wall temperature to be based on the temperature of critical viscosity plus 50 K in the slagging zone. Based on this initial wall temperature, the heat flux per unit area to the wall is computed or estimated before it is used as the initial input to the slag model. Iteration loops and relaxation factors are also recommended to assist in convergence.

4.6.1. Particle Capture Submodel and Data Acquisition UDF

Table 4-6 Description of UDMs for model inputs.

UDM	Description
F_UDMI(f,t,0)	Particle feed rate
F_UDMI(f,t,1)	Particle deposition rate
F_UDMI(f,t,2)	Number of trapped particles
F_UDMI(f,t,3)	Sum of x-velocities
F_UDMI(f,t,4)	Sum of particle diameters
F_UDMI(f,t,5)	Sum of particle temperatures
F_UDMI(f,t,6)	Sum of particle specific heats

The particle capture submodel and data acquisition are carried out in a function called `DEFINE_DPM_EROSION(dpm_slag_var,p,t,f,normal,alpha,Vmag,Mdot)` during the discrete phase computations. The model inputs from the CFD are stored in several User Defined Memories (UDMs) that uses the readily available CFD mesh. The definition of the UDMs for slag model inputs is given in Table 4-6.

The UDMs store the total particles feed and deposition rates, the total number of trapped particles and the sum of particle properties of each impacting particle to the particular wall computational cell and face that the particle is hitting. Note that the averaging of the particle properties is not performed in this UDF, but in the `DEFINE_PROFILE` function described in the next section.

4.6.2. Slag Flow Model and Thermal Boundary Condition UDF

Table 4-7 Description of UDMs for model outputs.

UDM	Description
F_UDMI(f,t,7)	Molten slag thickness, δ_l
F_UDMI(f,t,8)	Solid slag thickness, δ_{sld}
F_UDMI(f,t,9)	Local average slag velocity, u_{avg}
F_UDMI(f,t,10)	Slag mass flow rate, $\dot{m}_{ex}$
F_UDMI(f,t,11)	Heat loss rate per unit area, q_{loss}
F_UDMI(f,t,12)	Inner wall temperature, T_{wi}
F_UDMI(f,t,13)	Outer wall temperature, T_{wo}
F_UDMI(f,t,14)	Slag surface temperature, T_s
F_UDMI(f,t,15)	Cell heat transfer rate, $\dot{Q}_{ex,j}$
F_UDMI(f,t,16)	Heat flux per unit area to slag surface, q_{in}

The main slag model is written in a function called `double slag_model (face_t face)` and it is executed during every fluid phase computation by a function called `DEFINE_PROFILE(temperature_profile,t,i)`. This function also plays a role of assigning the model output, which is the wall temperature, to the CFD as a temperature boundary condition for the computations in the fluid phase. The slag model includes slag properties computations as well as the slag flow model that are described in Sections 3.4

and 3.3.1 respectively. The model outputs are then stored in UDMs that are also associated to the computational cells and faces that are readily determined by the CFD mesh as enumerated below in Table 4-7.

4.6.3. Discrete Phase Boundary Condition UDF

In this UDF, the boundary condition for the particles that impacts the wall is implemented. The in-built options that FLUENT offer include the "all reflect", "all trapped", "all escaped", etc. boundary conditions. This boundary condition is modified using a function called `DEFINE_DPM_BC(bc_wallcapture,p,t,f,f_normal,dim)`.

In this function, the particle capture submodel described in 3.3.2 is implemented. If a particle has a Weber number that exceeds the critical Weber number, that particle is reflected elastically. The velocity of the particle is thus modified to reflect its new direction. On the other hand, the tracking by the CFD of the particles that are trapped at the wall will be aborted. In other words, trapped particles are considered to have escaped from the CFD domain into the slag model domain. Conservation laws still apply since the mass, the momentum and the energy of the trapped particles are still accounted for in the slag layer computations.

4.7. Conclusions

The slag model introduced in Chapter 3 is applied to a slagging pressurized oxy-coal combustor and a two-stage air blown gasifier. First, the CFD framework and the reactor systems, in which the model is tested, were described, followed by the information about the model inputs. Then, the results of the slag model are presented and interpreted.

In the oxy-combustion case, only a molten slag layer is built-up from an axial location of approximately 0.4 L from the combustor inlet. The slag velocity is found to strongly depend on the momentum transfer from captured particles. This slag velocity, in turn, determines the rate at which the slag layer flows out of the combustor and thus, the molten slag thickness. The heat loss q_{loss}, as well as the outer wall temperature T_{wo} are also computed and among others, these variables are relatively more accessible for model validation purposes.

Similarly, a slag layer is observed to build up from an axially location of 0.8 L on the gasifier diffuser wall and no solid slag layer is formed. However, in contrast to the combustion case, fouling takes place at sections of the wall where the wall cooling solidifies the trapped particles and prevents them from forming a molten slag layer.

Sensitivity analysis of the reactor inclination carried out in Section 4.4.1 shows that particle momentum transfer from captured particles plays a significant role in the building up and flow of the slag layer. Moreover, the varying of the critical Weber number shows that the choice of a particle capture model is also very important. From the sensitivity analysis of the temperature of the critical temperature, we also conclude that the coal type that is used and hence, the temperature of critical viscosity notably influence the results of the slag model.

Given that particles trapped in a slag layer burn at a slower rate [17], a wall burning submodel has been developed to predict a modified particle volumetric devolatilization/consumption rate $\dot{m}_{vc}'''$ for porous particles. This wall burning submodel is tested by comparing the results with the Direct Numerical Simulation (DNS) [45]. The effective diffusivity correction factor, χ_{corr}, is found to be within reasonable agreement with the simulation results of the DNS. The particle weight and buoyancy force are also found to be insignificant in the determination of the particle sink position which in turn affects the particle volumetric reaction rate $\dot{m}_{vc}'''$, yielding a vertical sunken fraction of 25 ± 0.05 % for all reactor inclinations.

Finally, the different UDFs involved in the implementation of the slag model in FLUENT is described. Recommendations to ensure convergence is also presented based on Benyon's experience in implementing his slag model to the three dimensional pulverized coal fired furnace model developed by Pacific Power and the University of Sydney [9].

Chapter 5 Conclusions

5.1. Summary

A steady-state slag model is presented in this work. Firstly, the flow and energy characteristics of the slag layers are described. The model is capable of predicting local slag thicknesses, average molten slag velocity, heat fluxes and temperature profiles inside and outside the reactor. Improvements to existing slag models include the cubic temperature profile across the molten slag layer and the study of particle momentum contributions to the slag layer built-up. Particle momentum contribution is also shown to be significant.

Next, a particle capture submodel with a deterministic capture criterion is described. Initially, a check of the surface phase and the impacting particles phase is performed. This gives four different case permutations: (1) solid surface – solid particle, (2) liquid surface – liquid particle and (3) solid surface – liquid particle and (4) solid particle – liquid surface interactions. Various experiments in the literature have shown that all impacting particles in case (1) rebound and in case (2), they are all captured. For cases (3) and (4), the Weber number is used as a capture criterion because it considers particle velocity as well as impacting surface conditions. The critical Weber number is set to 1. However, in case (3), the trapped particle will not form a molten slag layer but instead fouls the reactor wall.

Finally, the model introduces and validates a wall burning submodel for porous char particles. A modified diffusivity coefficient with tortuosity and constriction correction

factors is explained in detail and a comparison with DNS simulations has shown a good agreement between them. The model also takes into consideration the temperature and composition dependent properties of coal slag. These properties are evaluated at the mean temperature of the molten slag layer, assuming a cubic temperature profile as aforementioned. The model is then tested in a pressurized oxy-coal combustion environment and a two stage air blown gasifier. The method to implement the slag model in a commercial CFD software, FLUENT is also presented.

5.2. Future Work and Challenges

Validation with experimental data is necessary for the slag model presented in this thesis. However, the harsh conditions within a combustor or gasifier make direct measurements during operation very challenging. An alternative way of confirmation is to validate the model as a whole with externally measureable variables such as outer wall temperature and heat losses to the coolant.

The following sections describe some areas that have been shown to be important from the sensitivity analyses in Section 4.4 and that need further attention for developing a more accurate slag model. The attempt to implement a two-way coupling of the slag model and the difficulties and challenges involved are also presented.

5.2.1. Particle Capture Submodel

The sensitivity analysis in Section 4.4.2 has shown that the critical Weber number plays a role in determining the slag layer flow and heat transfer characteristics. The analysis also points to the importance of the choice particle capture submodel. While a deterministic criterion is a significant step forward when compared to probabilistic criteria in the literature, the accuracy of the submodel remains untested. Experimental data is needed for the validation of the submodel. Alternatively, verification of the entire slag model can be used to indirectly substantiate the correctness of the submodel.

Besides that, the submodel assumes no mutual interference between trapped and impacting particles. At a high deposition rate and a low slag mass flow rate, this assumption no longer holds because trapped particles that are not fused with the slag layer will prevent impacting particles from reaching the slag surface and hence, from being trapped. This idea is the basis of the probabilistic approach in the work of Shimizu and Tominaga [13]. Montagnaro and Salatino [15] used this concept to determine coverage criterion of the slag surface by considering the particle capture, convective transport of trapped particles by the flowing slag. Hence, the submodel described in this work can be further refined by considering mutual interference of trapped and impacting. The effect of this extra criterion on the slag model also needs to be studied.

5.2.2. Slag Properties

In Section 4.4.3, the determination of the slag temperature of critical viscosity is found to have a significant influence on the results of the slag model. That makes the choice of a mathematical model for predicting the temperature difficult given the scarcity of experimental data and the variability of coal types. An experimental value of the temperature of critical viscosity is hence preferred.

Other slag properties such as the slag viscosity and thermal conductivity may also play a role in the prediction of the slagging characteristics. A sensitivity test on these slag properties is thus necessary. However, for some slag properties such as the specific heat, there lacks a variety of reliable models, which is also a consequence of the dearth of experimental data and the plethora of coal types. Therefore, a sensitivity study of the slag properties will identify the critical parameters that need more experimental validation.

5.2.3. Implementation in FLUENT

More work is necessary to improve the two-way coupling of the slag model with the CFD in both combustion and gasification environments. The implementation of the slag model in FLUENT in Section 4.6 is preliminary. The convergence is not yet fully guaranteed. The steps recommended by Benyon [9] as mentioned in Section 4.6 needs to be studied and tested. The introduction of iteration loops, relaxation factors and other convergence-aiding measures may also be necessary.

Once convergence can be guaranteed, the results of the slag model have to be reevaluated. Then, the effects of including a slag model on CFD simulation results can be studied in detail.

Appendix A Derivation of Constriction Correction Factor

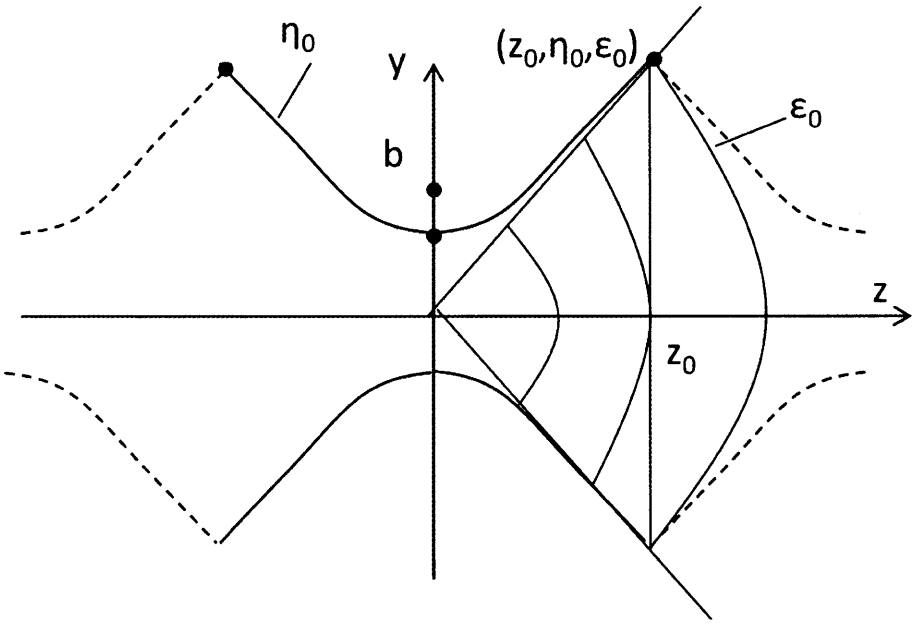

Figure A-1 A pore hyperbola in oblate spheroidal coordinates.

The derivation given in this appendix is based on the work of Petersen [25] and includes the addition of a tunability factor, b, which is also the focal point of the hyperbola in Figure A-1, for fitting the theoretical correction factor to experimental data if necessary. In oblate spheroidal coordinates, the coordinates ε and η for the hyperbola depicted in Figure A-1 are defined as:

$$\frac{y}{\eta_0} - \frac{z}{b^2 - \eta_0^2} = 1 \tag{1}$$

where η_0 is the axis intercept that is fixed at 0.7071.

The volume of the hyperbolic pore is therefore given as follows:

$$V = \pi \eta_0^2 \left(z_0 + \frac{z_0^3}{3\left(b^2 - \eta_0^2\right)} \right) \tag{2}$$

with z_0 being the half-length of the hyperbola (see Figure A-1). The value of z_0 is dependent on the sink position or the covered angle of the trapped particle and is explained in detail in a later part of this appendix.

The concentration profile in the pore is given by the solution to the Laplace equation for a dimensionless concentration, ς:

$$\varsigma = \frac{C(z) - C(0)}{C(z_0) - C(0)} \tag{3}$$

$$\nabla \varsigma = \frac{1}{\varepsilon^2 + \eta^2} \left\{ \frac{\partial}{\partial \varepsilon} \left[\left(1 + \varepsilon^2\right) \frac{\partial \varsigma}{\partial \varepsilon} \right] + \frac{\partial}{\partial \eta} \left[\left(1 - \eta^2\right) \frac{\partial \varsigma}{\partial \eta} \right] \right\} = 0 \tag{4}$$

$$\varsigma(z_0) = 1 \; ; \; \left(\frac{\partial \varsigma}{\partial \eta} \right)_{\eta = 0.7071} = 0 \; ;$$

with $$\varsigma(0) = 0 \; ; \; \left(\frac{\partial \varsigma}{\partial \eta} \right)_{\eta = 1} = 0 \tag{5}$$

To satisfy the boundary conditions (5), ς has to be independent of η [25] and is given as:

$$\varsigma = \frac{\tan^{-1}\varepsilon}{\tan^{-1}\varepsilon_0} \tag{6}$$

where ε_0 is a fitted parameter that is found to be:

$$\varepsilon_0 = \frac{2z_0}{1+\eta_0} \tag{7}$$

The net diffusive flow, N, through the hyperbolic pore can be derived and simplified to be [25]:

$$N = \frac{2\pi[C(z_0)-C(0)](1-\eta_0)D_{eff}}{\tan^{-1}\varepsilon_0} \tag{8}$$

On the other hand, the equivalent net diffusive flow through a series of cylindrical pores is given as follows:

$$N = \frac{[C(z_0)-C(0)]D_{\text{mod}}}{z_0^2} \tag{9}$$

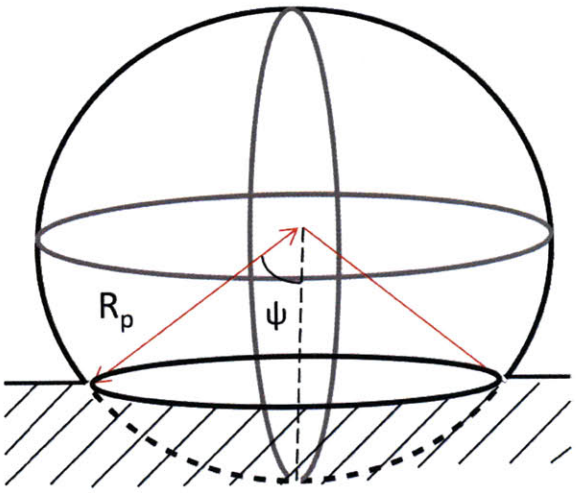

Figure A-2 Illustration of uncovered surface area of the particle spherical cap.

Equating Equations (2), (8) and (9), the constriction correction factor, σ_{corr}, is shown to be:

$$\sigma_{corr} = \frac{D_{\text{mod}}}{D_{eff}} = \frac{2(1-\eta_0)z_0^2}{\eta_0^2\left(z_0 + \frac{z_0^3}{3(b^2-\eta_0^2)}\right)\tan^{-1}\varepsilon_0} \tag{10}$$

The ratio of the maximum access area to the minimum surface area, β, can be formulated for the hyperbolic pore. Hence, z_0 and Equation (10) can be rewritten in terms of β as:

$$z_0 = (b^2-\eta_0^2)(\beta-1) \tag{11}$$

$$\sigma_{corr} = \frac{6(1-\eta_0)}{\eta_0^2(\beta+2)\tan^{-1}\varepsilon_0}\sqrt{(b^2-\eta_0^2)(\beta-1)} \tag{12}$$

For a particle that is trapped in a slag layer, the ratio of access area loss β can be approximated by the ratio of the total surface area of a sphere to the uncovered surface area of the particle spherical cap (see Figure A-2). β can be given in terms of the covered angle ψ (see Figure 3-8):

$$\beta = \frac{2}{1+\cos\psi} \tag{13}$$

Hence, the Equation (10) can once again be rewritten in terms of ψ:

$$\sigma_{corr} = \frac{6(1-\eta_0)}{\eta_0^2\left(\frac{2}{1+\cos\psi}+2\right)\tan^{-1}\varepsilon_0}\sqrt{\left(b^2-\eta_0^2\right)\left(\frac{2}{1+\cos\psi}-1\right)} \tag{14}$$

Appendix B Current Code for Coupling with CFD

```
/************************************************************************
Slag Model - Slag flow, char capture and slag properties
************************************************************************/
#include "udf.h"
#include "dpm.h"
#include "storage.h"
#include "sg_mem.h"
#include "mem.h"
#include "time.h"
#include "surf.h"
#include <math.h>
#include "string.h"

#define PI 3.14159265

/* Combustor constants */
#define D 1.2 /* [m] Combustor Diameter */
#define g 9.80665 /* gravitational constant*/
#define alpha_inc 1.5*PI/180.0 /* [rad] Combustor declination*/
#define T_c 343.0 /*[K] Coolant temperature*/
#define ho 9.0 /*[W/m^2 K] external heat transfer coefficient*/
#define kt_wall 28.88891  /* [W/m K] Wall thermal conductivity (tabular
                             alumina)*/
#define thick_wall 0.0508 /* [m] Wall thickness*/

/* Ash Properties (molten fractions) */
#define SiO2 0.535783768853335
#define Al2O3 0.219836175014401
#define TiO2 0.014178174654162
#define Fe2O3 0.020500290433469
#define CaO 0.049445873437529
#define MgO 0.056550150828708
#define Na2O 0.008900751677949
#define K2O  0.005162974725794
#define P2O5 0.005251808959018
#define MnO 3.172335052731592e-4
#define FeO 0.018695153130395
#define NiO 0.017982241934534
#define ZrO2 0.010900113684788
#define CaF2 0.017203232250343
#define B2O3 0.019292056910302
#define SO3  0.007706567689537
#define Fe 0.0
#define tot 1.377660931532268
#define T_cv 1.680e+3
```

```
Domain *domain;
int flag;

/* Slag flow model and slag properties */
double slag_model (face_t face)
{
       face_t f;
       domain = Get_Domain(1);
       Thread *t0, *t;
       cell_t c0;

       f=face;
       t = Lookup_Thread(domain, 6);

       int j;
       real P_VEL, P_DIAM, P_TEMP, P_CP, K1, K2, K3, q_in, xm, xa,
       alpha2, b0,b1,b2,b3,b,a, T_slag,T_slag_temp, miu_s, tot_W, V,
       rho_s, rho_s_temp, rho_solid, cp_s, cp_solid, kt_s,
       kt_solid,A_A,B_B,C_C,D_D,cum_sum,A[ND_ND];

       c0=F_C0(f,t);
       t0=F_C0_THREAD(f,t);
       F_AREA(A,f,t);
       q_in=MAX(0.0,BOUNDARY_HEAT_FLUX(f,t)/NV_MAG(A));
       if (F_UDMI(f,t,2)>0)
       {
              /* Average X-Velocities */
              P_VEL=F_UDMI(f,t,3)/F_UDMI(f,t,2);
              /* Average Particle Diameters */
              P_DIAM=F_UDMI(f,t,4)/F_UDMI(f,t,2);
              /* Average Particle Temperatures */
              P_TEMP=F_UDMI(f,t,5)/F_UDMI(f,t,2);
              /* Average Particle Specific Heats */
              P_CP=F_UDMI(f,t,6)/F_UDMI(f,t,2); }
       else
       {
              P_VEL=0.; /* Average X-Velocities */
              P_DIAM=0.; /* Average Particle Diameters */
              P_TEMP=0.; /* Average Particle Temperatures */
              P_CP=0.; /* Average Particle Specific Heats */
       }


       /* Temperature profile: 3rd order polynomial */
       if ((F_T(f,t))>=T_cv)
              T_slag=(5.*(F_T(f,t))+3.*T_cv)/8.0; /*[K]*/
       else
              T_slag=(F_T(f,t));
```

```
/* Viscosity Model */
xm = FeO+CaO+MgO+Na2O+K2O+MnO+NiO+2*(TiO2+ZrO2)+3*CaF2;
xa=Al2O3+Fe2O3+B2O3;
alpha2=xm/(xm+xa);
b0=13.8+39.9355*alpha2-44.049*alpha2*alpha2;
b1=30.481-117.1505*alpha2+129.9978*alpha2*alpha2;
b2=-40.9429+234.0486*alpha2-300.04*alpha2*alpha2;
b3=60.7619-153.9276*alpha2+211.1616*alpha2*alpha2;
b=b0+b1*SiO2+b2*SiO2*SiO2+b3*SiO2*SiO2*SiO2;
a=exp(-0.2693*b-13.9751); /*Urbain*/
/* a=exp(-0.2812*b-14.1305);% Kalmanovitch-Frank*/
miu_s=a*T_slag*exp(b*1000/T_slag);


/* Density Model */
tot_W=(SiO2*60.0844+Al2O3*101.9614+TiO2*79.8660+Fe2O3*159.6887+CaO
*56.0778+MgO*40.3045+Na2O*61.9790+P2O5*141.9447+MnO*70.9375+FeO*71
.8446+NiO*74.6929+CaF2*78.0752)*1e-3;
V=(SiO2*(19.55+7.9666*SiO2)+Al2O3*(28.31+32*Al2O3-3
1.45*Al2O3*Al2O3)+CaO*20.7+MgO*16.1+Na2O*33+FeO*15.8+Fe2O3*38.4+Mn
O*15.6+TiO2*24+P2O5*65.7+CaF2*31.3)*1e-6;
rho_s=tot_W/(V*(1+0.01/100*(T_slag-1773)));
rho_solid=tot_W/V/(1+0.01/100*(T_cv-1773));


/* Specific Heat Model */
cp_s=(SiO2*(55.98+ 15.40*1.e-3*T_slag+ 14.48*-
1.e5/T_slag/T_slag)+CaO*(48.82+ 4.52*1.e-3*T_slag+ 6.52*-
1.e5/T_slag/T_slag)+Al2O3*(115.00+ 11.80*1.e-3*T_slag+ 35.15*-
1.e5/T_slag/T_slag)+MgO*(42.60+ 7.45*1.e-3*T_slag+ 6.19*-
1.e5/T_slag/T_slag)+K2O*(65.7+ 22.60*1.e-3*T_slag+ 0.*-
1.e5/T_slag/T_slag)+Na2O*(65.7+ 22.60*1.e-3*T_slag+ 0.*-
1.e5/T_slag/T_slag)+TiO2*(75.19+ 1.17*1.e-3*T_slag+ 18.2*-
1.e5/T_slag/T_slag)+MnO*(46.48+ 8.12*1.e-3*T_slag+ 3.68*-
1.e5/T_slag/T_slag)+FeO*(48.78+ 8.36*1.e-3*T_slag+ 2.80*-
1.e5/T_slag/T_slag)+Fe2O3*(98.28+ 77.8*1.e-3*T_slag+ 14.85*-
1.e5/T_slag/T_slag)+Fe*(12.72+ 31.71*1.e-3*T_slag+ -2.51*-
1.e5/T_slag/T_slag)+P2O5*(182.5+ 46.4*1.e-3*T_slag+ 45.44*-
1.e5/T_slag/T_slag)+CaF2*(59.83+ 30.45*1.e-3*T_slag+ -1.96*-
1.e5/T_slag/T_slag)+SO3*(70.2+ 97.74*1.e-3*T_slag+ 0.*-
1.e5/T_slag/T_slag))*tot*10.;
cp_solid=(SiO2*87+CaO*80.8+Al2O3*146.4+MgO*90.4+K2O*74.0+Na2O*92.0
+TiO2*111.7+MnO*79.9+FeO*76.6+Fe2O3*191.2+Fe*43.9+P2O5*242.7+CaF2*
96.2+SO3*175.7)*tot*10;

if (cp_s>=1100)
      cp_s=cp_solid;


/* Thermal Conductivity Model */
kt_s=4.5e-7*rho_s*cp_s;
kt_solid=4.5e-7*rho_solid*cp_solid;
```

```
/*
F_UDMI(f,t,7): delta_l
F_UDMI(f,t,8): delta_s
F_UDMI(f,t,9): vel_l
F_UDMI(f,t,10): m_dot_l
F_UDMI(f,t,11): q_loss
F_UDMI(f,t,12): T_wi
F_UDMI(f,t,13): T_wo
F_UDMI(f,t,14): T_s
F_UDMI(f,t,15): Q_ex
F_UDMI(f,t,16):q_in
*/

/* Molten Slag Flow Model */
K1=0.0;
if (f>=150)
{
       for (j=f;j<230;j++)
       {
              /* Temperature profile: 3rd order polynomial */
              if ((F_T(j,t))>=T_cv)
                     T_slag_temp=(5.*(F_T(j,t))+3.*T_cv)/8.0;
                     /*[K]*/
              else
                     T_slag_temp=(F_T(j,t));
              rho_s_temp=tot_W/(V*(1.+0.01/100.*(T_slag_temp-
              1773.)));

              K1=K1+F_UDMI(j,t,1)/(rho_s_temp*PI*D);
       }
       for (j=0;j<150;j++)
       {
              /* Temperature profile: 3rd order polynomial */
              if ((F_T(j,t))>=T_cv)
                     T_slag_temp=(5.*(F_T(j,t))+3.*T_cv)/8.0;
                     /*[K]*/
              else
                     T_slag_temp=(F_T(j,t));
              rho_s_temp=tot_W/(V*(1.+0.01/100.*(T_slag_temp-
              1773.)));

              K1=K1+F_UDMI(j,t,1)/(rho_s_temp*PI*D);
       }
}
else
{
       for (j=f;j<150;j++)
       {
              /* Temperature profile: 3rd order polynomial */
              if ((F_T(j,t))>=T_cv)
                     T_slag_temp=(5.*(F_T(j,t))+3.*T_cv)/8.0;
                     /*[K]*/
              else
```

```
                T_slag_temp=(F_T(j,t));
            rho_s_temp=tot_W/(V*(1.+0.01/100.*(T_slag_temp-
            1773.)));

            K1=K1+F_UDMI(j,t,1)/(rho_s_temp*PI*D);
        }
}
K2=F_UDMI(f,t,1)*MAX(DPM_SMALL,P_VEL)*MAX(DPM_SMALL,P_VEL)/MAX(DPM
_SMALL,(4*NV_MAG(A)*miu_s*K1));
K3=rho_s*g*sin(alpha_inc)/(3*miu_s);
F_UDMI(f,t,7)=MAX(DPM_SMALL,pow((K1/MAX(DPM_SMALL,(K2+K3))),0.3333
333)); /* Molten slag thickness [m]*/
F_UDMI(f,t,9)=K1/MAX(DPM_SMALL,F_UDMI(f,t,7)); /* Molten slag
velocity [m/s]*/
F_UDMI(f,t,10)=rho_s*F_UDMI(f,t,9)*F_UDMI(f,t,7); /* Molten slag
mass flow rate*/

/* Heat Input */
cum_sum=0.0;
if (f>=150)
{
        for (j=f;j<230;j++)
        {
            if     (F_UDMI(j,t,1)!=F_UDMI(j,t,1))
                F_UDMI(j,t,1)=0.;
            cum_sum+=F_UDMI(j,t,1);
        }
        for (j=0;j<150;j++)
        {
            if     (F_UDMI(j,t,1)!=F_UDMI(j,t,1))
                F_UDMI(j,t,1)=0.;
            cum_sum+=F_UDMI(j,t,1);
        }
}
else
{
        for (j=f;j<150;j++)
        {
                                    if
(F_UDMI(j,t,1)!=F_UDMI(j,t,1))
                    F_UDMI(j,t,1)=0.;
            cum_sum+=F_UDMI(j,t,1);
        }
}

A_A=rho_s*cp_s*PI*D*F_UDMI(f,t,7)*F_UDMI(f,t,7)*F_UDMI(f,t,7)/miu_
s;
B_B=-F_UDMI(f,t,7)/2./kt_s*(rho_s*g*sin(alpha_inc)*11./120.
+4.*MAX(DPM_SMALL,P_VEL)*MAX(DPM_SMALL,P_VEL)*F_UDMI(f,t,1)*rho_s/
MAX(DPM_SMALL,4.*NV_MAG(A)/PI/D*cum_sum)/15.);
C_C=rho_s*g*sin(alpha_inc)*61./240.+4.*MAX(DPM_SMALL,P_VEL)*MAX(DP
M_SMALL,P_VEL)*F_UDMI(f,t,1)*rho_s/MAX(DPM_SMALL,4.*NV_MAG(A)/PI/D
*cum_sum)/5.;
```

```
D_D=rho_s*g*sin(alpha_inc)*19./240.+MAX(DPM_SMALL,P_VEL)*MAX(DPM_S
MALL,P_VEL)*F_UDMI(f,t,1)*rho_s/MAX(DPM_SMALL,4.*NV_MAG(A)/PI/D*cu
m_sum)/5.;
F_UDMI(f,t,8)=0.0;
if (f==149)
{
       F_UDMI(f,t,11)=(q_in*(NV_MAG(A)-A_A*B_B-
       A_A*C_C*F_UDMI(f,t,7)/(3.*kt_s))+F_UDMI(f,t,1)*P_CP*P_TEMP-
       T_c*A_A*(C_C+D_D))/(NV_MAG(A)+A_A*(C_C+D_D)*(thick_wall
       /kt_wall+1./ho)+A_A*C_C*F_UDMI(f,t,7)/1.5/kt_s);
}
else if (f==229)
{
       if (F_UDMI(0,t,15) !=F_UDMI(0,t,15))
              F_UDMI(0,t,15)=0.0;
       F_UDMI(f,t,11)=(q_in*(NV_MAG(A)-A_A*B_B-
       A_A*C_C*F_UDMI(f,t,7)/(3.*kt_s))+F_UDMI(f,t,1)*P_CP*P_TEMP
       +F_UDMI(0,t,15)-T_c*A_A*(C_C+D_D))/(NV_MAG(A)+A_A*(C_C+D_D)
       *(thick_wall/kt_wall+1./ho)+A_A*C_C*F_UDMI(f,t,7)/1.5/kt_s);
}
else
{
       if (F_UDMI(f+1,t,15) !=F_UDMI(f+1,t,15))
              F_UDMI(f+1,t,15)=0.0;
       F_UDMI(f,t,11)=(q_in*(NV_MAG(A)-A_A*B_B-
       A_A*C_C*F_UDMI(f,t,7)/(3.*kt_s))+F_UDMI(f,t,1)*P_CP
       *P_TEMP+F_UDMI(f+1,t,15)-T_c*A_A*(C_C+D_D))/(NV_MAG(A)
       +A_A*(C_C+D_D)*(thick_wall/kt_wall+1./ho)+A_A*C_C
       *F_UDMI(f,t,7)/1.5/kt_s);
}

F_UDMI(f,t,14)=MIN(2000,MAX(1000,F_UDMI(f,t,11)*(F_UDMI(f,t,7)/1.5
/kt_s+thick_wall/kt_wall+1./ho)+q_in*F_UDMI(f,t,1)/3./kt_s+T_c));
F_UDMI(f,t,12)=F_UDMI(f,t,11)*(thick_wall/kt_wall+1./ho)+T_c;
F_UDMI(f,t,15)=A_A*(B_B*q_in+C_C*F_UDMI(f,t,14)+D_D*F_UDMI(f,t,12)
);
F_UDMI(f,t,13)=F_UDMI(f,t,11)/ho+T_c;

/* Resolidification */
if (F_UDMI(f,t,12)<T_cv && F_UDMI(f,t,14)>T_cv)
{
       if (f==149)
       {
              F_UDMI(f,t,11)=(q_in*(NV_MAG(A)-A_A*B_B-
              A_A*C_C*F_UDMI(f,t,7)/(3.*kt_s))+F_UDMI(f,t,1)
              *P_CP*P_TEMP-T_cv*A_A*(C_C+D_D))/(NV_MAG(A)+A_A*C_C
              *F_UDMI(f,t,7)/1.5/kt_s);
       }
       else if (f==229)
       {
              if (F_UDMI(0,t,15) !=F_UDMI(0,t,15))
                     F_UDMI(0,t,15)=0.0;
```

```
                F_UDMI(f,t,11)=(q_in*(NV_MAG(A)-A_A*B_B-
                A_A*C_C*F_UDMI(f,t,7)/(3.*kt_s))+F_UDMI(f,t,1)
                *P_CP*P_TEMP+F_UDMI(0,t,15)-T_cv*A_A*(C_C+D_D))
                /(NV_MAG(A)+A_A*C_C*F_UDMI(f,t,7)/1.5/kt_s);
        }
        else
        {
                if (F_UDMI(f+1,t,15) !=F_UDMI(f+1,t,15))
                        F_UDMI(f+1,t,15)=0.0;
                F_UDMI(f,t,11)=(q_in*(NV_MAG(A)-A_A*B_B-
                A_A*C_C*F_UDMI(f,t,7)/(3.*kt_s))+F_UDMI(f,t,1)
                *P_CP*P_TEMP+F_UDMI(f+1,t,15)-T_cv*A_A*(C_C+D_D))
                /(NV_MAG(A)+A_A*C_C*F_UDMI(f,t,7)/1.5/kt_s);
        }

        F_UDMI(f,t,8)=((T_cv-T_c)/F_UDMI(f,t,11)-thick_wall/kt_wall-
        1./ho)*kt_solid;

F_UDMI(f,t,14)=MIN(2000,MAX(1000,((F_UDMI(f,t,11)+q_in/2.)*F_UDMI(
f,t,7)/1.5/kt_s+T_cv)));
        F_UDMI(f,t,15)=A_A*(B_B*q_in+C_C*F_UDMI(f,t,14)+D_D*T_cv);
        F_UDMI(f,t,13)=F_UDMI(f,t,11)/ho+T_c;
        F_UDMI(f,t,12)=F_UDMI(f,t,11)*(thick_wall/kt_wall+1/ho)+T_c;
}
F_UDMI(f,t,8)=A_A;
F_UDMI(f,t,9)=B_B;
F_UDMI(f,t,12)=C_C;
F_UDMI(f,t,13)=D_D;
C_UDMI(c0,t0,7)=F_UDMI(f,t,7);
C_UDMI(c0,t0,8)=F_UDMI(f,t,8);
C_UDMI(c0,t0,9)=F_UDMI(f,t,9);
C_UDMI(c0,t0,10)=F_UDMI(f,t,10);
C_UDMI(c0,t0,11)=F_UDMI(f,t,11);
C_UDMI(c0,t0,12)=F_UDMI(f,t,12);
C_UDMI(c0,t0,13)=F_UDMI(f,t,13);
C_UDMI(c0,t0,14)=F_UDMI(f,t,14);
C_UDMI(c0,t0,15)=F_UDMI(f,t,15);
F_UDMI(f,t,16)=q_in;
C_UDMI(c0,t0,16)=F_UDMI(f,t,16);
/*return F_T(f,t);*/
return F_UDMI(f,t,14);
}

/* Particle Capture Model and Preparation of Data to Faces */
DEFINE_DPM_EROSION(dpm_slag_var,p,t,f,normal,alpha,Vmag,Mdot)
{
        Thread *t0;
        cell_t c0;
        real T_slag,tot_W, V, rho_s, sigma_s,sigma_p,sigma_sp,We;
        int i;


        if (flag>0)
```

```
{
        Message("Reset\n");
        begin_f_loop(f,t)
        {
                for (i=0;i<7;i++)
                        F_UDMI(f,t,i)=0.;
        }
        end_f_loop(f,t)
        flag=0;
}

c0=F_C0(f,t);
t0=F_C0_THREAD(f,t);

/* Temperature profile: 3rd order polynomial */
if ((F_T(f,t))>=T_cv)
T_slag=(5.*(F_T(f,t))+3.*T_cv)/8.0; /*[K]*/
else
T_slag=(F_T(f,t));

/* Recalculation of temperature profile with heat input */
tot_W=(SiO2*60.0844+Al2O3*101.9614+TiO2*79.8660+Fe2O3*159.6887+CaO
*56.0778+MgO*40.3045+Na2O*61.9790+P2O5*141.9447+MnO*70.9375+FeO
*71.8446+NiO*74.6929+CaF2*78.0752)*1e-3;
V=(SiO2*(19.55+7.9666*SiO2)+Al2O3*(28.31+32*Al2O3-
31.45*Al2O3*Al2O3)+CaO*20.7+MgO*16.1+Na2O*33+FeO*15.8+Fe2O3*38.4
+MnO*15.6+TiO2*24+P2O5*65.7+CaF2*31.3)*1e-6;
rho_s=tot_W/(V*(1+0.01/100*(T_slag-1773)));

/* Surface Tension Model */
sigma_s=(SiO2*260+CaO*625+Al2O3*655+MgO*635+FeO*645+MnO*645+TiO2
*350-3.7-2972*Fe2O3+14312*Fe2O3*Fe2O3+0.8-1388*Na2O-6723
*Na2O*Na2O+0.8-1388*K2O-6723*K2O*K2O-5.2-
3454*P2O5+22178*P2O5*P2O5)*1e-3-0.15e-3*(T_slag-1733);
sigma_p=(SiO2*260+CaO*625+Al2O3*655+MgO*635+FeO*645+MnO*645+TiO2
*350-3.7-2972*Fe2O3+14312*Fe2O3*Fe2O3+0.8-1388*Na2O-6723*Na2O
*Na2O+0.8-1388*K2O-6723*K2O*K2O-5.2-3454*P2O5+22178*P2O5*P2O5)
*1e-3-0.15e-3*(P_T(p)-1733);

/*
F_UDMI(f,t,0): Particle Feed Rate
F_UDMI(f,t,1): Particle Deposition Rate
F_UDMI(f,t,2): Number of Trapped Particles
F_UDMI(f,t,3): Sum of X-Velocities
F_UDMI(f,t,4): Sum of Particle Diameters
F_UDMI(f,t,5): Sum of Particle Temperatures
F_UDMI(f,t,6): Sum of Particle Specific Heats
*/

F_UDMI(f,t,0)+=P_FLOW_RATE(p);
/* Char Capture Model */
sigma_sp=sigma_p-sigma_s*cos(2.094395102393195); /*120deg*/
We=rho_s*P_VEL(p)[1]*P_VEL(p)[1]*P_DIAM(p)/sigma_sp;
```

```
        /* Solid-solid interaction (all rebound) and Liquid-solid
        interaction,We>1 (rebound)*/
        if (((P_T(p)>=T_cv) && (F_T(f,t)>=T_cv))||(!((P_T(p)<T_cv)
        && (F_T(f,t)<T_cv))&&(We<1.0)))
        {
                F_UDMI(f,t,1)+=P_FLOW_RATE(p);
                F_UDMI(f,t,2)+=1.0;
                F_UDMI(f,t,3)+=P_VEL(p)[0];
                F_UDMI(f,t,4)+=P_DIAM(p);
                F_UDMI(f,t,5)+=P_T(p);
                F_UDMI(f,t,6)+=DPM_SPECIFIC_HEAT(p,P_T(p));
        }
        F_UDMI(f,t,14)=F_T(f,t);
        C_UDMI(c0,t0,14)=F_UDMI(f,t,14);
        C_UDMI(c0,t0,0)=F_UDMI(f,t,0);
        C_UDMI(c0,t0,1)=F_UDMI(f,t,1);
        C_UDMI(c0,t0,2)=F_UDMI(f,t,2);
        C_UDMI(c0,t0,3)=F_UDMI(f,t,3);
        C_UDMI(c0,t0,4)=F_UDMI(f,t,4);
        C_UDMI(c0,t0,5)=F_UDMI(f,t,5);
        C_UDMI(c0,t0,6)=F_UDMI(f,t,6);

}

/* Heat flux boundary condition profile */
DEFINE_PROFILE(temperature_profile,t,i)
{
        face_t f;
        domain = Get_Domain(1);
        Thread *th;
        th = Lookup_Thread(domain, 6);

        if (t==th)
        {
                for (f=149;f>=0;f--)
                {
                        F_PROFILE(f,t,i) = slag_model(f);
                }
                for (f=229;f>=150;f--)
                {
                        F_PROFILE(f,t,i) = slag_model(f);
                }
        }
        flag++;
}

/* Wall capture model */
DEFINE_DPM_BC(bc_wallcapture,p,t,f,f_normal,dim)
{
        real normal[3];
        real rel_vel[3];
        real face_vel[3];
        real rel_dot_n, vmag, vnew, sigma_p;
```

```
real weber_in, weber_out;
cxboolean moving = (SV_ALLOCATED_P (t,SV_WALL_GRID_V) &&
SV_ALLOCATED_P (t,SV_WALL_V ) );

Thread *t0;
cell_t c0;

real alpha; /* angle of particle path with face normal */
real vn=0.;
/*real nor_coeff = 1.;
real tan_coeff = 0.3; */
int i, idim = dim;
real NV_VEC(x);
#if RP_2D
/* dim is always 2 in 2D compilation. Need special treatment for
2d axisymmetric and swirl flows */
       if (rp_axi_swirl)
       {
              real R = sqrt(p->state.pos[1]*p->state.pos[1] + p-
              >state.pos[2]*p->state.pos[2]);
              if (R > 1.e-20)
              {
                     idim = 3;
                     normal[0] = f_normal[0];
                     normal[1] = (f_normal[1]*p->state.pos[1])/R;
                     normal[2] = (f_normal[1]*p->state.pos[2])/R;
              }
              else
              {
                     for (i=0; i<idim; i++)
                            normal[i] = f_normal[i];
              }
       }
       else
#endif
       for (i=0; i<idim; i++)
              normal[i] = f_normal[i];

       c0=F_C0(f,t);
       t0=F_C0_THREAD(f,t);

/* Set up velocity vectors and calculate the Weber number
to determine the regime. */
for (i=0; i < idim; i++)
{
       if (moving)
              face_vel[i] = WALL_F_VV(f,t)[i] +
              WALL_F_GRID_VV(f,t)[i];
       else
              face_vel[i] = 0.0;
       rel_vel[i] = P_VEL(p)[i] - face_vel[i];
}
vmag = MAX(NV_MAG(rel_vel),DPM_SMALL);
```

```
rel_dot_n = MAX(NV_DOT(rel_vel,normal),DPM_SMALL);
sigma_p=(SiO2*260+CaO*625+Al2O3*655+MgO*635+FeO*645+MnO*645+TiO2
*350-3.7-2972*Fe2O3+14312*Fe2O3*Fe2O3+0.8-1388*Na2O-6723*Na2O
*Na2O+0.8-1388*K2O-6723*K2O*K2O-5.2-3454*P2O5+22178*P2O5*P2O5)
*1e-3-0.15e-3*(P_T(p)-1733);
weber_in = P_RHO(p) * (rel_dot_n)*(rel_dot_n) * P_DIAM(p)
/MAX(sigma_p,DPM_SMALL);

/* Solid-solid interaction and solid-liquid interaction where
kinetic energy is greater than surface tension energy and solid */
if (((P_T(p)<T_cv) && (F_T(f,t)<T_cv))||(!((P_T(p)>=T_cv) && (
F_T(f,t)>=T_cv))&&(weber_in>=1.0)))
{
      alpha = M_PI/2. - acos(MAX(-1.,MIN(1.,NV_DOT(normal,p-
      >state.V)/MAX(NV_MAG(p->state.V),DPM_SMALL))));
      if ((NNULLP(t)) && (THREAD_TYPE(t) == THREAD_F_WALL))
            F_CENTROID(x,f,t);
      /* calculate the normal component, rescale its magnitude by
      the coefficient of restitution and subtract the change */
      /* Compute normal velocity. */
      for(i=0; i<idim; i++)
            vn += p->state.V[i]*normal[i];
      /* Subtract off normal velocity. */
      for(i=0; i<idim; i++)
            p->state.V[i] -= vn*normal[i];
      /* Apply tangential coefficient of restitution. */
      for(i=0; i<idim; i++)
            p->state.V[i] *= 1.;
      /* Add reflected normal velocity. */
      for(i=0; i<idim; i++)
            p->state.V[i] -= 1.*vn*normal[i];

      /* Store new velocity in state0 of particle */
      for(i=0; i<idim; i++)
            p->state0.V[i] = p->state.V[i];
      return PATH_ACTIVE;
}

/* Liquid-liquid interaction and solid-liquid interaction where
kinetic energy is smaller than surface tension energy */
else /*if ((P_T(p)>T_cv && (F_T(f,t))>T_cv)|| (weber_in<1.))*/
{
      alpha = M_PI/2. - acos(MAX(-1.,MIN(1.,NV_DOT(normal,p-
      >state.V)/MAX(NV_MAG(p->state.V),DPM_SMALL))));
      if ((NNULLP(t)) && (THREAD_TYPE(t) == THREAD_F_WALL))
            F_CENTROID(x,f,t);
      /* calculate the normal component, rescale its magnitude by
      the coefficient of restitution and subtract the change */
      /* Compute normal velocity. */
      for(i=0; i<idim; i++)
            vn += p->state.V[i]*normal[i];
      /* Subtract off normal velocity. */
      for(i=0; i<idim; i++)
```

```
                p->state.V[i] -= vn*normal[i];
            /* Apply tangential coefficient of restitution. */
            for(i=0; i<idim; i++)
                p->state.V[i] *= 1.;
            /* Add reflected normal velocity. */
            for(i=0; i<idim; i++)
                p->state.V[i] -= 0.*vn*normal[i];

            /* Apply new axial velocity. */
            /*p->state.V[0] = 0.0;/*F_UDMI(f,t,9);*/
            /* Store new velocity in state0 of particle */
            for(i=0; i<idim; i++)
                p->state0.V[i] = p->state.V[i];
            return PATH_ABORT;
        }
}
```

References

[1] Key World Energy Statistics. : International Energy Agency, 2009.

[2] Freme F, U.S. Coal Supply and Demand: 2008 Review.

[3] MIT, The Future of Coal - An Interdisciplinary MIT Study. , 2007.

[4] Federal Highway Administration (FHWA), American Coal Ash Association (ACAA) Fly Ash Facts for Highway Engineers. 2003;FHWA-IF-03-019:76 p.

[5] American Coal Ash Association (ACAA) 2008 Coal Combustion Product (CCP) Production and Use. 2008.

[6] American Coal Ash Association (ACAA) Coal Combustion Products: Beneficial Use - Simply Recycling by Another Name. 2009.

[7] Recycled Materials Resource Center User Guidelines for Waste and Secondary By-Product Materials in Pavement Construction. 2008.

[8] NETL, National Energy Technology Laboratory Clean coal technology: coal utilization by-products. 2006;Topical report no. 24:28 p.

[9] Benyon PJ, Computational Modelling of Entrained Flow Slagging Gasifiers. PhD Thesis, University of Sydney, 2002.

[10] Seggiani M, Modelling and simulation of time varying slag flow in a Prenflo entrained-flow gasifier. Fuel 1998;77:1611-21.

[11] Bockelie M. J., Denison M. K., Chen Z., Senior C. L., Linjewile T.and Sarofim A.F., CFD Modeling For Entrained Flow Gasifiers in Vision 21 Systems,2002, Sept 24-26, Proceedings of the 19th Annual International Pittburgh Coal Conference, Pittsburgh, PA, USA.

[12] Wang XH, Zhao DQ, He LB, Jiang LQ, He Q, Chen Y, Modeling of a coal-fired slagging combustor: Development of a slag submodel. Combust Flame 2 007;149:249-60. doi:10.1016/j.combustflame.2007.02.001.

[13] Shimizu T, Tominaga H, A model of char capture by molten slag surface under high-temperature gasification conditions. Fuel 2006;85:170-8. doi:10.1016/j.fuel.2005.03.033.

[14] Tominaga H, Tamashita T, Ando T, Asahiro N, Simulator Development of Entrained Flow Coal Gasifiers at High Temperature & High Pressure Atmosphere. IFRF Combustion Journal 2000.

[15] Montagnaro F, Salatino P, Analysis of char-slag interaction and near-wall particle segregation in entrained-flow gasification of coal. Combustion and Flame 2010;157:874-83.

[16] Emory SF, Berg JC, Surface Tension Effects on Particle Collection Efficiency. Industrial & Engineering Chemistry Fundamentals 1978;17:225-7. doi:10.1021/i160067a016.

[17] Noda R, Naruse I, Ohtake K, Fundamentals on combustion and gasification behavior of coal particle trapped on molten slag layer. J Chem Eng Jpn 1996;29:235-41.

[18] Hsiao M, Lichter S, Quintero LG, The critical Weber number for vortex and jet f ormation for drops impinging on a liquid pool. Physics of Fluids 1988;31:3560-2.

[19] Richards GH, Slater PN, Harb JN, Simulation of Ash Deposit Growth in a Pulverized Coal-Fired Pilot-Scale Reactor. Energy Fuels 1993;7:774-81.

[20] Shannon GN, Rozelle PL, Pisupati SV, Sridhar S, Conditions for entrainment into a FeOx containing slag for a carbon-containing particle in an entrained coal gasifier. Fuel Processing Technology 2008;89:1379-85. doi:10.1016/j.fuproc.2008.06.010.

[21] Senda J, Kobayashi M, Iwashita S, Fujimoto H, Modeling of diesel spray impinging on flat wall. JSME Int J Ser B-Fluids Therm Eng 1996;39:859-66.

[22] Bhatia SK, Perlmutter DD, A Random Pore Model for Fluid-Solid Reactions, 1. Isothermal, Kinetic Control. Aiche J 1980;26:379-86.

[23] Petersen EE, Reaction of Porous Solids. Aiche J 1957;3:443-8.

[24] Fogler HS, Elements of Chemical Engineering. : Prentice Hall, 2004.

[25] Petersen EE, Diffusion in a Pore of Varying Cross Section. Aiche J 1958;4:343-5.

[26] Mills KC, Rhine JM, The Measurement and Estimation of the Physical Properties of Slags Formed during Coal Gasification, 1. Properties Relevant to Fluid-Flow. Fuel 1989;68:193-200.

[27] Corey RC, Measurement and Significance of the Flow Properties of Coal-Ash Slag. : United States. Bureau of Mines., 1964.

[28] Watt JD, Fereday F, The Flow Properties of Slags Formed from the Ashes of British Coals: Part 1 Viscosity of Homogeneous Liquid Slags in Relation to Slag Composition. Journal of the Institute of Fuel 1969;42:99-103.

[29] Nowok JW, Hurley JP, Steadman EN, A New Approach to Calculating Coal Ash Viscosity. In: Williamson J and Wigley F, editors. The impact of ash deposition on coal fired plants. Washington, DC: Taylor & Francis, 1993:527.

[30] Patterson JH, Hurst HJ, Quintanar A, Boyd BK, Tran H, Evaluation of the slag flow characterization of Australian coals in slagging gasifiers. 2001;Research Report 19, Volume 1.

[31] Vargas S, Frandsen FJ, Dam-Johansen K, Rheological properties of high-temperature melts of coal ashes and other silicates. Prog Energy Combust Sci 2001;27:237-429.

[32] Mills KC, Rhine JM, The Measurement and Estimation of the Physical Properties of Slag Formed during Coal Gasfication, 2. Properties Relevant to Heat-Transfer. Fuel 1989;68:904-10.

[33] Hong J, Chaudhry G, Brisson JG, Field R, Gazzino M, Ghoniem AF, Analysis of oxy-fuel combustion power cycle utilizing a pressurized coal combustor. Energy 2009;34:1332-40. doi:10.1016/j.energy.2009.05.015.

[34] Benelli G., Malavasi M., Girardi G., Oxy-coal Combustion Process Suitable for Future and more Efficient Zero Emission Power Plants, 26-28 June 2007, PowerGen Europe Conference and Exhibition, Madrid, Spain.

[35] Gazzino M., Benelli G., Pressurised Oxy-Coal Combustion Rankine-Cycle for Future Zero Emission Power Plants: Process Design and Energy Analysis, August 10-14, 2008,ASME ES2008, Jacksonville, Florida, USA.

[36] Malavasi M., Rosetti E, High-Efficiency Combustors with Reduced Environmental Impact and Processes for Power Generation Derivable Therefrom, International Patent. *International Publication Number WO 2005/108867*, 17 November 2005..

[37] Malavasi M., Allouis C., D'Anna A., Flameless Technology for Particulate Emissions Suppression, April 26-28, 2009, Combustion Colloquia, Italian Section of the Combustion Institute, Napoli, Italy.

[38] Malavasi M., Di Salvia G., Rossetti E. Combustion process, International Patent. *International Publication Number WO 2009/071239*, 11 June 2009.

[39] Rossetti E., MM, Method and Plant for the Treatment of Materials in Particular Waste Materials and Refuse, International Patent. *International Publication Number WO 2004/094904*, 4 November 2004.

[40] Chen L., Gazzino M. and Ghoniem A. F., Characteristics of Pressurized Oxy-Coal Combustion under Increasing Swirl Number, June 6-10, 2010, *Proceedings of the 35th International Technical Conference on Clean Coal & Fuel Systems,*Clearwater, FL, USA.

[41] Kumar M., Zhang C., Monaghan R. F. D., Singer S. L. and Ghoniem A. F., CFD Simulation of Entrained Flow Gasification with Improved Devolatilization and Char Consumption Submodels, November 13-19, Proceedings of the ASME 2009 , International Mechanical Engineering Congress & Exposition, Lake Buena Vista, Florida, USA.

[42] Oya A, Fukatsu T, Otani S, Marsh H, Catalytic Graphitization of Cokes by Indigeneous Mineral Matter. Fuel 1983;62:502-7.

[43] Soo SL, Instrumentation for Fluid-Particle Flow. : William Andrew Publishing/Noyes, 1999.

[44] Bockelie M. J., Denison M. K., Chen Z., et al. CFD modeling for Entrained Flow Gasifiers, Oct.28-30, 2002, Proceedings of the Gasification Technologies Conference, San Francisco, CA.

[45] Shirgaonkar A, Yong SZ, DNS Results for Sinking Effective Diffusivity. 2009.